Spectroscopic studies on ^{39}Ca for Classical Nova Endpoint Nucleosynthesis

Spectroscopic Studies on ^{39}Ca for Classical Nova Endpoint Nucleosynthesis

By Johnson Liang,

A Thesis Submitted to the School of Graduate Studies in the Partial Fulfillment of the Requirements for the Degree Doctor of Philosophy

McMaster University
Doctor of Philosophy (2020)
Hamilton, Ontario (Department of Physics and Astronomy)

TITLE: Spectroscopic Studies on ^{39}Ca for Classical Nova Endpoint Nucleosynthesis
AUTHOR: Johnson Liang (McMaster University)
SUPERVISOR: Dr. Alan Chen
NUMBER OF PAGES: xvi, 114

Lay Abstract

The goal of this work is to investigate processes that create the chemical elements of the universe. This occurs through nuclear reactions of elements produced after Big Bang nucleosynthesis. These nuclear reactions are only possible in the hot, dense environments found in stars and explosive stellar events. One such stellar event is the classical nova, which can produce elements as heavy as Calcium. Although a multitude of nuclear reactions occur during a classical nova, only a handful have a large effect on the abundance of elements produced. This work studies the properties of a specific nuclear reaction that can strongly affect the abundances of elements synthesized in classical novae.

Abstract

In classical novae, the endpoint of nucleosynthesis occurs near A $\sim$ 40. Currently, observations of classical novae predict an order of magnitude enhancement of endpoint elements, such as Ar, K, and Ca, relative to solar abundances; however, simulations predict abundances closer to that of solar abundances.

A sensitivity study examining the effect of reaction rates on the abundances of these elements has shown that the reaction ^{38}K(p,γ)^{39}Ca can change the abundances of endpoint nuclides by an order of magnitude or more. In temperatures characteristic of this environment, this reaction rate is dominated by ℓ=0 resonance reactions within the Gamow window. These correspond to states in ^{39}Ca of $J^{\pi}5/2^{+}$ and $7/2^{+}$ between $E_x = 6.0 - 6.5$ MeV . While a direct measurement was carried out for these states, more precise values for the excitation energies were recommended.

In this work high resolution spectroscopic studies of ^{39}Ca were carried out to provide more information on the various resonances that lie in the Gamow window, and illuminate additional undiscovered states. The first study was conducted at the Maier-Leibnitz-Laboratory (MLL), employing the ^{40}Ca(d,t)^{39}Ca reaction, and the follow up study was conducted at the Triangle Universities Nuclear Laboratory (TUNL) using the ^{39}K(^{3}He,t)^{39}Ca reaction. The method and apparatus are discussed in this work. Energy levels in ^{39}Ca with 10 keV uncertainties had uncertainties reduced to 3-4 keV. In addition, several new states were found in ^{39}Ca from the TUNL experiment. Finally, there is an $\sim$ 10 keV systematic difference between previously evaluated states and the states measured in this work - a factor that affects the direct measurement carried out previously. This factor in combination with the results of this work show that the reaction rate of this may be higher than previously thought, and have a higher impact on the final abundances of elements synthesized in classical novae.

Acknowledgements

First, I would like to thank my supervisor Prof. Alan Chen for his role throughout this journey. You have been an exemplar in mentorship, and have taught me such a great deal not only in science, but in being a scientist. I have always felt supremely lucky to be a student of yours. You've generously given me innumerable opportunities to learn; whether in a laboratory or over a beer (and sometimes both at the same time). I will always be thankful for your patience, wisdom, and bonhomie, but I am most thankful for your encouragement. Six years ago I had no idea of what I wanted to do and looking back, I was a bit of a mess. You've helped me grow as a person, and instilled a confidence in my own ability. It is difficult to put into words how significant that is to me, so I hope that my utmost gratitude can give you a sense of it.

I would also like to thank Dr. Balraj Singh. You are the embodiment of perseverance, and I can only dream that I will one day match your level of dedication. Funnily enough, I found an e-mail in the summer of 2015 saying we might finish our project in six months; little did we know it would take closer to six years! I will remember the work we did in your office at the back of the lab fondly. Thank you for your personal interest in my academic career, your help in shaping my knowledge, and for bringing us to Tandoori Flame. I hope that we can share a meal soon.

I would be remiss if I did not give great thanks to my committee members: Prof. Soo Hyun Byun and Prof. Iris Dillmann. Your guidance in our annual meetings was indispensable. The dilligence in improving the thesis made by you two and Prof. Anu Kankainen cannot be overstated. Your suggestions to the present work have substantially improved its quality, and I can't thank you all enough for the time and effort that you have spent on this thesis.

Thank you to Dr. Daid Kahl, Dr. Kiana Setoohdenia, and the newly minted Dr. Athanasios Psaltis - my academic siblings - for helping me with any questions I had, and for the great times that we shared. I look forward to working together in the future!

To Mom, Dad, Carson, and all the rest of the family, thank you for your constant support. It gave me great comfort to know that no matter where life led me, I always had a home to come back to (with a tasty meal to boot).

I'd like to thank Melanie Demers for being the best partner I could have hoped for. You were always there to give me a hug or a kick in the ass when I needed it most. You are compassionate and lovely, and always know how to put a smile on my face. Thank you for sharing your brilliance with me, for strengthening my character, and thank you for believing in me in the times where I didn't believe in myself.

Lastly, I'd like to thank all the friends that have I've met along the way. Thanks to the friends who shared the late nights in ABB, desperately studying for the exam the next morning. Thanks to the friends who went on road trips to play card games competitively, or romped down the streets of an unexplored city. Thanks to the friends who looked up at the night sky with me from the shore of a lake or the top of a mountain. I'm glad to have met all of you; you've made this time in my life so much richer, and your company means more to me than you'll ever know.

Contents

List of Figures

List of Tables

Chapter 1

Introduction

1.1 Nuclear Physics Considerations

This section will cover the nuclear interactions that are relevant for this PhD thesis. In general, we have a particle incident on a target nucleus. The particle first encounters the repulsive Coulombic force which acts as a barrier to the attractive potential at the core of the system. The first part of this section will deal with the quantum mechanical aspects of scattering with an incident particle on this type of system. The phenomenon known as resonances will then be discussed, since it plays a crucial role in the nuclear reactions in astrophysical environments. Finally the general nuclear reaction rate will be discussed, and delving deeper, the nuclear reaction rate for resonance reactions will be discussed.

1.1.1 Resonances with the Square Potential Barrier

To explain the quantum mechanical considerations when dealing with resonances, it is instructive to first revisit particle scattering on the square barrier potential to define which variables are important to the concept of resonances [1]. This is pictured in Figure 1.1, as three regions in the system. Region I defines the attractive potential of depth V_0. Region II is the square-barrier potential, which acts to repel the incoming particle. Finally, in Region III no potential is present.

Here we assume that the potential is radially symmetric, ($\ell = 0$, or s-wave transmission), so Schrödinger's time independent equation for a particle is given by:

$$\frac{d^2u}{dr^2} + \frac{2m}{\hbar^2}[E - V(r)]u = 0 \tag{1.1}$$

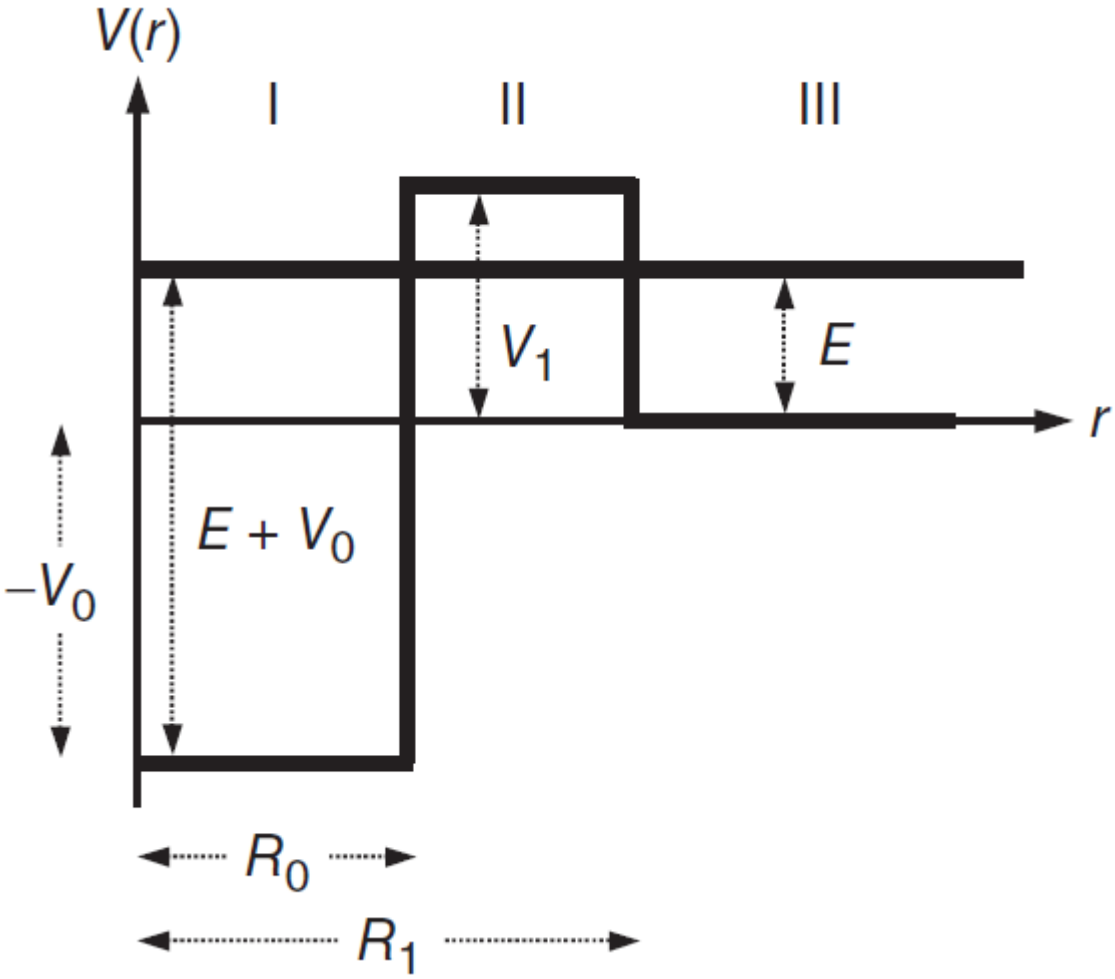

FIGURE 1.1: Square barrier potential, with potential of radius R_0, and a repulsive square barrier with thickness $\Delta R = R_1 - R_0$, and height V_1. The energy of the particle is less than the barrier potential [1].

where u is the radial wave function of the particle, m is the mass of the particle, r is the radius coordinate, E is the energy of the particle, and $V(r)$ is the potential experienced by the particle. If one solves the Schrödinger's equation explicitly, one obtains the following solutions for u in each region:

For Region I, $E - V > 0$, we obtain:

$$u_I = Ae^{iKr} - Be^{-iKr}, \quad K^2 = \frac{2m}{\hbar^2}(E + V_0) \tag{1.2}$$

The solution in Region II can be written in terms of real exponentials, after some algebra:

$$\begin{aligned} u_{II} &= Ce^{ik_{II}r} + De^{-ik_{II}r}, \qquad & k_{II}^2 &= \frac{2m}{\hbar^2}(E - V_1) = i^2\kappa^2 \\ &= Ce^{-\kappa r} + De^{\kappa r} \end{aligned} \tag{1.3}$$

Lastly in Region III, we again have a solution given by $E - V > 0$, with the solution:

$$u_{III} = Fe^{ikr} + Ge^{-ikr}, k^2 = \frac{2m}{\hbar^2}E \tag{1.4}$$

The second term in u_I describes a plane wave traveling in the negative r direction, which is analogous to the successful transmission into the positive attractive potential. The first and second terms of u_{III} correspond to the plane wave reflected from the barrier and incident wave moving towards the barrier, respectively.

We can define a quantity called the transmission coefficient given by the ratio of the flux of transmitted particles, and incident particles. These fluxes are given by the product of their intensities and velocity:

$$\hat{T} = \frac{j_{trans}}{j_{inc}} = \frac{v_{in}|B|^2}{v_{out}|G|^2} = \frac{K|B|^2}{k|G|^2} \tag{1.5}$$

where B^2 is the intensity of the -r moving wave in region I (Equation 1.2) and G^2 is the intensity of the -r moving wave in region III (Equation 1.4), In order to obtain the coefficients B and G , we can use the continuity condition on the barrier and isolate these variables. We require that the wave function and their derivatives be continuous at the boundaries set by R_0 and R_1.

The set of equations that we obtain at the boundaries are given by:

$$Ae^{iKR_0} + Be^{-iKR_0} = Ce^{-\kappa R_0} + De^{\kappa R_0} \tag{1.6}$$

$$i\frac{K}{\kappa}(Ae^{iKR_0} - Be^{-iKR_0}) = -Ce^{-\kappa R_0} + De^{\kappa R_0} \tag{1.7}$$

$$Ce^{-\kappa R_1} + De^{\kappa R_1} = Fe^{ikR_1} + Ge^{-ikR_1} \tag{1.8}$$

$$-Ce^{-\kappa R_1} + De^{\kappa R_1} = i\frac{k}{\kappa}(Fe^{ikR_1} + Ge^{-ikR_1}) \tag{1.9}$$

By adding and subtracting pairs of equations, one can isolate for the quantities of interest, B and G, and obtain a function for the transmission probability.

$$\hat{T} = \frac{Kk}{[K+k]^2 + [\kappa^2 + K^2 + k^2 + K^2k^2/\kappa^2]\sinh^2(\kappa\Delta R)} \tag{1.10}$$

where $\Delta R = R_1 - R_0$. This can be rewritten in terms of energy by expanding further:

$$\begin{aligned}\frac{1}{\hat{T}} =& \frac{1}{\sqrt{E(E+V_0)}}\Big(\left[2E + V_0 + 2\sqrt{E(E+V_0}\right] \\ &+ \left[E + V_0 + V_1 + \frac{E(E+V)_0)}{V_1 - E}\right]\sinh^2\left[\sqrt{(2m/\hbar^2)(V_1 - E)}\Delta R\right]\Big)\end{aligned} \tag{1.11}$$

The result is important as it shows that even if the energy of the particle coming from the right side is less than the barrier it encounters, there is a nonzero probability that it will reach the left side of the barrier. This is known as the tunnel effect, and is important for how we understand charged-particle reactions in stars.

We can now instead consider the solutions, given the continuity conditions at the boundary. The wave functions for the aforementioned regions are as follows:

$$u_I = A' sin(Kr) \tag{1.12}$$
$$u_{II} = Ce^{-\kappa r} + De^{\kappa r} \tag{1.13}$$
$$u_{III} = F' sin(kr + \delta) \tag{1.14}$$

where δ describes the phase shift that the particle experiences after entering into the attractive potential. From here, we can find the ratio of $|A'|^2/|F'|^2$, the relative intensity in the interior region compared to the region exterior to the potential.

$$\begin{aligned}\frac{|F'|^2}{|A'|^2} &= \sin^2(KR_0) + \left(\frac{K}{k}\right)^2 \cos^2(KR_0) \\ &+ \sin^2(KR_0)\sinh^2(\kappa\Delta R)\left[1 + \left(\frac{\kappa}{k}\right)^2\right] \\ &+ \cos^2(KR_0)\sinh^2(\kappa\Delta R)\left[\left(\frac{K}{\kappa}\right)^2 + \left(\frac{K}{k}\right)^2\right] \\ &+ \sin(KR_0)\cos(KR_0)\sinh(2\kappa\Delta R)\left[\left(\frac{K}{\kappa}\right) + \left(\frac{K}{\kappa}\right)\left(\frac{\kappa}{k}\right)^2\right]\end{aligned} \tag{1.15}$$

This ratio as a function of energy is shown in Figure 1.2. In this example, a neutron scatters from a square barrier potential with the following properties: $V_1 = 10$ MeV, $R_0 = 3$ fm, and $R_1 = 8$ fm, and reaches an attractive potential of $V_0 = 50$ MeV, and $V_0 = 100$ MeV in the solid and dashed line respectively [1]. From here, we can see that there is an enhancement of the interior intensity at specific values of energy - that is, an increased chance that the particle penetrates the barrier and makes it into the attractive potential. This is the phenomenon known as resonance scattering and results from favourable wave matching conditions at the boundaries. We see that for the $V_0 = 100$ MeV case, there is no wave matching in the energy range shown, so a resonance does not form, and additionally when normalized with the transmission coefficient $\hat{T}$, it is nearly constant with energy. In the $V_0 = 50$ MeV case, there is a clear resonance formed where we have good wave matching conditions.

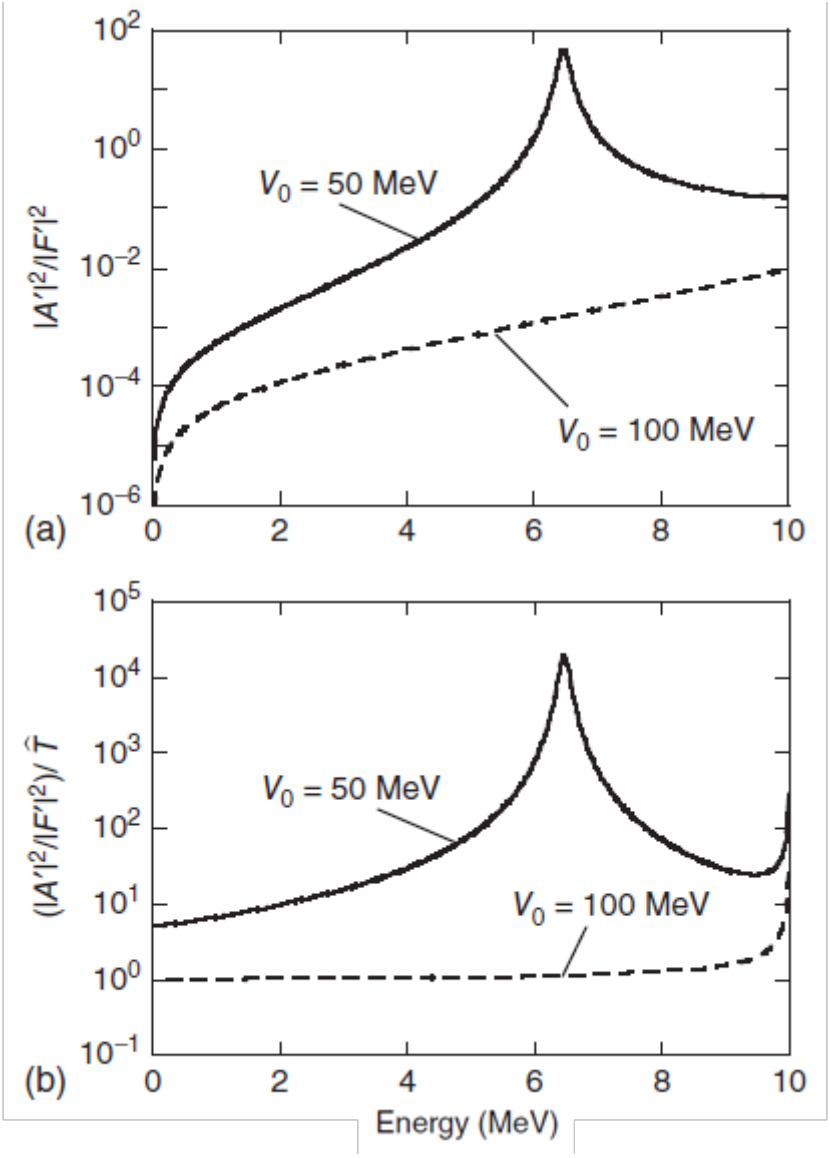

FIGURE 1.2: Resonance structures of neutron scattering: a) $|A'|^2/|F'|^2$ b) $(|A'|^2/|F'|^2)/\hat{T}$. Properties for the potentials are described in text of [1]. Figure adopted from [1]

Alternatively, we can plot $|A'|^2/|F'|^2$ for a neutron with E = 5 MeV, scattering from a barrier of the same properties as previously, but vary the depth of the attractive potential. This would allow us to probe various resonances that emerge from the good wave matching conditions for a given neutron energy. This is shown in Figure 1.3. The first resonance comes from good wave matching conditions with no nodes within the region $r < R_0$. The second resonance corresponds to a single node, the third resonance to two nodes and so on. In general, a resonance is formed when a the wave function passing into the potential forms a discrete quasi-stationary state within the boundaries of the potential well, and is governed by the properties of the incoming wave, potential and barrier. When this happens, a marked increase in the transmission (and thus cross section of the reaction) occurs.

1.1.2 Quantum Tunneling and the Gamow window

We now apply the phenomenon of tunneling to the context of the stellar environment; namely the tunneling effect through the Coulomb barrier into the potential well provided by the attractive strong force for charged particle reactions. These are especially relevant in proton capture reactions such as those described in section 1.2.

A schematic of the Coulomb barrier is shown in Figure 1.4 [1]. In the diagram a particle with energy, E, encounters a repulsive Coulomb barrier followed by the potential well provided by the attractive strong force at a distance, R_0. The radius R_c describes the classical turning point - where the incoming kinetic energy of the particle equals that of the Coulomb potential energy, The transmission probability for tunneling through the square barrier can now be applied here by splitting the barrier potential into slices of radius dr, and integrating over the length of the barrier. This is given by:

$$\hat{T} = \hat{T}_1 \cdot \hat{T}_2 \cdot ... \hat{T}_n \approx \exp\left[-\frac{2}{\hbar}\int_{R_0}^{R_C} \sqrt{2m|V(r) - E|}\, dr\right] \tag{1.16}$$

For a Coulomb potential, $V_c = Z_1 Z_0 e^2/r$:

$$\hat{T} \approx \exp\left[-\frac{2}{\hbar}\sqrt{2m}\int_{R_0}^{R_C} \sqrt{\frac{Z_0 Z_1 e^2}{r} - E}\, dr\right] \tag{1.17}$$

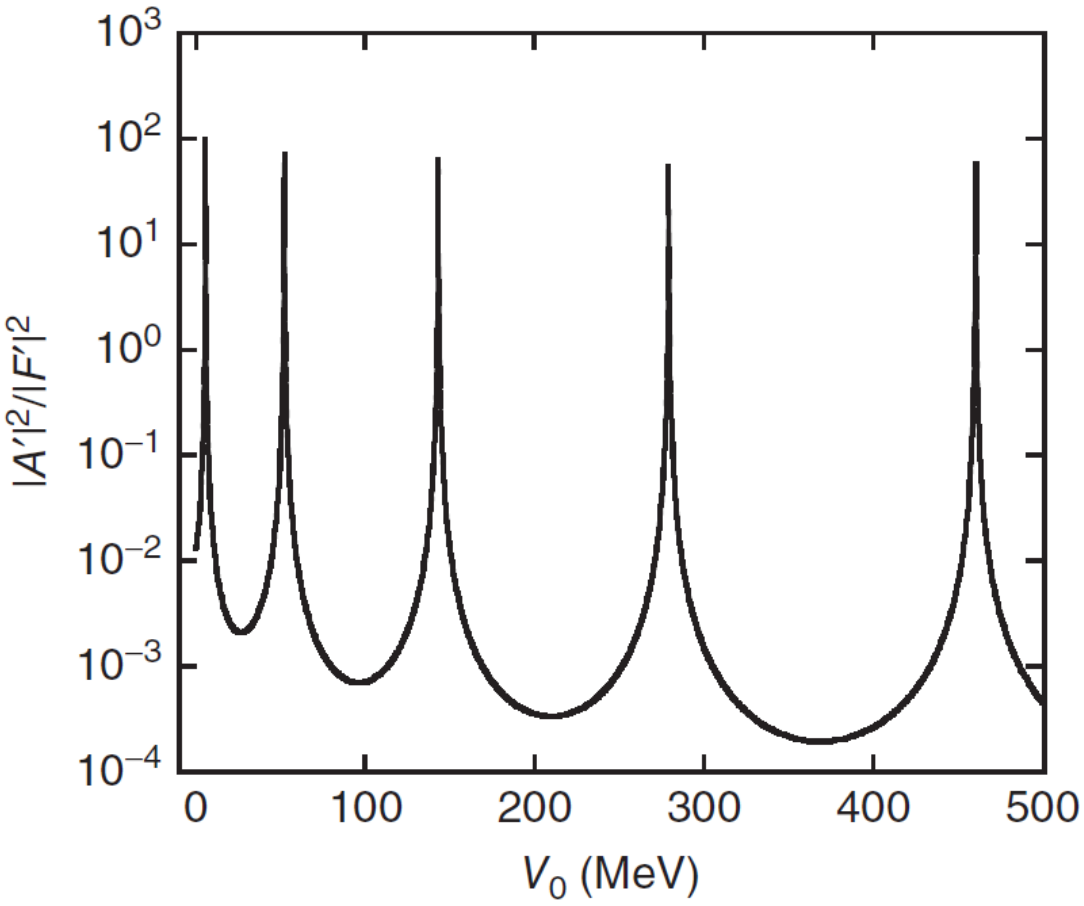

FIGURE 1.3: Resonances of a 5 MeV neutron scattering on a potential barrier with varying attractive potential depth. Figure adopted from [1].

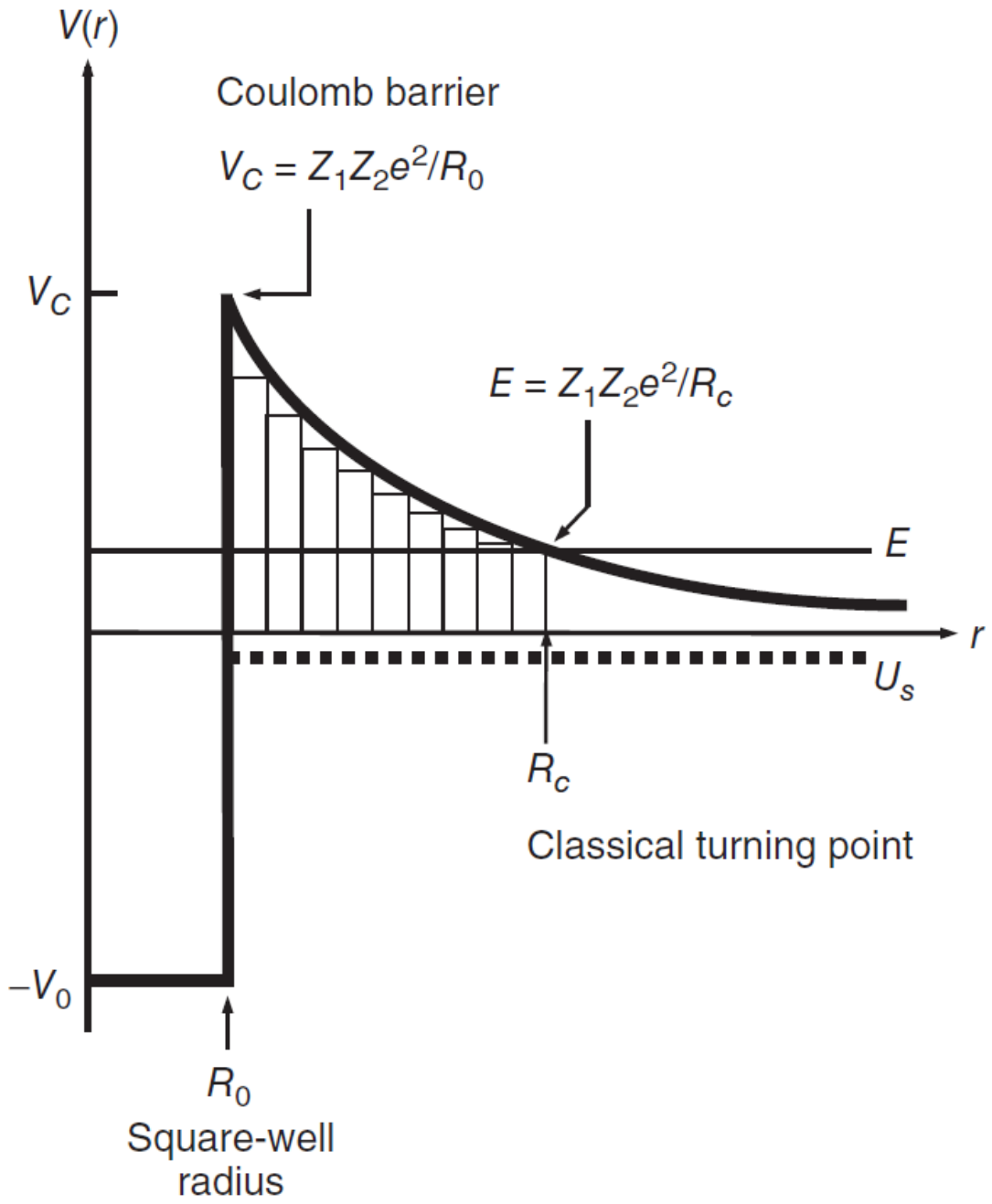

FIGURE 1.4: Schematic of Coulomb barrier, and the tunnelling effect, as well as a simplified potential well provided by the attractive strong force. Figure adopted from [1]

where Z_0 and Z_1 are the charges of the projectile and target respectively, and e is the elementary charge. Reiterating that the energy of the incident particle is equal to the Coulomb potential at the radius R_c, we can express the energy of the particle as $E = Z_0 Z_1 e^2 / R_c$. Substituting this into the integral above:

$$\hat{T} \approx \exp\left(-\frac{2}{\hbar}\sqrt{2mZ_0Z_1e^2}\int_{R_0}^{R_C}\sqrt{\frac{1}{r}-\frac{1}{R_c}}dr\right) \tag{1.18}$$

This integral can be solved analytically, and yields the expression:

$$\hat{T} \approx \exp\left(-\frac{2}{\hbar}\sqrt{\frac{2m}{E}}Z_0Z_1e^2\left[\arccos\sqrt{\frac{E}{V_c}}-\sqrt{\frac{E}{V_c}\left(1-\frac{E}{V_c}\right)}\right]\right) \tag{1.19}$$

At low energies compared to the Coulomb barrier, we can expand $\arccos\sqrt{x} - \sqrt{x(1-x)} \approx \pi/2 - 2\sqrt{x} - 2\sqrt{x} + x^{3/2}/3$, and simplify to:

$$\hat{T} \approx exp\left(-\frac{2\pi}{\hbar}\sqrt{\frac{m}{2E}}Z_0Z_1e^2\right) = e^{-2\pi\eta} \tag{1.20}$$

This equation describes the transmission of the particle through the Coulomb barrier, where the term on the right is the Gamow factor and the coefficient η is called the Sommerfeld parameter.

1.2 Reaction rate formalism

This section will describe the reaction rate formalism used to determine the rate of nuclear interactions in stars. Since the hydrostatic equilibrium of the star depends highly on thermal pressure the rate of heat generation via nuclear reactions is of great importance. In addition to that, the chemical abundances in a star depend directly on the rates of the multitude of reactions that take place during the various epochs of the star's life. The reaction rate will be broken down into three sections: general considerations, non-resonant reaction rates, and resonant reaction rates.

1.2.1 Stellar Reaction Rate

We can denote a nuclear reaction with the notation: $0 + 1 \rightarrow 2 + 3$, where 0 and 1 are the incoming projectile and target respectively, and 2+3 are the residual nucleus and ejectile respectively. In a stellar plasma, the rate of this reaction is the product of the cross section and the current density of each particle species.

The nuclear reaction cross section is the quantitative probability that the nuclei 0 and 1 will interact [1]. Qualitatively, the simplest case is the overlap between two spherical objects. The physical cross section of that system would be $\sigma = \pi(R_0 + R_1)^2$ where R_i is the radius of each spherical object respectively. However since nuclei typically have a wave nature associated with them, this convenient picture is not accurate. In general, the cross section depends on the relative velocity of the target-plus-projectile system such that $\sigma = \sigma(v)$.

The current density of particles is defined as the number of particles per unit time and unit area. For the interaction of particles 0+1, and assuming the interacting particles with a non-zero rest mass (i.e not a photon), the reaction rate is given by

$$r_{01} = N_0 N_1 v \sigma(v) \tag{1.21}$$

where N_0 and N_1 are the number densities of particles of species 0 and 1 respectively, v is the relative velocity between the two interacting particles, and $\sigma(v)$ is the cross section of the interaction with respect to velocity. At this point, we need to consider the velocity of particles in the stellar plasma. Particles will not move with a constant velocity relative to each other, and instead there is a distribution of velocities among the particles. This distribution can be described with a probability function, $P(v)$, which is the probability that a particle will be found with a specific velocity. It follows that $P(v)dv$ is the probability that a particle will be found between v and $v + dv$. This probability function is normalized such that

$$\int_0^\infty P(v)dv = 1 \tag{1.22}$$

and so the total reaction rate over all velocities can then be described by:

$$r_{01} = N_0 N_1 \int_0^\infty v P(v) \sigma(v) dv = N_0 N_1 < \sigma v >_{01} \tag{1.23}$$

where $< \sigma v >_{01}$ describes the reaction rate per particle pair. Should the particle species 0 and 1 be identical, the particle pairs that are reacting given a number density N_0 is:

$$\frac{N_0(N_0 - 1)}{2} \approx \frac{N_0^2}{2} \tag{1.24}$$

the reaction rate can be expressed conveniently as:

$$r_{01} = \frac{N_0 N_1 v \sigma(v)}{1 + \delta_{01}} \tag{1.25}$$

where the Kronecker delta δ_{01} is unity when the particle species 0 and 1 are the same.

For most stellar environments, the kinetic energies is from their thermal motion and thus the reactions are named thermonuclear reactions. The probability distribution of this motion is well described by the Maxwell-Boltzmann distribution if we assume that the temperature is high enough such that particles are ionized [2], but have not reached relativistic velocities, and that the densities are sufficiently low such that we do not have degenerate matter (see subsection 1.3.1. This is given by:

$$P(v)dv = \left(\frac{m_{01}}{2\pi k T}\right)^{3/2} e^{-m_{01} v^2/(2kT)} 4\pi v^2 dv \tag{1.26}$$

where the Boltzmann constant is $k = 8.6173 \times 10^{-5}$ eV/K, T is the temperature of the plasma, and m_{01} is a quantity described as the reduced mass, given by $m_{01} = m_0 m_1/(m_0 + m_1)$. This is a convenient variable for considering the system in a centre-of-mass frame.

We can then transform this to be in terms of energy, since $E = \frac{1}{2} m_{01} v^2$ and $dE/dv = m_{01} v$:

$$P(v)dv = \frac{2}{\sqrt{\pi}} \frac{1}{(kT)^{3/2}} \sqrt{E}\, e^{-E/kT} dE \tag{1.27}$$

and a final expression for the nuclear reaction rate can be written as:

$$N_A < \sigma v >= \left(\frac{8}{\pi m_{01}}\right)^{1/2} \frac{N_A}{(kT)^{3/2}} \int_0^\infty E\ \sigma(E)\ e^{-E/kT} dE \tag{1.28}$$

where we have defined N_A as Avogadro's Number $= 6.022 \times 10^{23}$. In this expression, the most complicated variable is undoubtedly the cross section. If the cross section is found, a numerical integration can be used to solve the reaction rate equation for a given environment and reaction. However a further complication occurs when considering the resonance phenomenon. At lower energies, the transmission through the Coulomb barrier, and thus the cross section, can vary significantly if there is good wave matching at particular energies (as discussed in the resonance phenomenon section). These resonant cross sections behave much differently than the comparatively simpler non-resonant cross sections, and require special treatment since resonance phenomena strongly affect the total reaction rate.

1.2.2 Non-resonant reaction rate

We now dive deeper into the calculations of the non-resonant reaction rates. These reaction rates deal with two-nuclei interactions called direct reactions, and typically occur between projectiles with higher incident energies in comparison to resonant reactions. When considering the de Broglie wavelength of the incident particle, one finds that the wavelength of the projectile is closer to that of a nucleon than a nucleus. Thus, the nuclei interact peripherally, with only one or two nucleons at the surface of the target nucleus. Examples include transfer reactions, knock-out reactions, etc. Features of direct reactions are single-step transitions from initial to final state which quickly proceed on the scale of 10^{-22} s [3].

Here it is useful to describe the quantity known as the astrophysical S-factor, $S(E)$. The S-factor is formulated to include all strictly nuclear effects. It is defined such that:

$$\sigma(E) = \frac{1}{E} e^{-2\pi\eta} S(E) \tag{1.29}$$

where the term $e^{-2\pi\eta}$ is the Gamow factor discussed earlier and describes the s-wave transmission probability when the energy of the particle is much lower than the Coulomb barrier. By defining the astrophysical S-factor such that it does not contain the $1/E$

term, it does not depend strongly on energy, and varies smoothly and slowly. This is compared to the reaction cross section, σ, which can vary strongly due to the exponential behaviour of the Coulomb penetration, especially at lower interaction energies. This makes the astrophysical S-factor a better tool for extrapolating to those lower energies. Expressing the reaction rate with this factorization of the cross section yields:

$$N_A < \sigma v >= \left(\frac{8}{\pi m_{01}}\right)^{1/2} \frac{N_A}{(kT)^{3/2}} \int_0^\infty e^{-2\pi\eta} S(E) e^{-E/kT} dE \tag{1.30}$$

Here I will reiterate the exponent of the Gamow factor:

$$-2\pi\eta = -\frac{2\pi}{\hbar}\sqrt{\frac{m_{01}}{2E}} Z_0 Z_1 e^2 \tag{1.31}$$

An important result that arises from the integrand of this expression is the appearance of the phenomenon known as the Gamow peak. The Gamow factor goes to zero at lower energies with a $e^{-\sqrt{\frac{1}{E}}}$ dependence, and increases at higher energies; denoting that as the energy increases, the tunneling probability also increases and vice versa, approaching zero at small energies. Meanwhile, the factor arising from the Maxwell-Boltzmann probability distribution goes as $\mathrm{e}^{-E/kT}$; denoting that the probability of finding a particle at a certain energy is lower as that particular energy increases, approaching zero at higher energies. If we assume the astrophysical S-factor is constant or sufficiently slowly varying for the time being, then the integrand is maximized at the maximum of the product of these two terms. This is the definition of the Gamow peak: a narrow range of energy where the reaction rate is maximized, and most of the nuclear reactions happen. This concept is pictured schematically in Figure 1.5.

The centroid of this peak can be determined by taking the derivative of this product with respect to energy and setting it equal to zero. This yields:

$$\frac{\pi}{\hbar} Z_0 Z_1 e^2 \sqrt{\frac{m_{01}}{2}} \frac{1}{E_0^{3/2}} - \frac{1}{kT} = 0 \tag{1.32}$$

Finding the maximum of this peak yields:

$$E_0 = \left(\left(\frac{\pi}{\hbar}\right)^2 (Z_0 Z_1 e^2)^2 \left(\frac{m_{01}}{2}\right) (kT)^2\right)^{1/3} \tag{1.33}$$

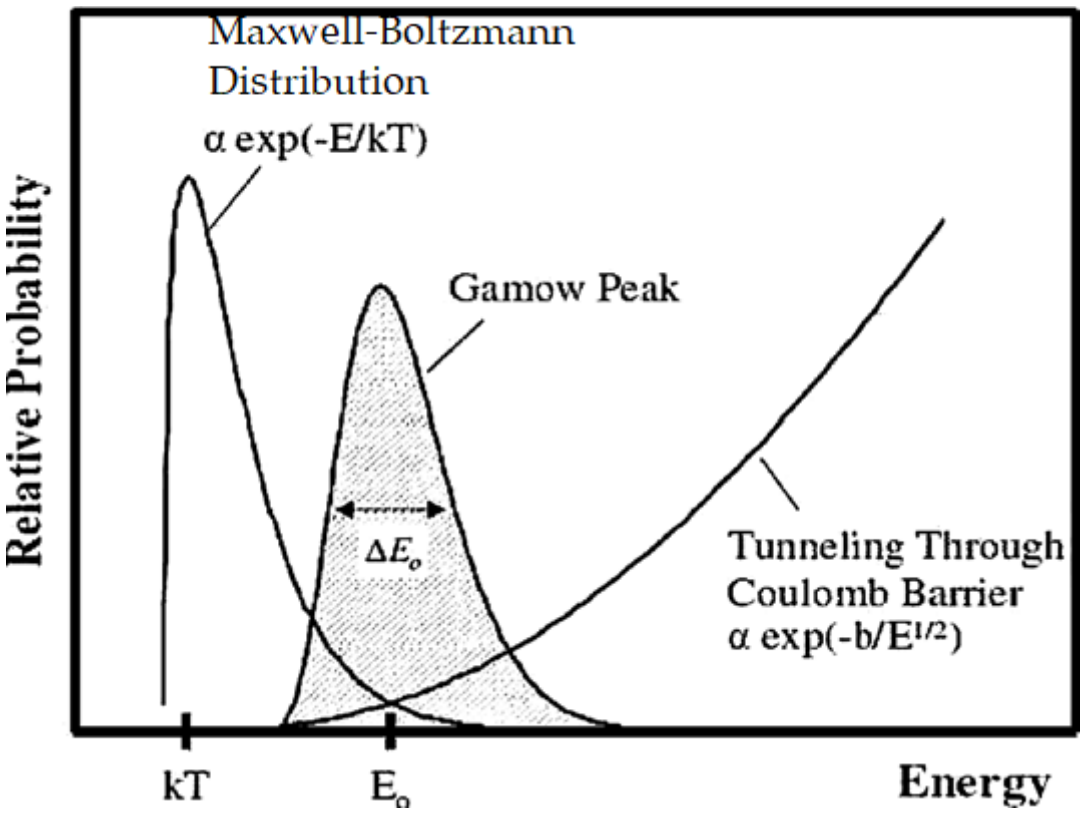

FIGURE 1.5: The Gamow peak represents the kinetic energy range in which the majority of nuclear reactions happen in a stellar environment. It is the overlap between the high energy tail of the Maxwell-Boltzmann distribution and the tunneling probability through the Coulomb barrier. Figure adopted from [4].

Thus, E_0 is the most effective temperature that induces nuclear reactions in a stellar plasma. We can also approximate the Gamow peak as a Gaussian function with centroid at E_0, and 1/e width Δ defined as:

$$\Delta = \frac{4}{\sqrt{3}}\sqrt{E_0 kT} \tag{1.34}$$

Within the boundary of this width - that is an energy window $E_0 - \Delta/2$ to $E_0 + \Delta/2$ - is the energy range in which the majority of the nuclear reactions happen.

1.2.3 Resonant reactions

For non-resonant reactions, a smoothly varying astrophysical S-factor worked well for describing the cross section. In resonant reactions, the S-factor would vary strongly at resonance energies due to reasons outlined in previous sections. Here we will consider isolated and narrow resonances. The first condition requires that the resonance be well separated from other resonances such that they do not overlap. The second is that it must be narrow such that the partial widths are approximately constant over the total resonance width.

The cross section of an isolated resonance is well described by the one-level Breit-Wigner formula[1]:

$$\sigma_{BW}(E) = \frac{\lambda^2}{4\pi}\frac{(2J+1)(1+\delta_{01})}{(2j_0+1)(2j_1+1)}\frac{\Gamma_0\Gamma_1}{((E_r-E)^2+\Gamma^2/4)} \tag{1.35}$$

where j_i are the spins of the target and projectile, J and E_r are the spin and energy of the resonance. δ_{01} is a Kronecker delta; when the particles are of the same species $\delta_{01} = 1$, else $\delta_{01} = 0$. Γ_i are the partial widths of the entrance and exit channel (0 and 1 respectively) of the resonance. Γ is the total width.

To explain the variables listed in the Breit-Wigner equation, first we must examine what qualitatively happens in the nucleus during resonant reactions. The incident particle enters the vicinity of the larger target nucleus with a de Broglie wavelength that is similar to that of the target nucleus. Because of this, the incident particle interacts with the entire nucleus, in contrast to the higher energy particle in the non-resonant

reaction section [3]. In a successful reaction, the incident particle fuses with the target nucleus and forms a compound nucleus. While in this state, the excess energy is distributed among all the nucleons. Although there may be enough energy to eject a particle from the nucleus, since it is distributed among the entire nucleus, it remains stable for long time compared to the direct reaction, but will eventually decay. The result is that the decaying state has an imprecise energy by the uncertainty principle. The energy is distributed in probability by:

$$\Gamma \approx \hbar/\tau \tag{1.36}$$

where τ is the lifetime of the state. These typically range from $10^{-14} - 10^{-20}$s and less [3], leading to widths that are of scale $\Gamma << 1$ MeV. The total width tells us the width of the probability distribution of all outcomes or channels in the reaction. Partial widths describe the widths of each individual reaction and decay channel, and the sum of the partial widths yields the total width. The cross section of any given reaction is proportional to the partial widths involved in that reaction,

The compound nucleus can exhibit quasi-stationary quantum states (as outlined in the subsection 1.1.1) with discrete energies, spins and parities. The cross section of a reaction shows a marked increase when the excitation energy of the compound nucleus matches that of a quasi-stationary quantum state's resonance energy. We can now see that in the Breit-Wigner formula for resonances, the last term depends on the resonance energy of the state, the partial widths for the reaction channels, as well as the total width.

Additionally, the ability to form a resonant state is subject to selection rules. These are given by the angular momentum and parity conservation laws:

$$J_0 \oplus J_1 \oplus \ell = J \tag{1.37}$$

where J is the spin of the resonant state, J_x are the spins of the incident particle and target, and ℓ is the orbital angular momentum. The parity of the system must also be

conserved such that:

$$\pi(J_0)\pi(J_1)(-1)^{\ell} = \pi(J) \tag{1.38}$$

where $\pi(J)$ is the parity of the final resonant state, $\pi(J_x)$ are the parities of the incident particle and target.

This time, we would like to substitute the Breit-Wigner formula for resonance cross sections into the cross section variable of Equation 1.28.

$$N_A < \sigma v > = \left(\frac{8}{\pi m_{01}}\right)^{1/2} \frac{N_A}{(kT)^{3/2}} \int_0^\infty E \left(\frac{\lambda^2}{4\pi}\omega \frac{\Gamma_0\Gamma_1}{((E_r - E)^2 + \Gamma^2/4)}\right) e^{-E/kT} dE \tag{1.39}$$

$$= N_A \frac{\sqrt{2\pi}\hbar^2}{(m_{01}kT)^{3/2}}\omega \int_0^\infty \frac{\Gamma_0\Gamma_1}{(E_r - E)^2 + \Gamma^2/4} e^{-E/kT} dE \tag{1.40}$$

where we have used the definitions:

$$\omega = \frac{(2J+1)(1+\delta_{01})}{(2j_0+1)(2j_1+1)} \qquad \lambda^2 = \frac{h^2}{p^2} = \frac{h^2}{2mE} \tag{1.41}$$

We can now make some assumptions for certain variables in the equation. For narrow widths, the Maxwell-Boltzmann portion is relatively constant at $E = E_r$. The partial widths are also approximately constant over the energy width of the resonance. The integral can then be calculated analytically.

$$\begin{aligned} N_A < \sigma v > &= N_A \frac{\sqrt{2\pi}\hbar^2}{(m_{01}kT)^{3/2}} e^{-E_r/kT}\omega \cdot 2\frac{\Gamma_0\Gamma_1}{\Gamma} \int_0^\infty \frac{\Gamma/2}{(E_r - E)^2 + \Gamma^2/4} e^{-E/kT} dE \\ &= N_A \frac{\sqrt{2\pi}\hbar^2}{(m_{01}kT)^{3/2}} e^{-E_r/kT}\omega \cdot 2\frac{\Gamma_0\Gamma_1}{\Gamma} \cdot \pi \\ &= N_A \left(\frac{2\pi}{m_{01}kT}\right)^{3/2} \hbar^2 e^{-E_r/kT}\omega\gamma \qquad \gamma = \frac{\Gamma_0\Gamma_1}{\Gamma} \end{aligned} \tag{1.42}$$

The term $\omega\gamma$ is an important quantity known as the resonance strength, and is proportional to the area under the resonance cross section. Quantitatively this is the

product of the resonance cross section evaluated at E_r and the total width Γ of the resonance:

$$\Gamma \cdot \sigma_B(E_r) = \Gamma \cdot \frac{\lambda_r^2}{\pi}\omega\frac{\Gamma_0\Gamma_1}{\Gamma^2} = \frac{\lambda_r^2}{\pi}\omega\gamma \tag{1.43}$$

The reaction rates for narrow resonances are specifically dependent on the resonance strength and the energy, experimentally measurable quantities.

1.3 Astrophysics Considerations

In this section we will explore the environments that produce the chemical elements that are present in the universe today. In this thesis, we will be mainly concerned with the nucleosynthesis that occurs in a classical nova, occuring on the surface of white dwarf stars. The properties of the white dwarf will be discussed, as well as how the classical nova unfolds.

1.3.1 Introduction to White Dwarfs

For main sequence stars with a mass between $0.4 - 11$ $M_\odot$, the star will eventually fuse hydrogen in its core to helium. For stars on the larger end of this range (larger than 2.2 $M_\odot$, the ashes of helium burning - carbon and oxygen - are present. During this part of the star's evolution its thin hydrogen-rich envelope will be shed, revealing the electron degenerate core. The expanding shell will go on to form the planetary nebula, a sublime pattern of gas which is suffused with colour from re emitting the light of the dying star,

The central degenerate core goes on to become the white dwarf, a compact stellar object of high density and supports itself through electron degeneracy pressure. The following section will describe properties of the white dwarf.

In general, the mass of a white dwarf will depend on the mass of the progenitor star, as well as if it was in a binary system or not. In general, we can separate them into three classes of white dwarfs based on their final composition prior to entering the white dwarf phase: Helium white dwarfs (He-WD), Carbon-Oxygen white dwarfs (CO-WD), and Oxygen-Neon white dwarfs (ONe-WD) [5].

The Helium white dwarf (He-WD) mainly consists of helium and has shed its hydrogen-rich envelope. These stars have a lower mass relative to the other two, and their progenitor star has an initial mass of $M < 2.2M_{\odot}$. These stars typically do not reach the helium core flash[1](He-flash) during their evolution, thus the composition is chiefly helium. One last consideration is that the wind mass loss is not strong enough to fully remove the hydrogen-rich envelope for isolated He-WDs. Thus, it is thought that they lose their envelope via mass transfer in a close binary. The masses of these WDs are between $0.15M_{\odot} - M_{He-Fl}$, the upper limit being the mass of the He core at onset of the He-flash, $M_{He-Fl} \approx 0.45 - 0.5M_{\odot}$.

CO-WDs mainly consist of carbon and oxygen, and have also shed their hydrogen-rich envelope. The initial mass of a single progenitor star for this is typically $M < 6 - 8M_{\odot}$, and in binaries, this can reach up to $10M_{\odot}$. The evolution of these progenitor stars leads to helium burning through the triple-α process, which is responsible for the carbon-oxygen composition; however, these stars are not massive enough for carbon burning. The CO-WD mass is between $M_{He-Fl} - M_{C-ign}$, the lower limit as the mass of the core prior to the He-flash, and the upper limit as the core mass at the onset of carbon ignition, $M_{C-ign} = 1.1M_{\odot}$.

ONe-WDs originate from the largest progenitor stars compared to the others. Single stars have an initial mass between $9 - 10M_{\odot}$, and in binaries can range from $9 - 12M_{\odot}$. These stars lose their envelopes in the Super-AGB phase, and can undergo carbon and oxygen ignition, creating oxygen and neon respectively, and with trace amounts of magnesium and sodium. The WDs that result from these stars are typically between $1.1M_{\odot} - 1.38M_{\odot}$.

Generally in interacting binary systems, each respective white dwarf can form from progenitor stars with a larger initial mass compared to the single star case. This can be explained as follows: As a star evolves, it grows considerably during some phases. If the companion star (also referred to as secondary star or donor star) expands in this way, its outer shell can be siphoned onto the primary star. This ultimately affects the evolution of both stars through mass and angular momentum changes.

[1]The helium core flash is a runaway thermonuclear event that occurs with the synthesized helium from hydrogen burning. The helium produced will sink to the core and form an electron degenerate core. Upon ignition through the triple-α process - the process in which three α particles are combined into Carbon - thermonuclear runaway will occur. This process occurs in a timescale of a few seconds but can produce luminosities comparable to an entire galaxy ($10^{11}L_{\odot}$) [6]

White dwarfs have run out of their respective nuclear fuel to generate thermal pressure against the collapsing force of gravity. The supporting pressure is generated through electron degeneracy pressure of the electrons that exist in the plasma of the white dwarf [6]. This arises as a consequence of the Pauli exclusion principle: no two identical fermions (electrons in this case) can occupy the same quantum state in the same quantum system. As thermal pressure is removed due to lack of nuclear reactions, the electrons in this system are increasingly pushed to lower energy states. Since no two fermions can occupy the lowest energy states, they are unable to lower their energies due to this exclusion principle. There are 2 major consequences to this interaction:

The first consequence is that there is an upper limit to the mass of a white dwarf, named the Chandrasekhar limit. This occurs when the electrons are required to reach velocities higher than the speed of light to upkeep the necessary electron degeneracy pressure. This mass is accepted to be approximately 1.44 solar masses [7], and indeed there have been no observations of white dwarfs exceeding this mass.

The second consequence is that the structure of the degenerate gas is largely uncoupled from the thermal energy of the system [8]. We can define the energy of the highest energy electron arising from electron degeneracy pressure as the Fermi energy. The energy of this particle is independent of thermal energy, and can be observed if the system was at $T = 0$ K. As a result, if the temperature increases, gas will not expand until the temperature is high enough to surpass the Fermi energy. This will be an important detail when considering the thermonuclear runaway in the classical nova.

1.3.2 Classical novae

To understand the occurence of the classical nova, first we must explore the physics of a binary system, and the gravitational interactions of the gas within it.

For the interest of classical novae, we begin with the discussion of binary star systems which consist of a primary white dwarf star, typically a CO or ONe white dwarf, and a secondary main sequence star. In these configurations, the mass of the secondary star can be influenced by the gravitational force of the white dwarf primary. The consequence is that mass from the secondary star overflows its Roche lobe, and is siphoned to the primary white dwarf. This mass transfer from secondary star to primary star can be stable if the ratio of masses between the secondary to primary star is less than 0.8. If

the ratio is greater than 0.8, the mass from the secondary star is quickly transferred to a common envelope between the two stars until the ratio of less than 0.8 is achieved [9].

For a nova to occur within the timescale of the age of the universe - approximately 14 billion years [10], mass transfer from the secondary star to the primary star must occur at a rate of at least $10^{-11}M_{\odot}$/yr, and typical accretion rates are between $10^{-10} - 10^{-9}M_{\odot}$/yr. The accretion of mass onto the white dwarf primary from the secondary star leads to energy production and eventually the classical nova outburst. We will now explore the evolution of the classical nova.

When matter from the outer shell of the secondary star exceeds the Roche lobe enclosing it, that matter accretes onto the white dwarf primary. For higher mass secondary stars that can overfill their Roche lobe during their evolution in the red giant phase, the envelope expansion drives the mass towards the white dwarf primary. For low mass secondary stars which do not evolve in this way, mechanisms such as magnetic stellar wind and/or gravitational wave radiation can dissipate orbital angular momentum between the primary and secondary star, decreasing the distance between the two objects and adjusting the position of the Roche lobe enclosing the secondary star. If the radius of the secondary star exceeds the limit of the Roche lobe, then mass transfer from the secondary towards the white dwarf primary occurs. With regards to the angular momentum of the accreted matter, if the white dwarf has a slow rotation, it can directly flow onto the surface; however if this is not the case, the material will instead form a disk around the white dwarf primary [9]. In order to have inflow onto the surface of the white dwarf, the material must dissipate its angular momentum via molecular collisions and shockwaves.

This accretion forms a hydrogen-rich layer of gas on the surface of the white dwarf primary. As compressional heating increases the energy on this layer nuclear processes begin and the base layers of the accreted material become hot and degenerate. Hydrogen burning proceeds first through the pp-chain, and as temperature increases the CNO cycle takes over [11] . In the final stages of thermonuclear runaway, the hot CNO cycle (subsection 1.3.3) is the dominant process of nuclear burning. Compressional heating as well as the energy released by nuclear reactions both work to heat the accreted material; however, due to the quasi-decoupling of pressure and thermal energy present in degenerate matter, the accreted material does not expand and thermonuclear runaway occurs.

During the runaway, the hot CNO cycle is the prevalent form of energy generation. A consequence of this is that the energy rate is limited by the time scales of the β^+-decay nuclei. When the temperature of this region exceeds 10^8 K, the majority of CNO nuclei have picked up a proton and become unstable to β^+ decay. Since the material cannot expand due to degeneracy, convection becomes the main source of heat transfer. This has the effect of circulating unburned C, N, O, Ne, and Mg nuclei to the hotter burning shells, which sustains the nuclear energy generation at temperatures higher than 10^8K. This process means that proton capture reactions can compete with beta decay, and proton rich nuclides away from stability can be synthesized.

The lifetimes of these nuclei are longer than the convection turnover time of ~ 100 s [11], so β^+-unstable nuclei are able to reach the cooler, outer areas of the envelope before decaying. This decay is a source of intense energy which serves to lift degeneracy and allows the material to expand with temperature. This expansion is what halts the thermonuclear runaway. As it expands, the β^+-unstable nuclei decay and release energy into the non-degenerate, expanded material, rapidly raising the temperature throughout the shell. This shuts off convection by flattening the temperature gradient.

1.3.3 Explosive Nucleosynthesis in Classical Novae

A classical nova typically ejects between $10^{-5} - 10^{-4} M_\odot$ [12] of accreted material with a mean velocity of $\sim 10^3$ km/s into the surrounding area. Since these operate far from equilibrium, their isotopic abundances will be distinct to material processed through normal stellar burning.

As material accretes onto the surface of the white dwarf, the compressional heating and proton induced nuclear reactions continually raise the temperature. On the base layer, the degenerate matter is unable to expand, eventually leading to the thermonuclear runaway process [1]. During the accretion pp-chain reactions are responsible for energy generation. If CNO cycle catalysts are present, then at higher temperatures the CNO cycle will take over. During the final stages of the thermonuclear runaway, at temperatures between $T = 0.1 - 0.4$ GK, the hot CNO cycle takes over. An important point to reiterate is that the nucleosynthesis in hydrostatic conditions does not apply in the thermonuclear runaway environment. The main differences are: 1) proton capture reactions compete with β^+ decays, and 2) the temperature and density of the system change drastically with time. Thus a different treatment is required [11].

As stated previously, the main burning process during the thermonuclear runaway is the hot CNO cycle. The sequence of reactions in this cycle are as follows [1]:

Hot CNO1	Hot CNO2	Hot CNO3
^{12}C(p,γ)^{13}N	^{15}O(β^+,ν)^{15}N	^{15}O(β^+,ν)^{15}N
^{13}N(p,γ)^{14}O	^{15}N(p,γ)^{16}O	^{15}N(p,γ)^{16}O
^{14}O(β^+,ν)^{14}N	^{16}O(p,γ)^{17}F	^{16}O(p,γ)^{17}F
^{14}N(p,γ)^{15}O	^{17}F(β^+,ν)^{17}O	^{17}F(p,γ)^{18}Ne
^{15}O(β^+,ν)^{15}N	^{17}O(p,γ)^{18}F	^{18}Ne(β^+,ν)^{18}F
^{15}N(p,α)^{12}C	^{18}F(p,α)^{15}O	^{18}F(p,α)^{15}O

In each cycle, a catalytic group of C, N, and O isotopes undergoes proton induced reactions and subsequent β^+ decays in order to ultimately release a helium nucleus. This avenue of energy generation will depend highly on the abundance of CNO catalysts, and the abundances of these CNO catalysts remains constant until $T > 0.4$ GK wherein breakout reactions (^{15}O(α,γ)^{19}Ne and ^{14}O(α,p)^{17}F) would pull these catalysts out of the CNO cycle permanently. Breakout reactions, however, do not occur in classical novae, since peak temperatures in the hottest classical novae only reach $T \approx 0.418$ GK.

The hot CNO-cycle is thought to generate roughly 70% of the energy in the classical nova burning. At temperatures and densities characteristic of classical novae, (p,γ) and (p,α) reactions will be faster than compared to β^+ decay half-lives. This means that the completion of each hot CNO cycle will be limited by the speed of β^+ decay processes and the rate of energy generation from these cycles depends directly on the β^+ decay steps in each CNO cycle. In the hot CNO1 cycle, the ^{14}O and ^{15}O (p,γ) reactions would lead to the production of ^{15}F and ^{16}F respectively, which are both unstable by proton emission. Thus, the destruction of ^{14}O and ^{15}O are via β^+ decay and the energy generation rate is limited by the β^+-decay half-lives.

While the HCNO1 cycle occurs via a ^{12}C seed nuclei, the HCNO2 and HCNO3 cycles proceed with ^{16}O seed nuclei. In the temperature range of $T = 0.1 - 0.4$ GK, the dominant destruction mode of ^{18}F is by a (p,α) reaction, acting orders of magnitude faster than both the ^{18}F(p,γ)^{19}Ne and ^{18}F(β^+,ν)^{18}O reactions. This means that the HCNO2 and HCNO3 cycles are also closed cycles in that they preserve the number of catalytic seed nuclei in the burning environment. The difference between these two HCNO cycles is the temperature in which they operate; at $T > 0.23$ GK, the ^{17}F(p,γ)^{18}Ne reaction outcompetes the β^+ decay and gives rise to the HCNO3 cycle, which bypasses ^{17}O.

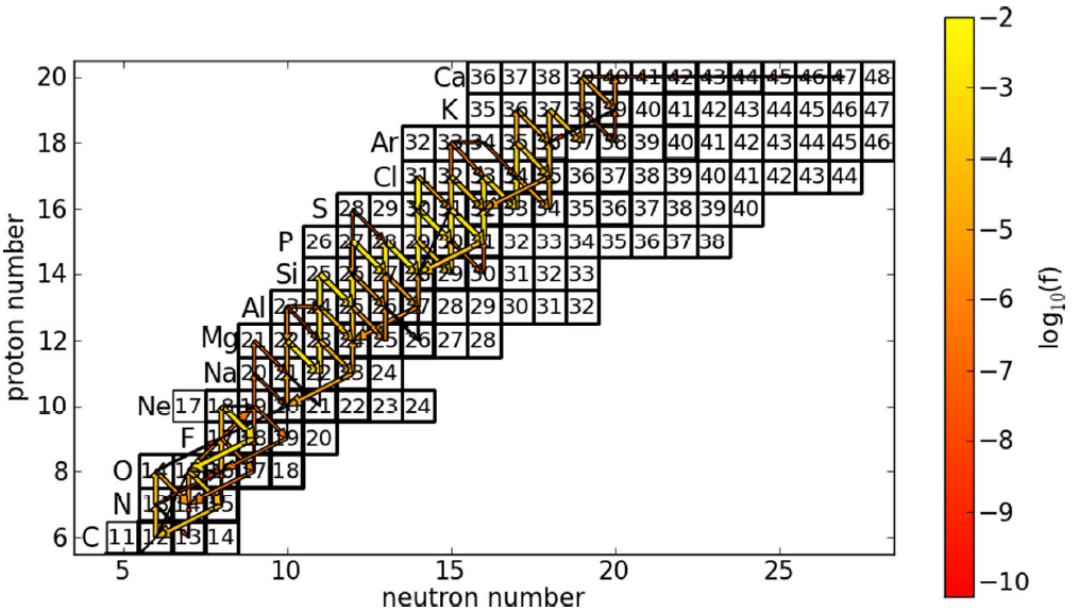

FIGURE 1.6: Nucleosynthesis pathway for accretion onto a ONe white dwarf. A network calculation was performed for the peak temperature of $T_{max} = 0.408$ GK. Arrow thickness and colour represent flux strength. Endpoint of nucleosynthesis is near mass 40. Figure adopted from [13]

Heavier nuclei ($A \geq 20$) can be formed from the mixing of the white dwarf material with the accreted envelope. This mixing can occur from various methods such as 1) convective mixing, 2) shear mixing, and 3) Kelvin-Helmholtz instabilites [11]. These can contribute to dredging up the white dwarf material into the burning shell. The dredged material contains the seed nuclei in the Neon - Silicon mass range [8] which are the precursors for synthesizing elements up to $A \sim 40$ in ONe WD novae. Hydrogen burning with Ne and Na catalysts are another closed cycle (NeNa cycle) that burns hydrogen into helium, however at peak temperatures of ONe novae ($T > 0.25$ GK), the destruction mechanisms of ^{23}Na - (p,γ) and β^+ decay - become equal in rate. Once a seed nucleus reaches ^{24}Mg from the ^{23}Na(p,γ)^{24}Mg proton capture reaction, it leaves the NeNa cycle and forms heavier elements via proton captures and subsequent β^+ decays. Figure 1.6 shows the nucleosynthesis pathway of an ONe nova with peak temperatures of 0.408 GK. The endpoint of these reactions theoretically ends at the $A \sim 40$ region, and indeed several observations of spectroscopic abundances in nova shells show Si, S, Cl, Ar, and Ca, with no observed overproduction of elements heavier than Ca [8].

Astronomical observations of elemental abundances for Ar and Ca in ONe novae

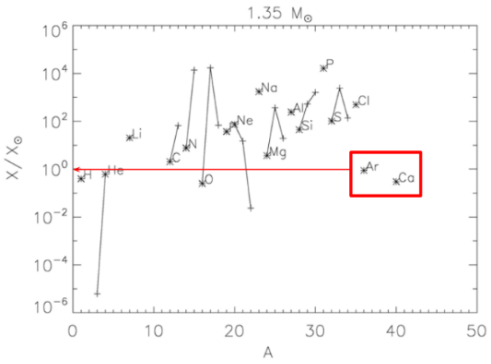

Element	Sun	QV Vul (1987)	V2214 Oph (1988)	V977 Sco (1989)	V443 Sct (1989)
H	1.00	1.00	1.00	1.00	1.00
He	1.0 e-1	1.1 e-1	1.9 e-1	1.9 e-1	2.3 e-1
N	9.5 e-5	1.1 e-3	6.4 e-2	5.9 e-3	7.8 e-3
O	8.1 e-4	3.8 e-3	1.1 e-3	3.7 e-3	9.0 e-4
Ne	1.1 e-4	7.3 e-5	2.5 e-3	2.5 e-3	1.4 e-5
S	1.7 e-5	4.1 e-6	9.7 e-5	-	2.4 e-5
Ar	3.7 e-6	-	5.5 e-5	5.3 e-5	1.8 e-5
Ca	2.2 e-6	-	9.4 e-5	1.6 e-5	1.0 e-5
Fe	4.2 e-5	2.3 e-5	6.5 e-4	4.8 e-5	2.8 e-5
Z	0.019	0.05	0.37	0.08	0.06

FIGURE 1.7: A comparison of endpoint nuclide abundances, argon and calcium, from model calculations and astronomical observations. On left: Adopted from [15], model simulations show that the argon and calcium abundances are close to solar values. On right: Adopted from [14], the observed abundances of argon and calcium compared to solar values from various WD novae compared to solar values - an order of magnitude enhancement exists in the WD ejecta compared to solar values.

ejecta show an overall enhancement with respect to solar values by a factor of ~ 10 [14]. In contrast, hydrodynamic simulations with nuclear reaction rate networks produce abundances of Ar and Ca close to solar values [15]. Figure 1.7 shows this discrepancy between these works. This discrepancy is the main motivation behind the spectroscopic studies conducted in this work.

One clue into resolving this discrepancy comes from a sensitivity study performed by Iliadis et. al. [2]. In this work, the rates of various reaction rates were varied about their uncertainty one reaction at a time and the impact of that variation on the abundances of nuclides was observed. These uncertainties are typically a factor of 100 as an upper limit and 0.01 as a lower limit for reaction rates determined with Hauser-Feshbach calculations. The Hauser-Feshbach method is an averaging method to find cross sections in excitation energy ranges with high level density. In the environments of classical novae, the cross section is dominated by isolated, well separated, single resonances. Thus the maximum uncertainty - the upper and lower limits of the possible rates - is typically used. When varying the ^{38}K(p,γ)^{39}Ca reaction rate about its uncertainty, it was observed that the abundances of ^{38}Ar, ^{39}K, and ^{40}Ca changed by a factor of 24, 58, and 57 respectively [16]. It should be noted that these isotopes are stable and in the case of potassium and calcium, the most abundant isotopes of that element.

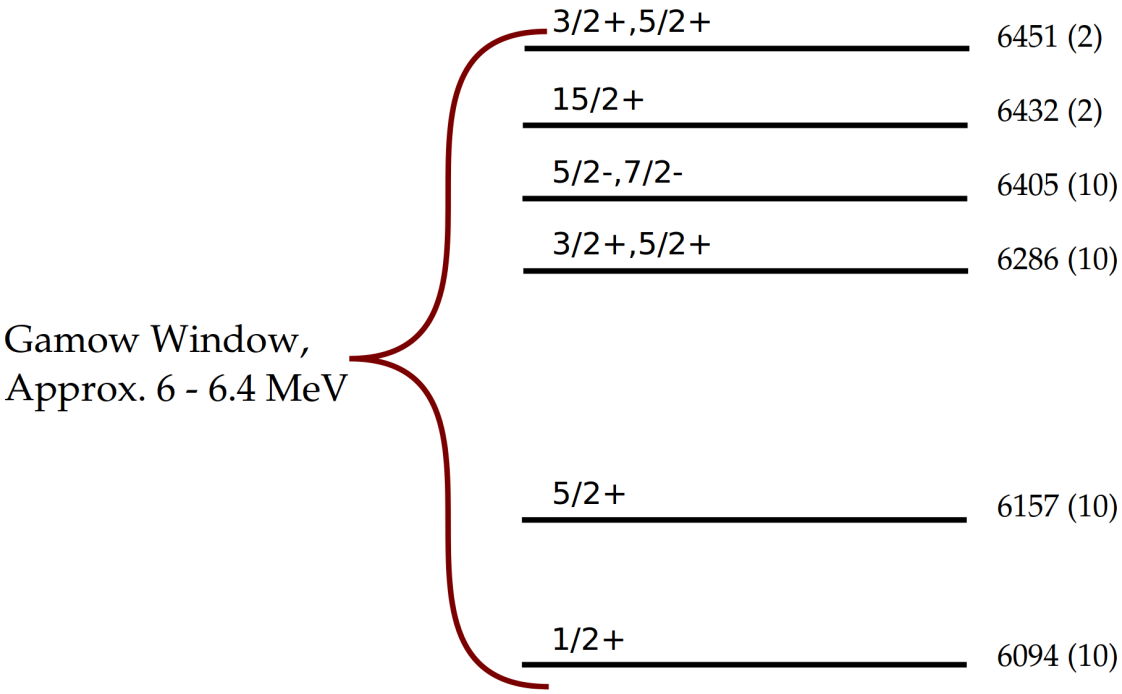

FIGURE 1.8: Gamow window schematic with ENSDF[17] evaluated energies of ^{39}Ca prior to the experiments in this work, and after the DRAGON direct measurement.

1.3.4 Importance of ^{39}Ca and previous studies

The ^{38}K(p,γ)^{39}Ca reaction operates via ℓ=0 resonance reactions within the Gamow window in classical nova peak temperatures. The Gamow window for this reaction at a temperature of 0.4 GK is 0.321-0.614 MeV, with a Gamow peak of 0.468 MeV. Combining this with the Q-value of the reaction Q = 5.7709(1) MeV, the most astrophysically important resonance energies in ^{39}Ca that will be populated by this reaction are between 6.0-6.4 MeV. There are a handful of states that lie within this region. Since the nuclear interactions are at a low energy, $\ell = 0$ transfer reactions will be the most dominant. Given the J^π of ^{38}K and proton are 3^+ and $1/2^+$, states with $J^\pi = 5/2^+$ and $7/2^+$ are the most important. This condition is met for exactly three states: 6.451(2), 6.286(10), and 6.157(10), which have $J^\pi = 5/2^+$. Figure 1.8 shows these states schematically.

The first attempts to directly measure this reaction rate were carried out by the DRAGON (Detector of Recoils and Gamma-rays of Nuclear reactions) collaboration at TRIUMF [18]. The reaction proceeds via resonance reactions within the Gamow window at nova temperatures (0.4 GK). The objective of the experiment was to find

resonance strengths of three $\ell = 0$ resonances lying within the Gamow window in order to ultimately deduce the reaction rate of this astrophysically important reaction. Given the spin and parity of ^{38}K and a proton in their ground state (3^+ and $1/2^+$ respectively), reactions proceeding through resonant states in ^{39}Ca with a spin and parity of $5/2^+$ or $7/2^+$ would likely be the most dominant. These resonances were at energies of: 6.157(10), 6.286(10), and 6.460(10) MeV in the ^{39}Ca nucleus before the experiment. During the DRAGON experiment, the resonance strength of only the 6.460(10) MeV state was determined to be $\omega\gamma = 120^{+50}_{-30}(\text{stat.})^{+20}_{-60}$ meV, and upper limits were determined for the other two states. In addition, the 6.460(10) MeV state was observed at an energy of $6.450^{+2}_{-1}(\text{stat.})\pm1(\text{sys.})$ MeV instead. The large uncertainties associated with resonance energies could affect the measurement process as follows: The radioactive ^{38}K ion beam produced at the ISAC-1 facility [19] impinged on a windowless hydrogen gas target of the DRAGON setup [20]. A beam energy was selected for each resonance such that the beam would impinge on the gas target and produce that resonant reaction within the gas target. To handle the beam energy width, a gas pressure and temperature of 10.6 mbar and 298 K respectively [16] were chosen so that the stopping power effects would cause the distribution of resonant events to be centered in the gas target. If the resonance energies are of large uncertainty then the centroid of this distribution can occur off the center of the gas target. The data set on the right side of Figure 1.9 shows how this can manifest. The centroid of the distribution of event positions (blue dots) on the z-axis (direction of beam) is downstream of the center of the gas target. A best-fit simulation (orange line) shows that the resonance observed is at a beam energy of $E_r = 679^{+2}_{-1}(\text{stat.})\pm1(\text{sys.})$ keV instead of the previously evaluated value of $E_r = 689\pm10$ keV [21]. Worse yet, the resonance could be totally missed if the energy of the beam is too high or low. The energy window that can be covered by the gas detector is seen in the left plot of Figure 1.9, and is approximately 30 keV wide.

Further spectroscopic studies were done in response to this measurement. A γ-ray measurement was carried out by Hall et. al. [22] with Gammasphere ORRUBA Dual Detectors for Experimental Structure Studies (GODDESS) and a ^{39}Ca charged particle reaction study was carried out by Setoodehnia et. al. [23] using the ^{40}Ca(^{3}He,α)^{39}Ca reaction. The latter used the same detector system that will be described in subsection 2.2.5. The results from these works will be compiled in the results section.

The work in this thesis is motivated by the need to increase the precision on these

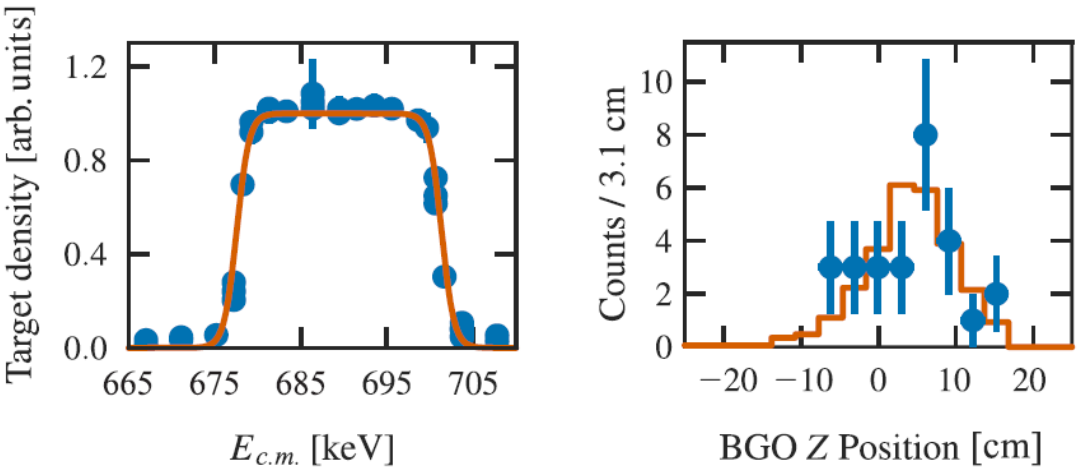

FIGURE 1.9: Figures from [16], data for a ^{38}K beam energy of 27.17 MeV to produce events from the 6.460(10) MeV resonance in ^{39}Ca. **On left**: Gas density in target as a function of center-of-mass beam energy. Blue dots denote measured densities, while the orange line is a density profile function that was fitted to the points. **On right**: Distribution of z-positions of observed events in the gas target using γ-events in coincidence with recoil events. Blue denotes number of measured events, while the orange line denotes a best-fit simulation with $E_r = 679$ keV and $\omega\gamma = 120$ meV The centroid of the distribution occurs downstream of the center of the target, suggesting that the beam energy chosen was too high, and the resonance observed is at a lower energy than previously thought.

^{39}Ca states in order to further understand the nucleosynthesis in classical novae. We carried out the ^{40}Ca(d,t)^{39}Ca, and the ^{39}K(^{3}He,t)^{39}Ca reactions in order to populate states in ^{39}Ca.

Chapter 2

Experimental Methods

Two reactions to populate states in ^{39}Ca were explored in two separate experiments. The first is the ^{40}Ca(d,t)^{39}Ca reaction performed at the Maier Leibnitz Laboratory in Garching, Germany. The (d,t) reaction was chosen as it is a one nucleon transfer, making the angular distribution analysis more straightforward. The (d,t) reaction has also been studied in past, populating the ^{39}Ca states of interest [24]; however, the uncertainties associated with these excitation energies are large (15-30 keV).

The second experiment performed in this work is the ^{39}K(^{3}He,t)^{39}Ca reaction at Triangle Universities Nuclear Laboratory (TUNL), in North Carolina, USA. This experiment was chosen since it has the advantage of being non-selective in the states of ^{39}Ca that it populates. This reaction was last measured in [25]; however, the experimenters did not study the states in ^{39}Ca of astrophysical interest.

In both cases, a major factor in the feasibility is the availability of target and beam. At the very least, the target must be stable to radioactive decay. Another decider is the availability and properties of the chemical element that must be used to produce the target. One particular hurdle that had to be overcome was the risk of oxidation in targets, which will be discussed in this section. When considering the beam, the strength of the beam current is important. A high current is desired to be able to gather the necessary statistics within a reasonable time frame. This depends on the facility's ability to produce a particular beam. Deuteron and ^{3}He are beams that have been historically producible with good beam strength and stability.

2.1 The ^{40}Ca(d,t)^{39}Ca experiment

2.1.1 The Maier Leibnitz Laboratory in Garching

The purpose of this experiment was to obtain precise energies for the astrophysically important resonances of ^{39}Ca for endpoint nucleosynthesis in classical novae. This section covers the experimental setup and descriptions of the apparatuses used for the ^{40}Ca(d,t)^{39}Ca experiment carried out at the Maier Leibnitz Laboratory. These include: the ^{2}H ion source, the 14 MV MP-Tandem accelerator, the target chamber and fabrication of targets, the Q3D spectrograph, and finally the various detectors used.

2.1.2 ^{2}H ion source

The purpose of this section is to explain the production of negatively charged deuterons before they are accelerated through the MP-Tandem accelerator. A diagram is located in Figure 2.1.

Neutral, molecular deuterium D_2 is moved into the dissociator as an atomic jet created by adiabatic expansion through an aluminum nozzle cooled to 80K. The main purpose of the dissociator is to separate the molecular deuterium into atomic deuterium by electron impacts onto the deuterium molecules. This is achieved by applying a 13.5 MHz radio frequency (RF) field from a high frequency AC circuit within the cold deuterium plasma [26]. This causes the electrons to oscillate in a helical orbit. These electrons impact the molecular deuterium, and break the molecular bonds with an efficiency of $77 \pm 5\%$. At the 10 mm diameter entrance aperture of the Electron Cyclotron Resonance (ECR) ionizer, a beam of 5×10^{15} atoms/s can be seen.

Next, the beam of deuterons passes through an additional pumping stage, which reduces the scattering of the beam from residual gas and enhances the beam intensity by about 20%. It then passes to the ECR ionizer.

The main purpose of the ECR ionizer is to remove the existing electrons from the neutral deuterium atoms. This will be important when moving to the cesium vapour jet in the next stage. An axial magnetic mirror field is applied by two pancake coils and the magnetic field forms a minimum-B structure. This minimum-B structure has a minimum magnetic field of 87.5 mT in the middle of the ECR chamber, while having maxima of 140 and 160 mT at the edges. This axial field confines the plasma to the chamber,

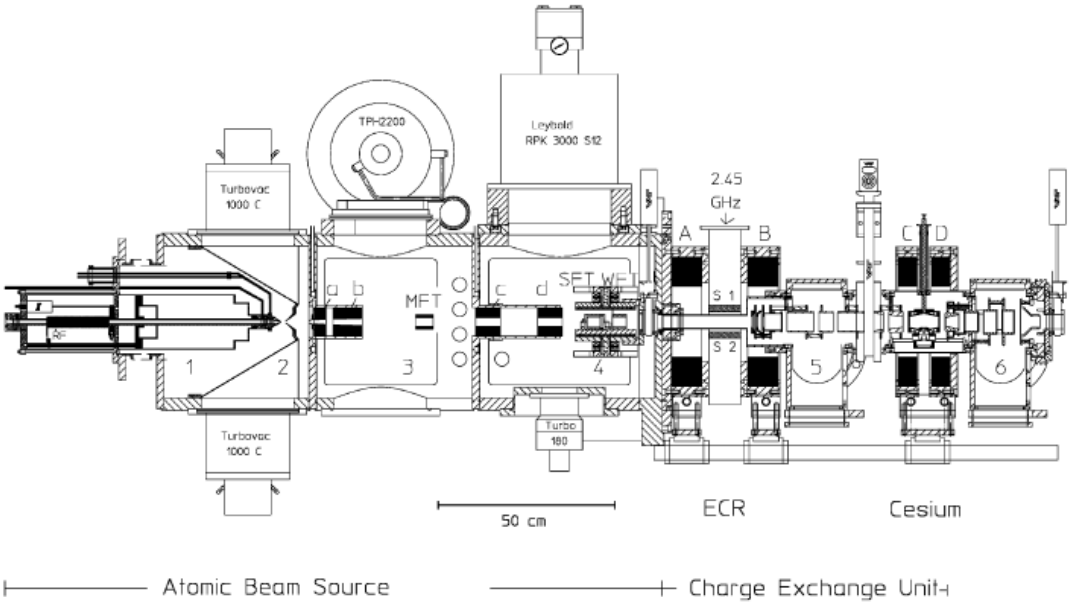

FIGURE 2.1: Vertical Cross section of the ion source, consisting of the Atomic Beam Source (ABS) and the Charge exchange unit. The ABS consists of the dissociator in vacuum section 1, with differential pumping sections labelled 1-4. Sextupole magnets are labelled at a-d which are used for creating polarized beams, but were not necessary for this experiment. The Charge exchange unit consists of the Electron Cyclotron Resonance (ECR) ionizer, and cesium sputter. Figure adopted from [27].

while a radial field is supplied by a set of 6 Iron-Neodynium-Boron (FeNdB) sextupole magnets. A 2.45 GHz RF field is also applied to the plasma, which resonantly accelerates electrons that are in the vicinity of the 87.5 mT magnetic field. Collisions between these electrons and the deuterium atoms ionize the deuterium, producing positively charged ions of deuterium. The efficiency of ionization is a few percent. The deuterium beam is then extracted from the plasma in two steps by three electrodes, and focused by an einzel lens and two deceleration electrodes before reaching the cesium vapour jet target.

Before being sent to the MP-Tandem accelerator, the ions must be negatively charged, so two electrons must be picked up by the now positive deuterium ions. This is where the Cesium vapour jet target is used [28] . The Cs reservoir is kept at 310 °C [27]. Through expansion of the Cs vapour through a slit nozzle, a supersonic jet is formed. About 30% of the jet makes it to the charge exchange region, where the positively charged deuteron ions pass through. In this region the deuterium will pick up two electrons from the cesium jet. Because Cesium has a low ionization energy of 3.89 eV, it is ideal for providing electrons for the double charge exchange. After passing the charge exchange region, the jet will reach a condensation surface kept at 35 °C where it will condense to a liquid and be recirculated into the jet. For a deuteron beam kinetic energy of 400-500 eV/nucleon, the efficiency of double charge transfer was noted to be 22 %. [27].

2.1.3 The Munich MP-Tandem Accelerator

At the end of the ion source, the kinetic energy will not be high enough to populate the states of interest in ^{39}Ca between 6-6.5 MeV. The purpose of the MP-Tandem is to accelerate the deuterons to the adequate kinetic energy of 24 MeV.

The operating principle is as follows: as the negatively charged ion beam enters the tandem - in our case D^- - it is accelerated towards the positive high voltage terminal. The energy gained by each particle in the beam is given by $E_k = e \cdot V$ as the deuterons are pulled towards the positive terminal. Located within the positive terminal is a foil stripper which will remove electrons [29], leaving the ion carrying a net positive charge. In the case of a deuteron beam, it strips all electrons, leaving the deuteron with a charge of +1. The beam of particles is then accelerated away from the positive terminal, gaining a kinetic energy $E_k = Ze \cdot V$. For deuterons the total amount of energy gained is $E_k = 2e \cdot V$.

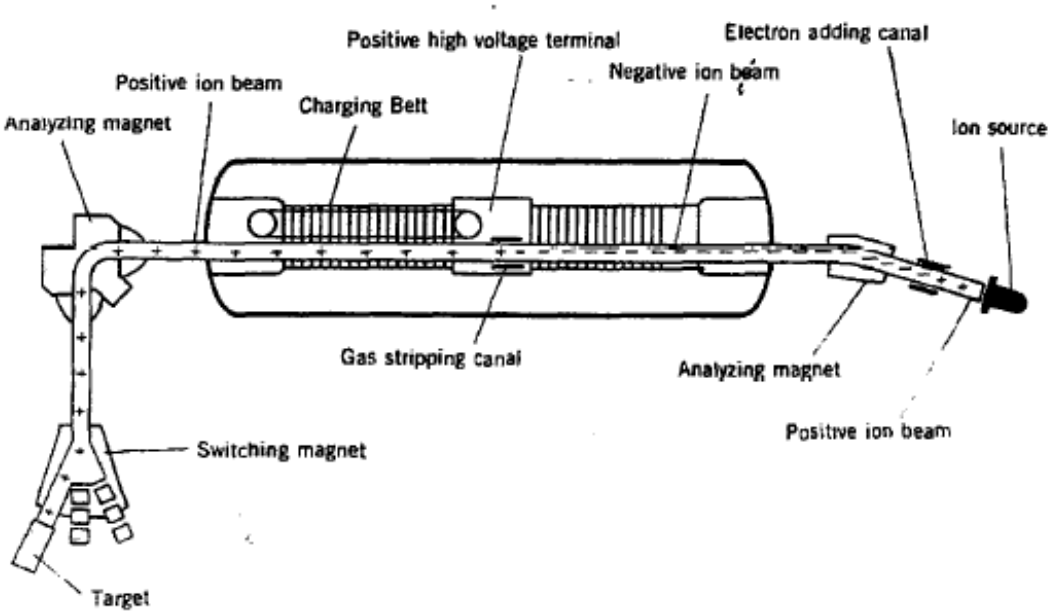

FIGURE 2.2: Schematic of a typical tandem accelerator. Figure adopted from [3]

The beam is then accelerated through a series of electrically insulated tubes kept in high vacuum. In the middle of the structure is the positive terminal which is brought to the nominal voltage by 3 pelletron chains [29]. These chains are made of pellets of conductive material connected by an insulating material and configured into a rotating belt. A single chain can deliver 100 μA of current, through up-charging, and another 100 μA through down-charging as the chain makes contact with the terminal. A total of 600 μA can be delivered from all 3 chains. To maintain a stable voltage without coronal discharging, the terminal is surrounded by an insulating gas. The gas used is a combination of 30 % SF_6 and 70% N_2. After the negatively charged deuteron beam is accelerated towards the positive terminal, the electrons from the deuterons are stripped using a carbon foil, and are now positively charged. These positively charged deuterons are now accelerated away from the terminal.

It is of utmost importance that the energy of the deuterons of the beam is well known, and well constrained. For this reason there is a conventional analyzing magnet with subsequent slit pair as well as a time of flight (TOF) system employed to precisely measure the energy of deuterons exiting the tandem [29]. The momentum and therefore energy of the beam is calculated from the B-field produced by the analyzing magnet

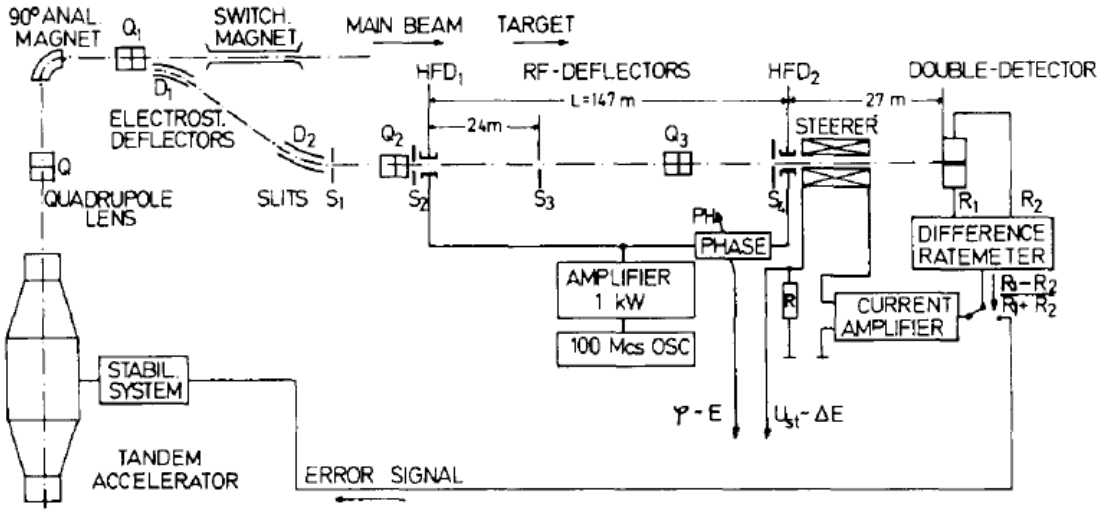

FIGURE 2.3: Time of Flight (TOF) system used to increase precision on beam energy. A portion of the beam is "peeled off" from the main beam and sent through two precisely spaced RF deflectors labelled HFD_1 and HFD_2 which measure the TOF, and thus the energy of the beam particles. Figure adopted from [29]

which is measured with a nuclear magnetic resonance (NMR) probe in the magnet's operating region, and the radius of curvature ρ of the particles as they are bent through the magnet, which is measured with the subsequent slits. The magnetic field can be determined to a precision of order 10^{-4}, since the field of even high-quality iron magnets may have varying fields away from the location that the NMR probe reads out the magnetic field. The positions determined from the current on the slits can be found with a precision of a few parts in 10^4 due to asymmetries in the beam profile and changes in the ion source conditions.

The TOF system employs a set of two electrostatic deflectors to peel off a fraction of 100 nA from the main beam and send it through two identical high frequency resonators separated by a carefully measured distance of $L = 14711.89 \pm 0.03$ cm. The time of flight information can provide energy values to a precision of 1.5×10^{-5} with 20 MeV protons, and can typically give values for energy resolution on the order of $\Delta E/E = 2 \times 10^{-4}$

2.1.4 Target Chamber

After being accelerated by the MP-Tandem, the deuteron beam will then collide with various thin target foils where nuclear reactions of interest will happen. This section will

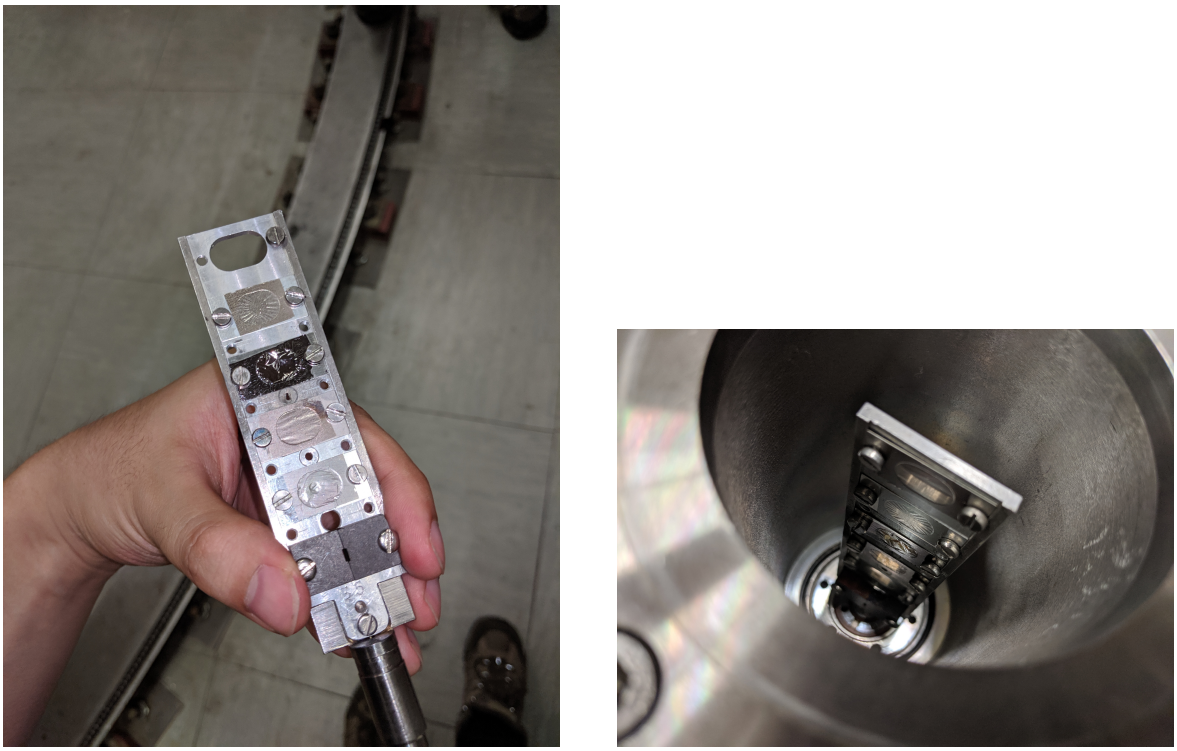

(a) (b)

FIGURE 2.4: a) Target ladder from top to bottom: ^{13}C background target, CaF_2 thick production target, ^{32}S implanted calibration target, CaF_2 thin production target, LiF background target, collimator. b) Target chamber in which the target ladder is inserted. The chamber is pumped down to high vacuum (10^{-6} torr).

discuss the targets and related equipment.

A target ladder is shown in Figure 2.4. The fabrication details of the ^{40}Ca production target which produces the reactions of astrophysical interest will be discussed in subsection 2.2.4. 30 μg/cm^2 of natural calcium fluoride (CaF_2) was evaporated onto an isotopically pure ^{12}C backing of 12 μg/cm^2. Care was taken in choosing the compounds used for the target and backing. SpecPlot simulations (see section 3.1) of the focal plane had shown that tritons from the ^{13}C(d,t)^{12}C is a potential contaminant in the focal plane spectrum, hence the use of the isotopically pure ^{12}C backing which does not contribute tritons to the spectrum. Another contaminant are tritons from the ^{16}O(d,t)^{15}O reaction which can occur from an unavoidable oxidation of metallic calcium. SpecPlot simulations showed these would produce large peaks on the focal plane, and can also change the thickness of the target to an unknown degree. To that end, we chose to use

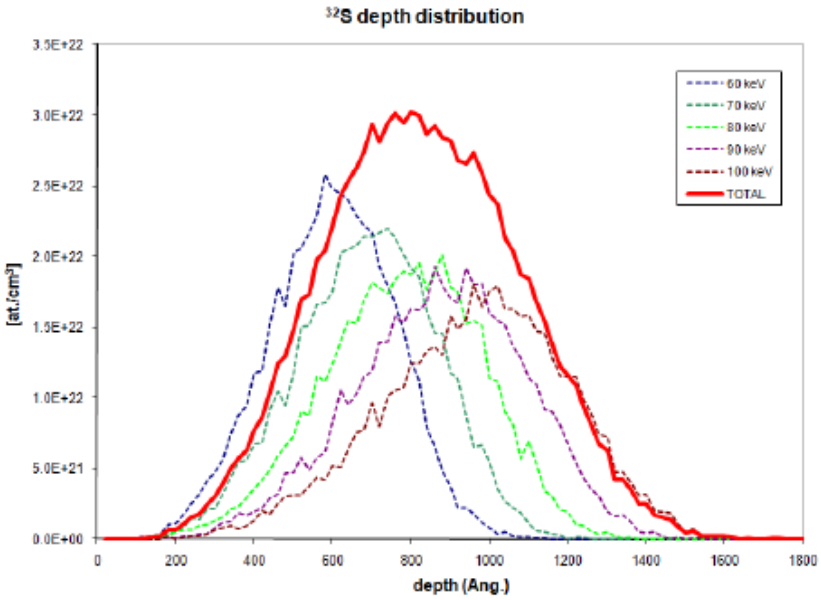

FIGURE 2.5: SRIM simulation of depth profile for implanted ^{32}S target. Figure adopted from [30].

CaF_2 to avoid oxidation.

A ^{32}S target was fabricated in order to calibrate the focal plane position axis to the energy of the residual nucleus. A ^{32}S target was chosen since: 1) it was accessible and already at the facility, stored in a target closet; 2) the similar mass would mean both this target and the ^{40}Ca production target would exhibit similar kinematic broadening; 3) the thicknesses of this target and the production target were similar so energy loss patterns would be similar between them; 4) ^{31}S, the residual nucleus of the (d,t) reaction, has a well studied level structure, and peaks of tritons from energetically separated states would appear in our focal plane given our experimental parameters; 5) the nature of implanted targets means that there will likely be very few contaminants. The ^{32}S calibration target was fabricated through the ion implantation technique. The target was prepared at the Lennard-Hendricks Laboratory at Western University in Ontario, Canada [30]. The goal of the implantation method is to embed ^{32}S nuclei into a carbon foil with a well defined abundance vs. penetrative depth profile. A beam of ^{32}S was accelerated by a Tandem Van de Graaff accelerator and deposited in a layer of 40 $\mu g/\text{cm}^2$ 99% isotopically pure ^{12}C mounted on a glass slide. The abundance vs. penetrative depth profile was chosen to be a Gaussian distribution. To that end, the incident beam energy

and dose were varied to create the depth distribution. The dose, D, is calculated from the total charge q_c from the relation:

$$q_c = D \times q \times e \times \text{aperture area} \tag{2.1}$$

Using SRIM simulations [31] for stopping power and ranges of ions in matter, the optimal incident energies and doses were determined to produce a target with a Gaussian depth distribution. Incident beam energies of 100, 90, 80, 70, and 60 keV were chosen, and the thickness of the target can then be calculated by:

$$\Delta x = \frac{D \cdot M}{N_A} \tag{2.2}$$

where M is the molar mass of ^{32}S in units of g/mol, while N_A is Avogadro's number. A Rutherford backscattering measurement was performed to quantify the thickness of the target, yielding a value of 11.7(5) μg/cm^2. The results of the SRIM simulation can be seen in Figure 2.5

The ion-implanted foil can then be floated off the glass slide into distilled water and picked up by the target frame. More details and figures of the floating process can be found in the evaporation method section. The target was then stored in 2011 at the MLL until used by our experiment in 2017.

Five targets were mounted onto the target ladder along with a collimator. These targets are listed in Figure 2.4 and fastened to the ladder. Once the ladder is loaded, it is inserted into a chamber downstream of the tandem as seen in Figure 2.4. The chamber is sealed and slowly pumped down to a pressure of 5×10^{-6} torr so the foils do not tear. The ladder structure is convenient, as a motor is located beneath the target ladder which allows it to move in the vertical direction into a smaller vacuum sealed cylinder that can be independently vented. This allowed us to change the target without needing to break vacuum to open the target chamber. The target ladder can also be rotated to accommodate the movement of the Q3D spectrograph downstream. The benefit of this rotation is that at higher Q3D angles the count rate (which typically get poorer at higher Q3D angles) are increased, as the target will have a higher effective thickness.

The effective thickness is given by:

$$\Delta x_{eff} = \frac{\Delta x}{cos\theta} \tag{2.3}$$

where δx is the thickness, and θ is the angle of rotation. The downside, however, is that the energy resolution of states will become worse due to straggling in a thicker target. As the deuterons interact with the target, it can potentially undergo the nuclear reaction of interest in the front of the target or the back. A schematic of this is shown in Figure 2.6. If the tritons created from the reaction are formed in the front of the target, closer to the tandem, the triton will pass through the target. The energy loss from the triton passing through the target will be different than if the reaction were to happen at the back of the target since the deuteron will pass through the target instead, yielding a different energy loss. These effects will be manifested through a wider full width at half maximum of the peaks in the triton spectra we will observe.

After the target there is a carbon Faraday cup located at the 0° position. Carbon was chosen as the Faraday cup material since 1) it has low thermal conductivity, so it does not overheat during use 2) it is low Z, so when the beam impinges on it, not many electrons are ejected from the carbon. This is important because allows us to gain an accurate measure on the current of the beam passing through the target. The amount of light reaction products interacting with the Faraday cup is negligible compared to the number of deuterons simply passing through any given target with no nuclear interactions, so the cup reading can be used as a measurement of the beam current. The beam current throughout this experiment was typically 200-600 enA.

2.1.5 Q3D Magnetic Spectrograph

In order to obtain high precision excitation energies of ^{39}Ca, the kinetic energies of the reaction products from the reaction of interest must be known to a high precision. Therefore, if we know the energy of the beam, the Q-value of the reaction, and we experimentally find the energy of the triton from the reaction, we can deduce the excitation energy of the ^{39}Ca that is populated - signifying the resonance energy in ^{39}Ca.

To this end, a Quadrupole-Dipole-Dipole-Dipole (Q3D) magnetic spectrograph is employed. The purpose of this instrument is to apply magnetic fields to momentum analyze the tritons coming from the experiment.

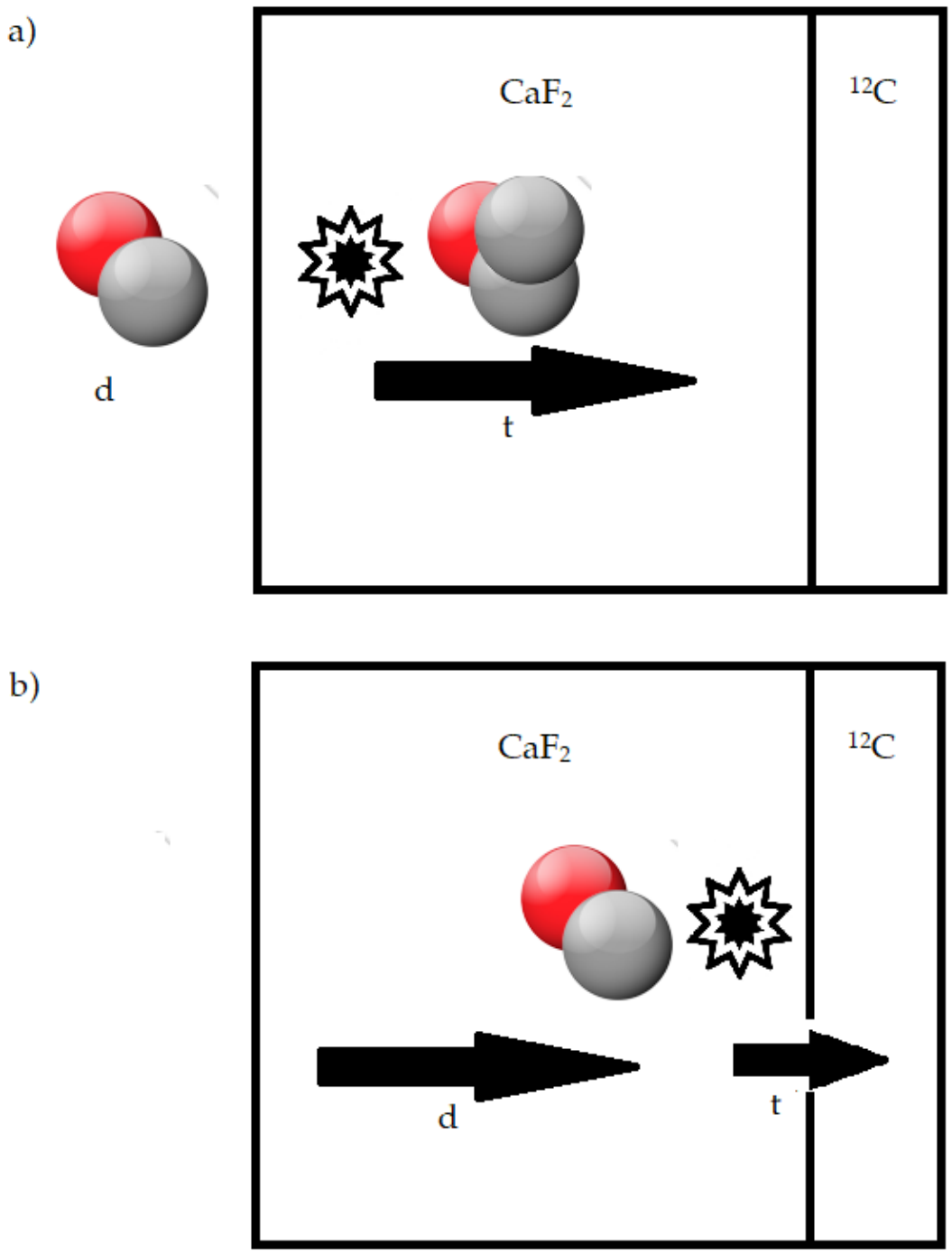

FIGURE 2.6: Schematic of incoming deuteron interacting with CaF_2 target. a) Deuteron interacts with the front of the target, triton loses energy passing through the target. b) Deuteron passes through target and interacts at back of target. Deuteron loses energy passing through the target. Different energy losses are associated with each specific particle moving through the target.

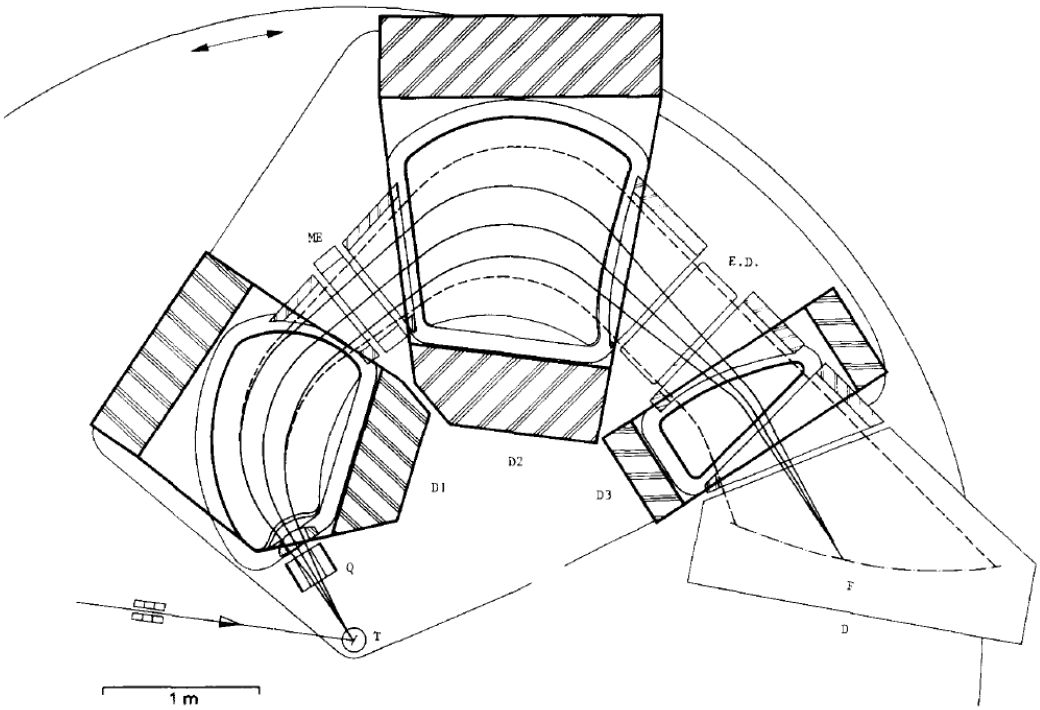

FIGURE 2.7: Schematic of the Quadrupole 3x Dipole (Q3D). Light reactions products are produced from nuclear interactions in the target chamber labelled T, and enter into the quadrupole, labelled Q. The Quadrupole element focuses the products in the vertical direction while defocusing them in the horizontal direction. The light reaction products then enter the momentum analyzing dipoles labelled D1, D2, and D3. Finally they reach the focal plane detector and their positions are detected. Figure adopted from [32]

The operating principle of a magnetic spectrograph is as follows: The Lorentz force on a particle of charge q and velocity v is given by:

$$\vec{F} = q \cdot \vec{v} \times \vec{B} \tag{2.4}$$

Since the magnetic force acts perpendicularly to the velocity of the particle, it will do no work on the particle, meaning the kinetic energy of the particle will remain the same through travel through the magnetic field. These fields are generally perpendicular to the direction of motion, and cause a centripetal acceleration:

$$\frac{mv^2}{\rho} = qvB \tag{2.5}$$

where ρ is the radius of curvature that the particle travels. The product $B\rho$ is colloquially referred to as the magnetic rigidity, and is given by:

$$B\rho = \frac{mv}{q} \tag{2.6}$$

As reaction products of varying energies are moving through a magnetic field of a known value, their trajectories will be bent according to their momentum to charge ratio. For tritons, their positions on the focal plane will then give information on the momenta, and thus their kinetic energies.

After light reaction products are generated from the target chamber, they will pass through to the Q3D located directly downstream as seen in Figure 2.7 [32, 33]. The first section the particles pass through is the quadrupole magnet. The quadrupole magnet acts to defocus charged particles in the horizontal direction and focus the charged particles in the vertical direction. The end result is a horizontal plane of the reaction products. The dipole magnets create a homogenous magnetic field to bend the particles and momentum analyze the particles based on their momentum-to-charge ratio through the mechanisms outlined above. Once momentum is analyzed, the particles are finally focused on the focal plane upon entering the detector suite.

There are a few considerations taken to optimize the separation of the momentum analyzed particles, and therefore the energy resolution. The energy resolution can be

thought of as the ability to resolve two particles of slightly different momentum to charge ratio. Quantitatively, the resolution $\frac{p}{\Delta p}$ it is defined as:

$$\frac{p}{\Delta p} = \frac{DR}{M_H x_0} \tag{2.7}$$

where R is the nominal radius of curvature, D is the nondimensional dispersion, M_H is the magnification in the median plane, and x_0 is the target spot size in the dispersive plane [32]. The design of the successive dipole magnets allows for a greater degree of dispersion, which aids the overall energy resolution. Another factor is the effect of kinematic broadening. This effect arises when two tritons produced from the population of the same state appear to have different energies due to a difference in emission angles. Kinematic broadening is corrected through a multipole element, which creates a simultaneous dipole, quadrupole, sextupole, octopule, and decupole field. Overall, the energy resolution from the Q3D is reported to be $\Delta E/E = 2 \times 10^{-4}$, which is on par with the energy resolution of the tandem. A schematic view of the Q3D is shown in Figure 2.7.

To maximize the statistics, the full acceptance angle into the Q3D of 13.9 msr was used. The tradeoff, however, is the loss of resolving power due to aberrations.

2.1.6 MLL Detector Suite

Once the momentum of the light reaction products has been analyzed, we need to detect them in order to 1) separate the tritons from other light reaction products such as deuterons, protons and α particles and 2) determine the positions of the tritons from the reactions in the target.

This section will cover the detector suite used in the experiment which is composed of a series of wire proportional counters, a position sensitive cathode strip detector, and a scintillator. These instruments are all housed in a sealed container filled with isobutane gas. The combination of these elements is used to fulfill the purposes listed above, and a schematic diagram of the detector is shown in Figure 2.8 [34].

The operational principle of a wire proportional counter is as follows: as a particle enters the detector chamber, it deposits energy into the surrounding isobutane gas, which ionizes it, creating multiple ion electron pairs [35]. An anode wire is present, which is held at a high positive voltage, along with cathode strip foils on each side of it, held

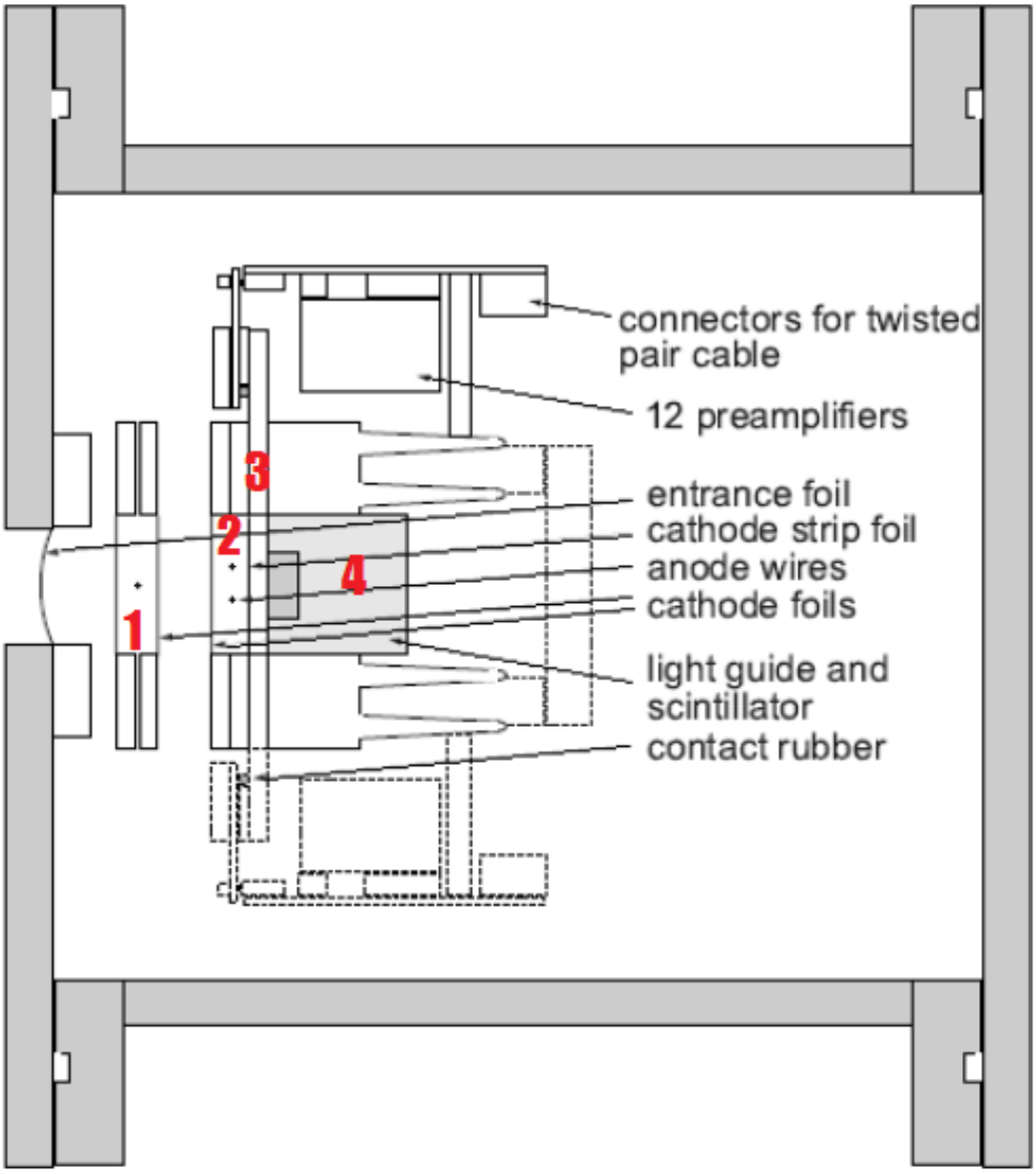

FIGURE 2.8: A vertical cross section (side view) of the detector suite used at MLL. As beam enters through the kapton foil on the left, it passes through 1) single wire proportional counter 2) multiwire proportional counter 3) position-sensitive cathode strip detector 4) plastic scintillator. Figure adopted from [34].

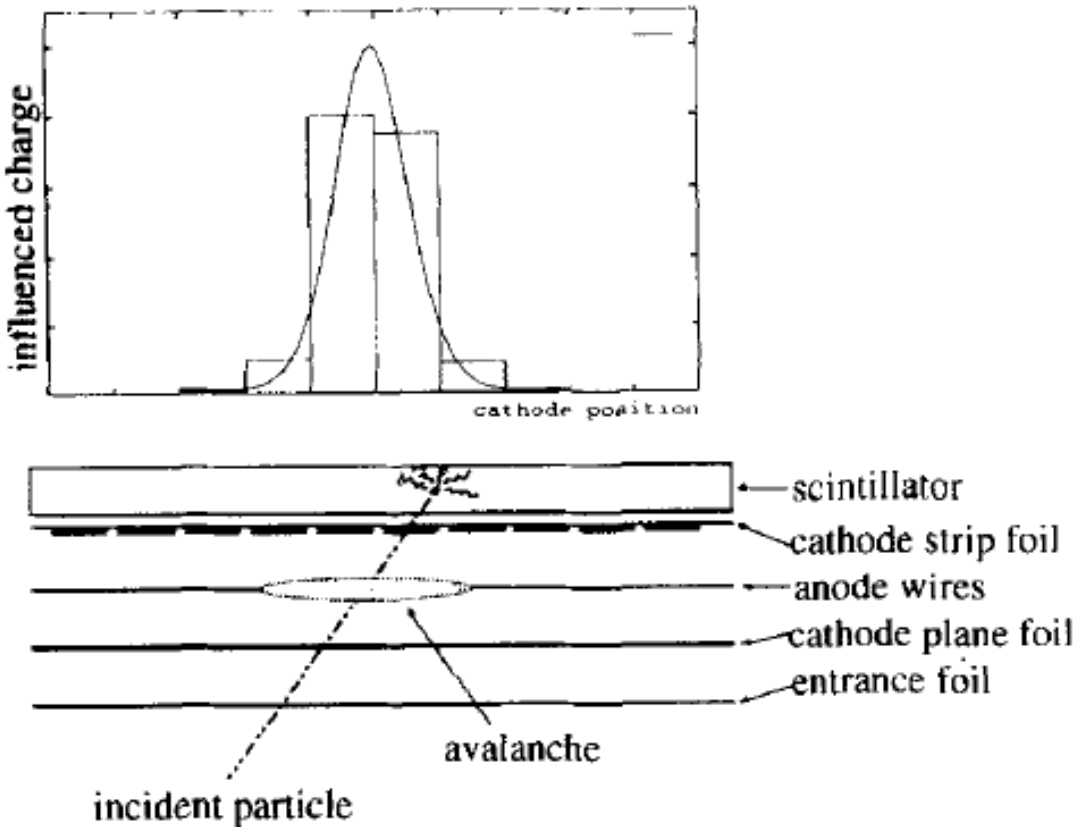

FIGURE 2.9: Schematic of the function of the cathode strip detector used at MLL.Figure adopted from [34]

at ground. When the liberated electron is in the presence of the anode wire, it will be accelerated towards the wire, ionizing additional ions. This multiplicative ionization is known as an electron avalanche[36]. The charge induced by the positive ions generated from the electron avalanche is the main contributor behind the signal detected from the charged particle passing through. A schematic of this process can be seen in Figure 2.9.

A powerful capability of these detectors is that the amount of charge induced is proportional to the energy deposited by the incident particle. This means that it can be used as a means of particle identification.

The position-sensitive cathode strip detector operates as follows: 255 electrically isolated cathode strips that are 3.5 mm in width and separated by 0.5 mm are arranged to cover 890 mm of the 1800 mm curved focal plane of the Q3D [37]. The particles pass through the focal plane at an angle of $40° - 50°$ which will induce charge in about 6

strips. The cathode strips closest to the ionization event will have the highest induced charge, and a ”center-of-mass" calculation can be used to find the position at which the charged particle passed the focal plane.

Finally, a plastic scintillator is located at the end of the detector setup. These are generally composed of a scintillating material which is connected to a photomultiplier or a light guide. As radiation passes through the scintillator, it excites the atoms and molecules in the material, and light is emitted [35]. This light is picked up by the photomultiplier tube which turns it into a photoelectric current that is amplified by an electron multiplier system. Due to its fast timing properties, it acted as part of a trigger for data acquisition. It also took energy measurements of the light reaction products for use in particle identification.

When a particle reaches the detector setup after the Q3D, it firsts passes through the 25 μm thick Kapton foil at the front of the detector housing. As it moves through the detector, it ionizes the isobutane gas held at a pressure of 500 mbar [34]. It then passes through the single wire proportional counter, consisting of a cathode foil and anode wire, depositing an amount of energy $\Delta E1$ which can be detected by the device as explained above. The gold plated tungsten anode wires in the experiment were all nominally set to 1300 V, and adjusted as needed by $\sim$ 50 V during the experiment. The particle then moves through a cathode foil, a gas filled region, and then another cathode foil. Both foils of aluminized mylar are of thickness 2.9 μm. It then passes through a two-wire proportional counter, depositing an amount of energy defined by ΔE in the same fashion as the previous wire proportional counter. During the experiment, this detector was also used to center the detector, since both wires should theoretically have the same amount of charge induced. It then passes through the cathode strip detector where it induces charge on the nearest strips, giving position data on the particle. After passing one last cathode strip foil, it reaches the plastic scintillator where the rest of the energy, E is deposited and detected.

2.1.7 Electronics and DAQ

This section will cover the electronics DAQ associated with the detectors listed above, most importantly those associated with the position sensitive cathode strip detector.

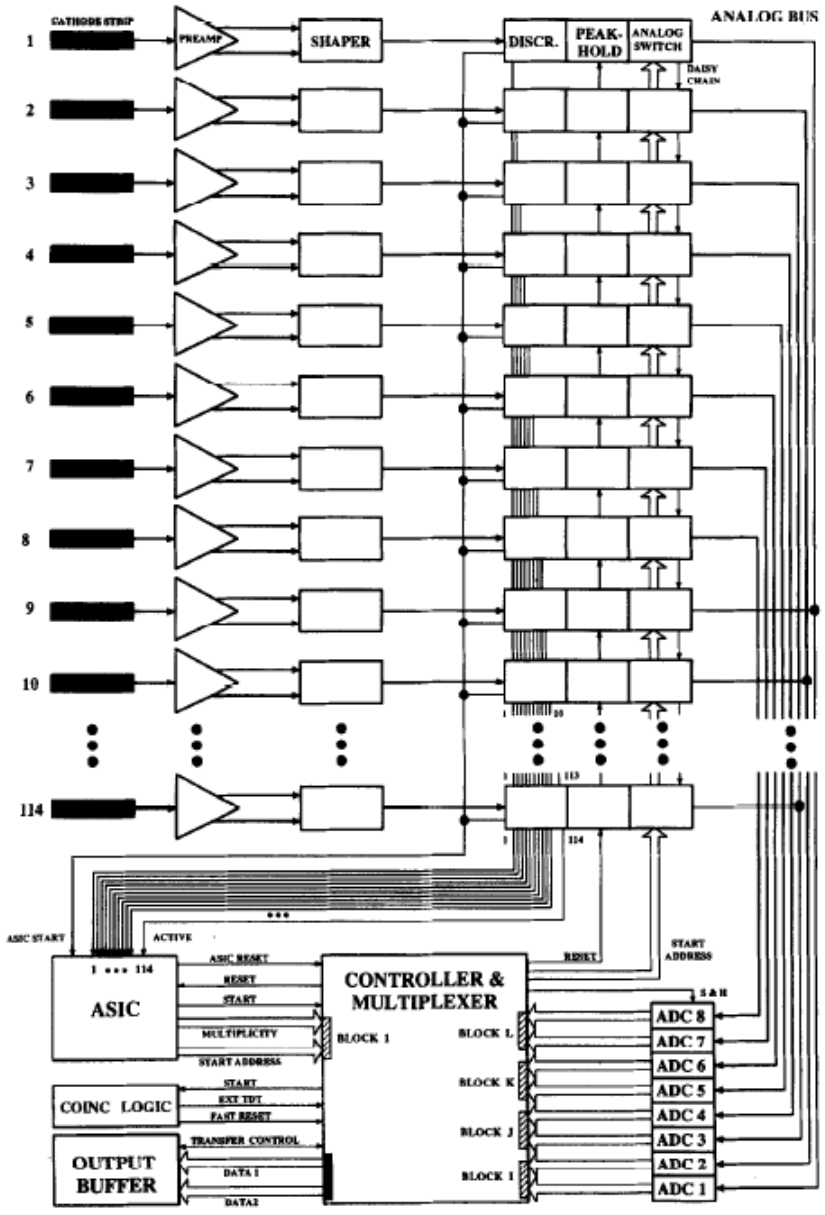

FIGURE 2.10: Schematic of the electronics setup to process the signal from the detectors. Figure adopted from [37].

Each cathode strip in the detector suite is given its own preamplifier and pulse shaper. Events are recorded when they show a multiplicity of 3-7. The multiplicity is defined by the number of strips that fire in the event. Since the focal plane is offset by $40 - 50°$ degrees relative to the Q3D exit [37], a charged particle will come in at an angle not perpendicular to the focal plane inducing charge in multiple cathode strips as it passes through. The advantage to this is twofold: firstly, it allows us to generate a coincidence trigger that will be explained below. Secondly, it improves the resolution of the position spectrum. If it were only to arrive perpendicularly to the focal plane the resolution of the position spectrum would be limited to the size of a single cathode strip; however with multiple strips firing, the final position of the charged particle can be interpolated from the composite signal .

To carry out this multiplicity determination task, an application specific integrated circuit (ASIC) is used. When a cathode strip signal above the discriminator threshold is measured, a logic signal is sent to the ASIC. If the required number of strips are fired in coincidence, the ASIC will determine that it is indeed a true event. This is used as a first level of background subtraction.

A second coincidence test between the position signal, the energy-loss signal from the anode wires, and energy-rest signal from the scintillator is carried out. This test takes place during the pulse shaping and multiplicity test which takes 2.5 μs to carry out. This is the second level of background subtraction. A schematic of the DAQ can be seen in Figure 2.10.

We will now discuss the MARABOU[38] (MBS And Root a Based Online-Offline Utility) system, the data acquisition and analysis system used at MLL. It consists of a front end, which is responsible for data readout, event building, and data transport based on the Multi Branch System (MBS); and a back end, responsible for setup, run control, histogramming, data analysis, and data storage using the ROOT data analysis framework[38]. The ROOT back end is used to control the MBS front end, and allows for online analysis during the experiment. Figure 2.11 shows a schematic for tasks in the MARABOU system.

On the hardware side, a VME-CAMAC (Versa Module European - Computer Aided Measurement and Control) interface is used. The purpose of the CAMAC system is to allow a variety of different modular crate electronics used in the experiment to interface

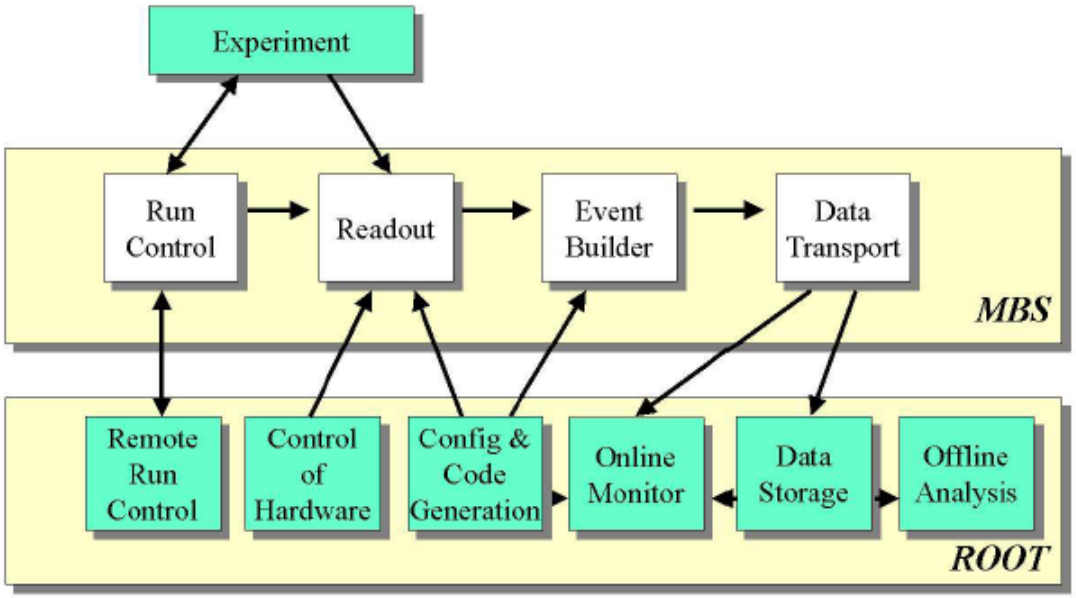

FIGURE 2.11: Marabou task schematic. Figure adopted from [38].

on a common back plane. This then connects to two computers; one which reads the data and writes to memory, the other processor takes data from the VSB port of the memory and sends the formatted events to the Linux host. Figure 2.12 shows a schematic of the hardware configuration as used in the experiment. A schematic of the hardware is shown in Figure 2.12.

2.2 ^{39}K(^{3}He,t)^{39}Ca Experiment at TUNL

This section will describe the ^{39}K(^{3}He,t)^{39}Ca experiment at TUNL. This experiment was carried out to follow up on the previous study and confirm the existence of the states discovered. The (^{3}He,t) reaction tends to populate states non-selectively in J^{π}, and it has not been measured in the energy region of interest, so undiscovered states in ^{39}Ca will hopefully be observed in this work.

2.2.1 TUNL Ion Source

While the purpose of the ion source - to generate negatively charged beam ions - is the same in both experiments, the methods and tools used are very different. The two major components used at TUNL are: 1) the duoplasmatron and extractor, and 2) the sodium

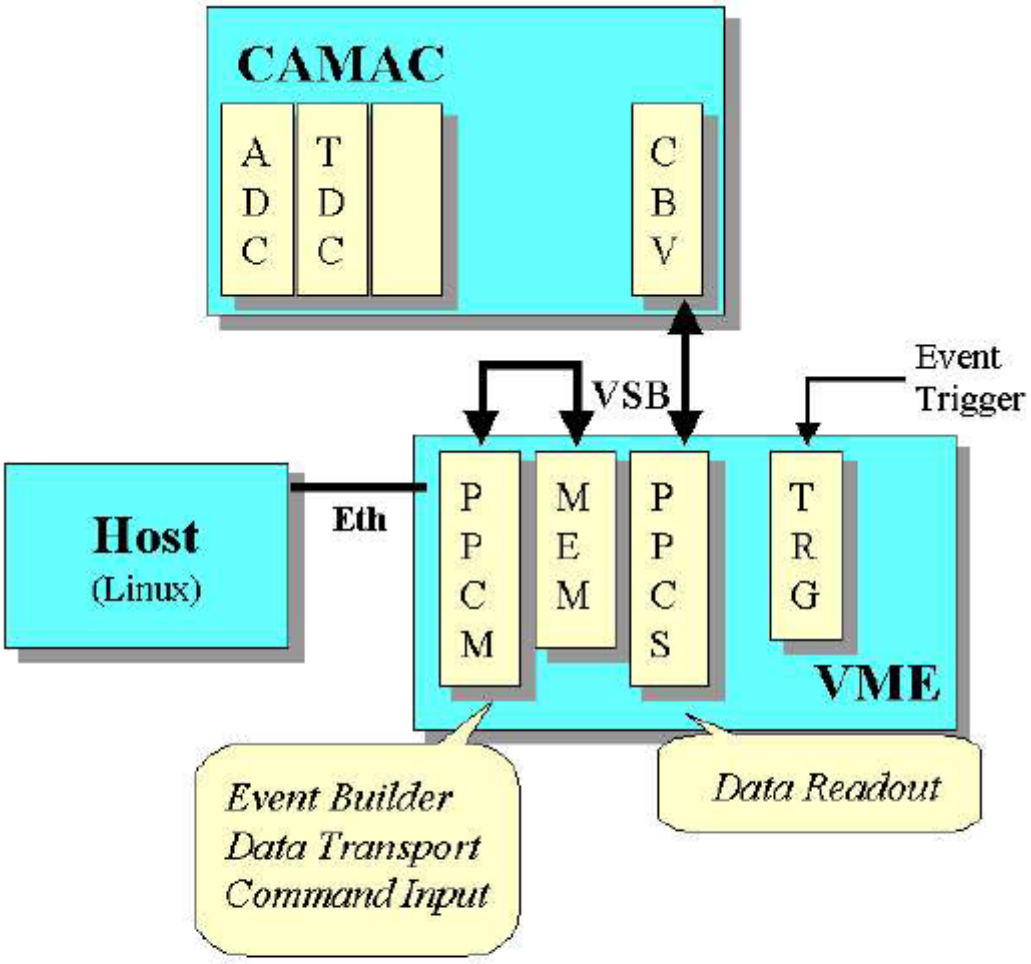

FIGURE 2.12: MARABOU hardware schematic. Figure adopted from [38].

vapor oven. These are analogous to the ECR ionizer and Cesium Vapour jet respectively that were used in the MLL experiment.

The working principle of the duoplasmatron will be discussed first; a figure of the instrument is shown in Figure 2.13. The purpose of this apparatus is to generate positively charged ions of ^{3}He which will then undergo two electron pickup in the sodium oven. To that end, the duoplasmatron creates two stages of discharge. The first stage creates a discharge of electrons via thermionic emission from a hot cathode filament (typically made of tungsten) set to a positive voltage in region A. The electrons are guided towards the helium gas inlet by a combination of a strong axial magnetic field, and a funnel shaped intermediate electrode placed between the hot filament cathode and grounded anode. The intermediate electrode is biased to a voltage that is about half of the filament cathode voltage. This helps constrict the discharge further along the axis from the entrance to exit aperture. The electrons then reach the gas inlet where it interacts with the helium gas and ionizes it, producing the second discharge. As the electrons from the first stage of discharge deposit the kinetic energy to the helium atoms, they slow down and migrate across the magnetic field lines. The result is that the plasma in this region has a positive potential and helps to push the positive helium ions out of the anode in region B. The intermediate electrode now acts as a cathode and positively charged helium ions are accelerated towards the grounded anode and enter the extraction region.

The duoplasmatron used in this experiment is described now. The cathode filament is heated resistively and is biased to a voltage between +30-70 V [40] relative to the anode electrode which is kept at ground. In addition to the components listed in Figure 2.13, a soft iron probe takes the place of the intermediate electrode, and is biased to a voltage of about half of the filaments. The probe is a pencil-shaped containment vessel and is surrounded by the source head magnet. The anode electrode is held at ground, and is composed of copper with a molybdenum insert. After the ionized gas passes through the anode, it in a steel plasma expansion cup and is extracted with an electric field created by an applied voltage of about -19 kV.

After the beam has formed, it enters the sodium vapor oven[41]. This instrument will facilitate charge-exchange and convert the positively charged helium ions into negatively charged ions for the tandem to accelerate. This is accomplished via a two electron pickup from the sodium vapour. The sodium oven is composed of four elements: heat shield, heating element, sodium oven and charge exchange canal [40]. The heat shield protects

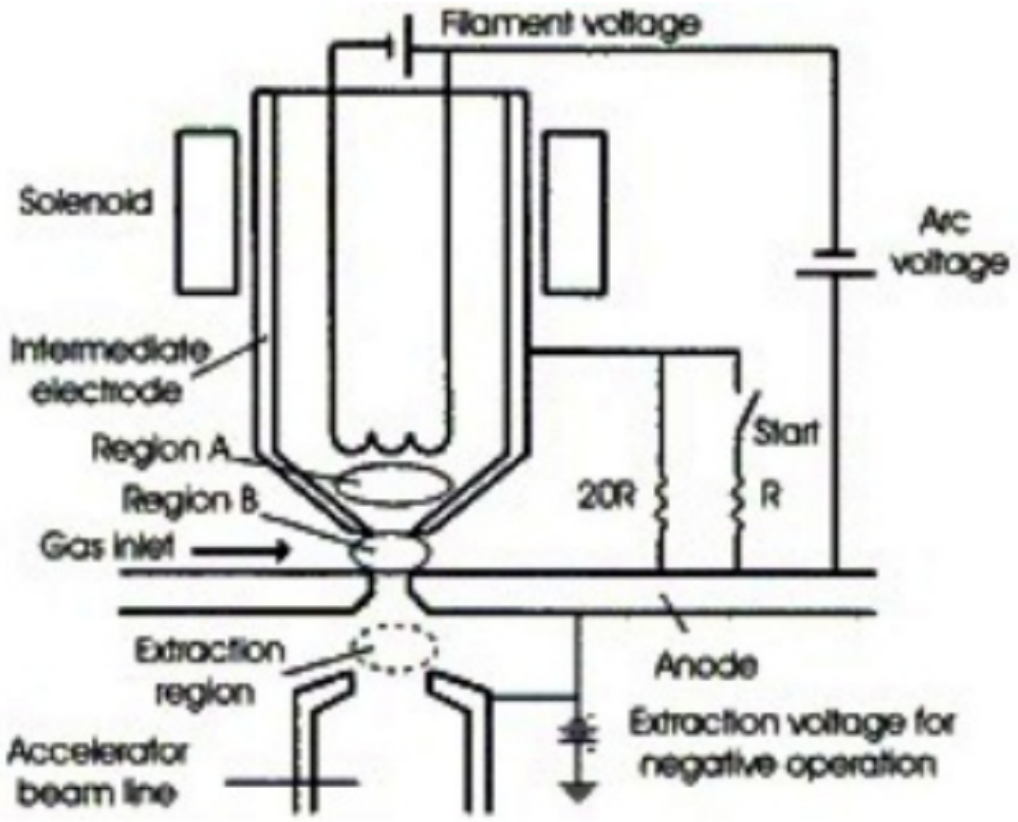

FIGURE 2.13: Duoplasmatron schematic. The cathode filament introduces thermionic electrons into region A. These are accelerated with the intermediate electrode which acts as an anode, and constrained by an axial magnetic field provided by the solenoid. The electrons interact with the incoming Helium atoms from the gas inlet, ionizing them. The now positively charged Helium ions are accelerated towards the anode plate, and the intermediate electrode acts as a cathode. They are then extracted.Figure adopted from [39]

the instruments exterior to the element from the intense heating. The sodium oven is surrounded by the heating element, which radiatively heats it with infrared radiation. There is a hole in the oven which leads to the charge-exchange canal, and this is where the ions can undergo double electron pickup.

2.2.2 10 MV FN Tandem Accelerator

The tandem uses two pelletron charging chains which are described in the subsection 2.1.3. Much of the operating principles are similar to that used in the MLL; however it does not have the liner or TOF system for energy stabilization. It instead is regulated by a corona needle assembly, which draws current from corona discharge. In "GVM" (Generating Volt Meter) setting, the control grid receives the signal from the corona discharge and adjusts based on the error signal which is the difference between the terminal voltage setpoint and signal from the voltmeter reading the actual terminal voltage. This was the typical mode used in this experiment.

2.2.3 Enge Split-pole Spectrograph

An Enge Split-pole spectrograph was employed for this experiment. The principle of this instrument is the same as that of the Q3D; by exploiting the Lorentz force, we can apply a magnetic field onto the moving charged reaction particles generated from the beam interacting with the target, which momentum analyzes the particles on a focal plane. However the difference between the Split-pole and the Q3D lies in the details and capabilities of each instrument.

The description "Split-pole" is because there are two separate dipole pieces surrounded by a single coil [42]. A schematic view of the spectrograph is found in Figure 2.14. The purpose of the split is to provide second-order double focusing over a larger range of energies. For vertical focusing, the goal is to achieve the highest collecting power in the instrument rather than achieving an exact image of the source. Low momentum particles are able to converge easily after being focused in the entrance of the first dipole. High-momentum particles however are not immediately focused by the first dipole. The split is designed in a way such that high-momentum particles experience stronger focusing forces moving across the split, where it interacts with the surrounding coil, which allows for a wider total range on the momentum.

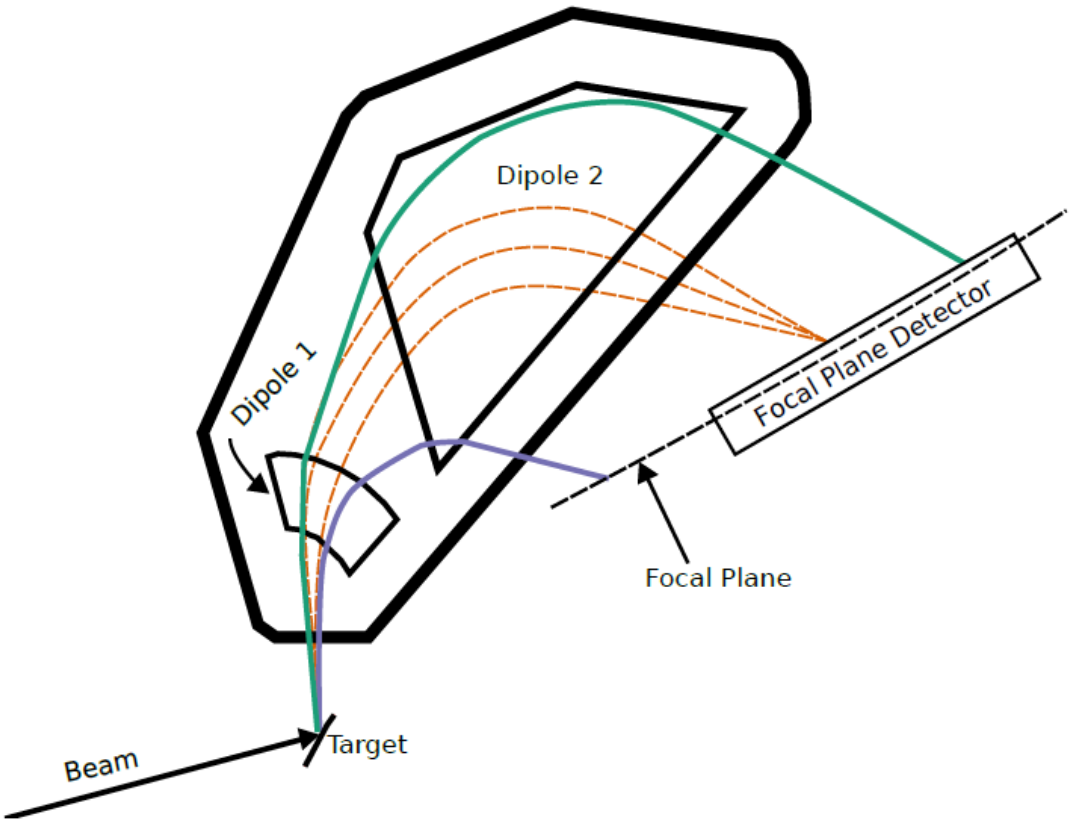

FIGURE 2.14: Schematic of the TUNL split-pole spectrograph. Two dipoles analyze the momentum of the reaction products. Figure adopted from [43].

During this experiment the dipoles provide a vertical magnetic field of strength 11.5 - 11.6 kG. This magnetic field strength was chosen to maximize the coverage of astrophysically interesting energy levels in ^{39}Ca. The solid angle of aperture for maximum acceptance for the spectrograph is 6.1 msr; however in order to maximize the energy resolution of the device, the acceptance solid angle was kept at 1-2 msr (depending on if higher statistics were required).

An advantage of this instrument is the large momentum coverage, and thus the range of energies able to be detected at a given magnetic field strength. The resolution of each instrument can also be comparable. We had attempted to measure the ^{39}K(^{3}He,t)^{39}Ca reaction at MLL in 2019, however a tandem chain had malfunctioned, causing an early end to our experiment, and only the 15° spectrograph angle could be measured. These data are shown in Figure 2.15, and uses both the same KI target and the same energy of ^{3}He beam. This comparison of resolution also depends on the focal plane detector, and sources of energy loss in the detector suite; however it is meant to illustrate that the split-pole energy resolution is indeed comparable to the Q3D.

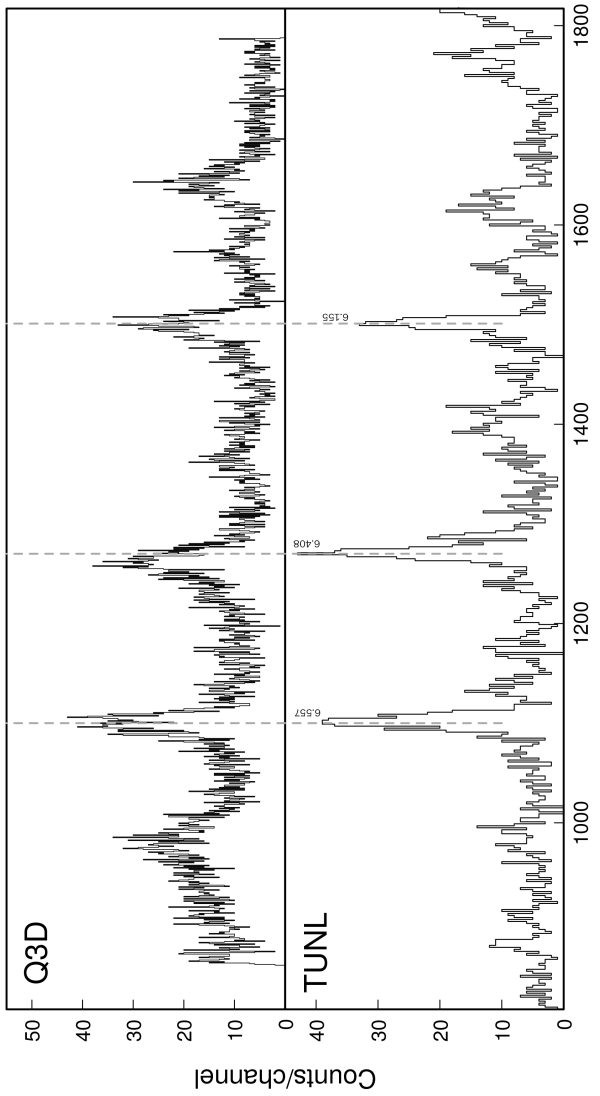

FIGURE 2.15: Comparing spectrum from Q3D data and Split-pole data. Spectra are both measuring tritons from the ^{39}K(^{3}He,t)^{39}Ca reaction at 15° lab angle.

2.2.4 Target Evaporation Setup

This section will discuss the target evaporation process used to fabricate the production targets used in this experiment composed of potassium iodide (KI). Metallic potassium oxidizes violently, and so a compound is required for stability. Potassium fluoride (KF) was considered, since a KF target of similar thickness to a KI target would have more potassium in it due to the mass ratio. Given a target thickness of 100 μg/cm^2, a KI target would have 23.5 μg/cm^2 of potassium, while a KF target would have 67.3 μg/cm^2 of potassium.

This was ultimately not chosen as the target since the fluorine content introduced a much larger contaminant background to the triton spectra compared to the iodine content. Thin natural carbon foils were obtained from Arizona Carbon Foil (ACF) metals with thickness specifications of approximately 20 $\pm$ 2 μg/cm^2. Foils were floated off their glass slide into distilled water. From the water, they were picked up using the TUNL target frames. As they dried off in atmosphere, care was taken to make sure water droplets did not collect and rupture the foil.

After drying, they were taken to the evaporator and placed on the substrate holder. While there are 16 slots, due to the geometry of the evaporation, the middle 8 slots are optimal for keeping a consistent thickness among all the targets. This is because the flux of the evaporating particles has a 1/r^2 dependence, so by arranging the foils only on the middle we can mitigate that effect. KI in powder form is loaded into a tantalum boat which is clamped in place by copper electrodes on either side. A sputter blocker is put above the boat until the evaporation is ready to begin.

A quartz crystal thickness monitor is also put into one of the substrate holder's slots. A quartz crystal is subject to the piezoelectric effect; that is the relationship between mechanical deformation and voltage applied [44]. If an alternating current is applied to the crystal, it will induce well quantified oscillations in the quartz crystal. Since the frequency of oscillation depends partially on the thickness of the crystal, a change in oscillation frequency can be used to deduce the thickness of the layer built up on the crystal. This allows us to measure thickness down to the Angstrom range.

A glass bell jar with a rubber o-ring is used to house the setup. To pump out the air from the enclosure, a roughing pump as well as a diffusion pump are used. A pressure of

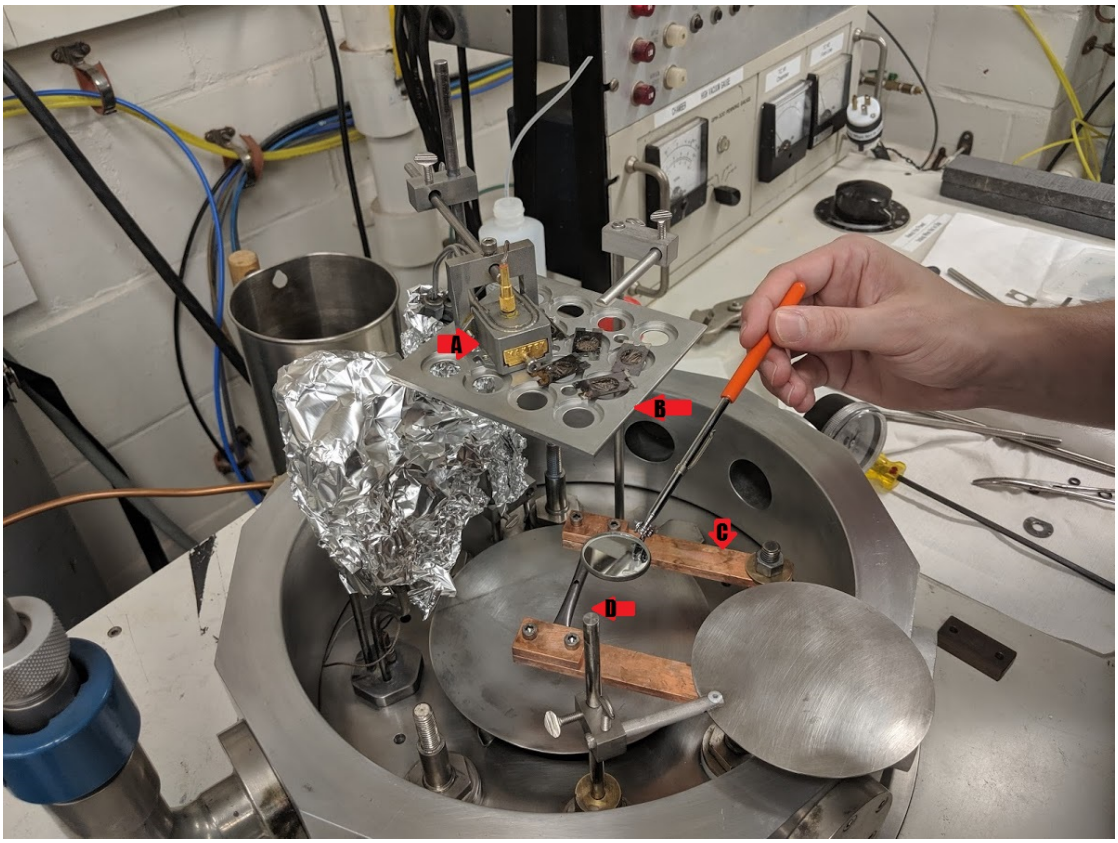

FIGURE 2.16: Target Evaporation Setup. A) Quartz crystal thickness monitor, B) Substrate holder, C) Copper electrode, D) Tantalum boat containing KI. The sputter blocker can be rotated into place from outside the bell jar. A glass bell jar and rubber o-ring are placed atop the setup to contain the vacuum.

8×10^{-5} Torr is needed to have a clean evaporation, and can take several hours to slowly evacuate, using the combination of the two pumps.

Once the chamber has been evacuated, the KI is ready to be evaporated. This is done by passing a current of approximately 62 A through the copper electrode and tantalum boat. The resistivity of tantalum is high such that resistive heating is induced and the material inside vaporizes. Once the necessary temperature is reached, the sputter cover is removed, and the thickness is closely monitored, adjusting the current through the boat to control the flux. A thickness of 320.5 nm was deposited onto the carbon backing, corresponding to 100 μg/cm^2.

A target of nat. Aluminium (100% ^{27}Al) was used as a calibration target for this experiment. This target was found in a closet of previously used targets and unfortunately the specifications of the Aluminium thickness and carbon backing thickness is not known. Work is currently being done to deduce the thickness of the target. This target was chosen as a calibration target because Specplot simulations show that well separated triton peaks of known energies appear in our energy range of interest.

2.2.5 TUNL detector suite

Much of the same principles used in the MLL experiment are employed here, such as the use of wire proportional counters and position sensitive cathode detectors. A schematic of the detector suite is found in Figure 2.17. The focal plane detector consists of two position-sensitive avalanche counters, a gas proportionality counter (energy deposition labelled ΔE), and a residual energy scintillator (energy deposition labelled E). These are contained within a chassis that is filled with isobutane held at 200 Torr, and separated from the vacuum of the spectrograph by a 12.7 μm Kapton entrance window [43].

After the particles pass through the entrance window, they encounters the first position-sensitive avalanche detector. The detector consists of two cathode foils made of aluminized mylar, and five high voltage anode wires. The cathode foil closest to the entrance of the detector has been separated into cathode strips via an electroetching technique [45]. It is essential that the cathode strips are of the same width and are well electrically isolated from each other. The electroetching technique makes use of an electric discharge to remove the aluminium coating from the mylar foil to etch borders between the cathode strips. To etch the lines, the aluminized mylar foil is first stretched

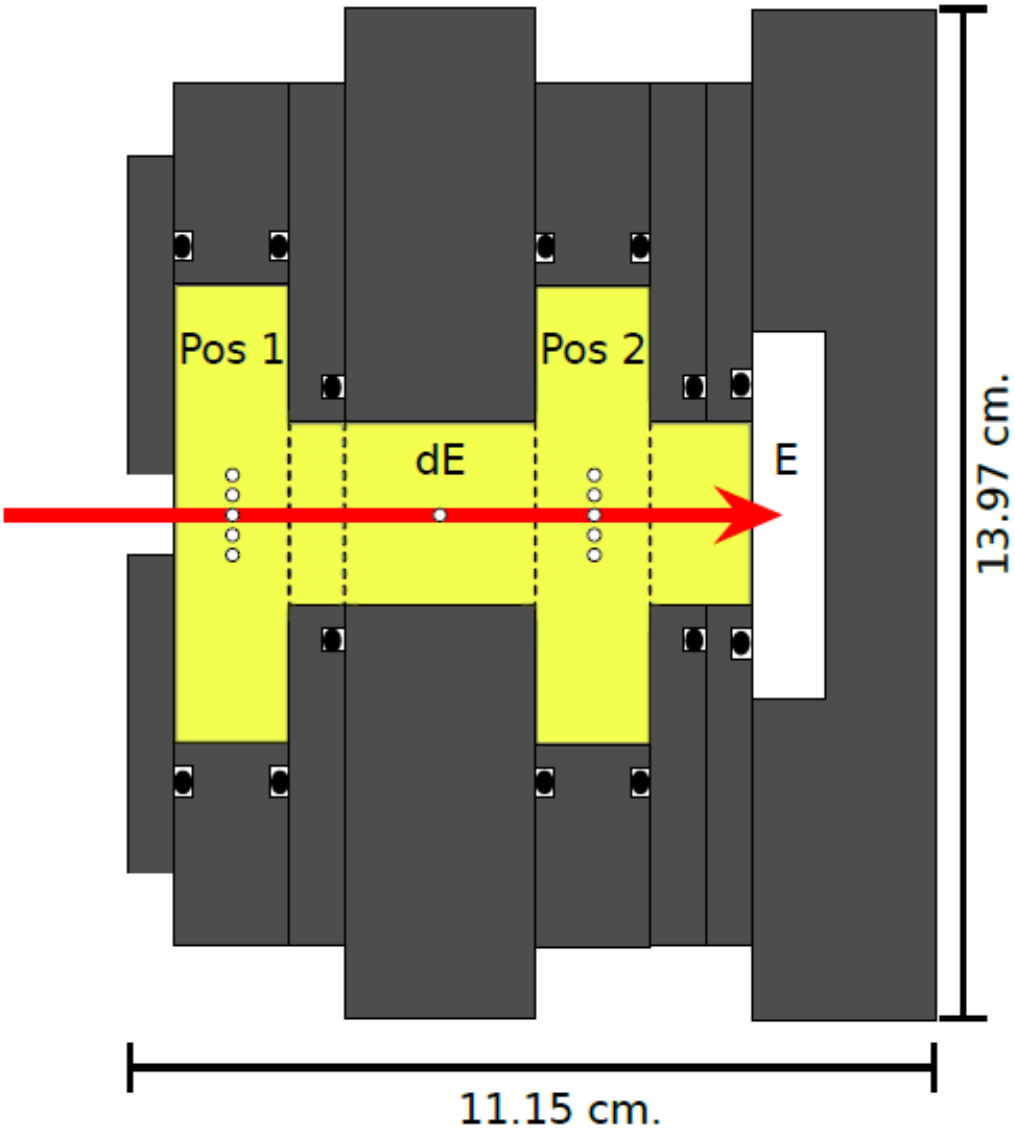

FIGURE 2.17: Detector suite used at TUNL. The entire setup is filled with pressurized isobutane gas. Beamline is labelled in red. Pos 1 represents the first cathode strip detector, followed by dE, a wire proportional counter. The beam then passes through Pos 2 (a second cathode strip detector), and finally E, the scintillator which absorbs the remainder of the beam particle's energy. Figure adopted from [43].

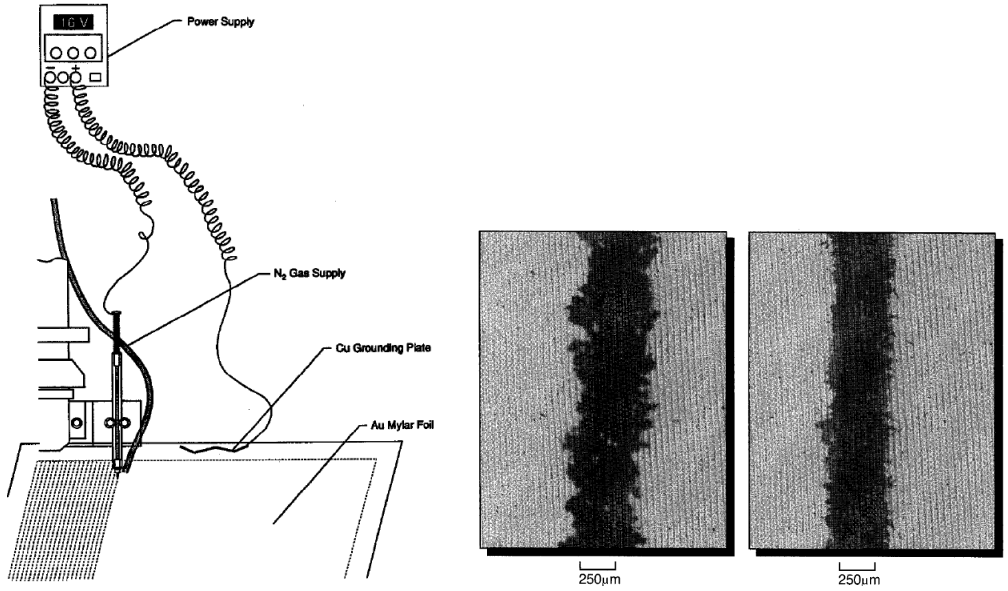

FIGURE 2.18: Electroetch system: a) On left: Electroetch setup, where a stylus is attached to a motor which is programmed to move in regularly spaced lines. The stylus is also attached to a voltage source and applies electrical discharge to produce the lines electrically isolating lines. b) on right: A comparison of the electroetch line's definition. The first line is made using a positive voltage, whereas the second is made from using a negative voltage. A cleaner line is seen using a negative voltage. Figure adopted from [45].

out on a frame to eliminate shifts in cathode positions that would have been introduced in stretching an etched foil. A tungsten tipped stylus is attached to a copper assembly as pictured in Figure 2.18a. The stylus is held at a voltage of -15 V, since interestingly, the negative voltage gives a better edge definition when etching as seen in Figure 2.18b. Each strip is 2.54 mm wide with each etched line being 0.03-mm wide. The mylar strips themselves were 0.3 μm thick single-sided aluminized mylar. As a particle passes through the position detector, the same ionization and electron avalanche as described earlier occurs.

The induced charge on the cathode strips are then transferred to a set of delay line chips. The principle of operation is as follows: The charge is collected on the cathode strip on a point on the length of the focal plane. The charge is then sent out in both directions of the length of the focal plane on a set of "taps"[43]. These taps induce a 5 ns delay, and by looking at the arrival time of each signal, the location of the induced charge can be deduced. The delay line consists of 20 delay chips with 10 taps per chip.

The total delay across the line is 1 μs. The uncertainty in the delay per tap is 1.5 ns, which is quite high. This can result in non-linearity in the delay to position conversion [46].

The gas proportionality counter consists of a 12.7 μm diameter anode wire held at 1000 V, and two grounded cathode plane foils. The front cathode plane is simply the other side of the first position detector. These function in the same way as the wire proportional counter as described in the MLL detector suite section subsection 2.1.6.

A scintillator is located at the end of the detector to obtain the residual energy deposited. The scintillator paddle used here is a Saint-Gobain BC-404 organic plastic scintillator [43]. The operating principle of this device is the same as the scintillator used in the MLL detector suite, see subsection 2.1.6 . To maximize the amount of light collected along the scintillator, a wrapping of Tyvek and Aluminum foil has been employed. While Tyvek wrapping has been demonstrated to produce a higher light output compared to aluminum, the former is not able to withstand the pressurised environment of the detector, so aluminum foil was chosen to create a sealing surface.

Conventionally a light guide is used to transfer the light produced from the scintillator; however, light guides can add significant weight and length to the detector. The design choice in this detector is instead to employ optical fibers to gather the light to a Photomultiplier tube. The fibers are 1-mm diameter Bicron BCF-91A which also shifts the wavelength of the scintillated light (380-495 nm) from the BC-404 to the green spectrum (490-570 nm). Eight 1-mm deep grooves spaced 5 mm apart were machined onto the scintillator and the fibers were placed and secured into the groove using BC-600 optical cement. The spacing used had been shown to maximize the light collection on the scintillator.

The dynode signal from the PMT provides precise timing information, and acts as a trigger to generate an event count. A count from the E detector triggers a gate for the DAQ to begin taking data for a 10 μs interval.

GEANT4 [47] simulations were done by Ref. [43] to estimate the energy resolution with the Full Width at Half Maximum (FWHM). As a charged particle travels through a detector it scatters on elements that are on the trajectory of the particle. This ultimately degrades the detector resolution, and increases the FWHM. This is shown in Figure 2.20 The elements that could cause scattering include: the Kapton window, curved to simulate

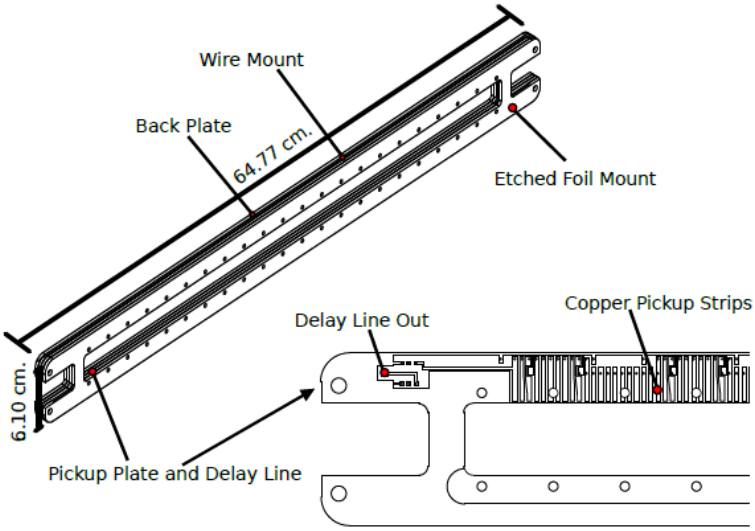

FIGURE 2.19: a) Front of the cathode strip detector as a result of the electroetch process. b) Figure adopted from [43]. Schematic of delay chips used to deliver position information from the cathode strip detector.

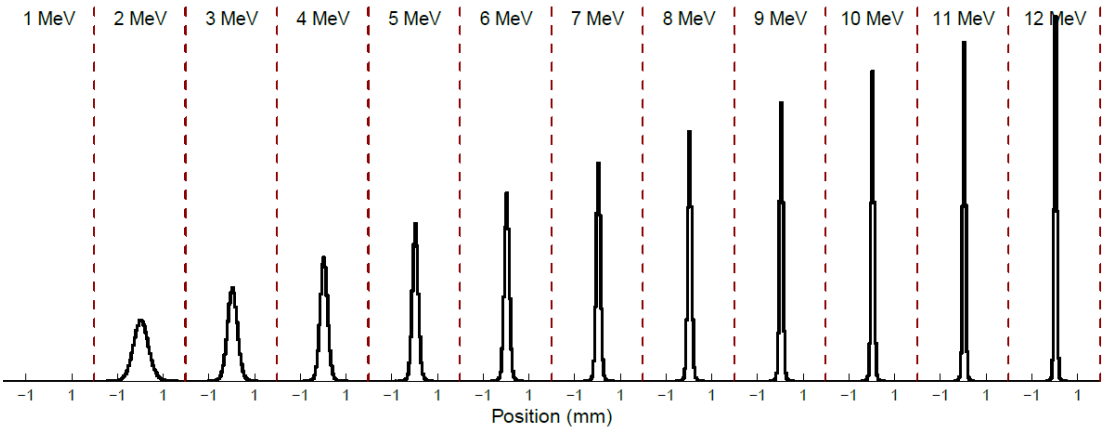

FIGURE 2.20: GEANT 4 position simulations from Ref. [43] for a range of proton incident energies. Each histogram is a simulated position spectrum with a focal plane at 0 mm for a range of energies 1-12 MeV. Of note is the lack of spectrum for the 1 MeV proton. Peak broadening occurs due to scattering from detector elements, such as the Kapton window, Mylar foil and isobutane gas. The scattering is exacerbated at lower energies as seen in the larger FWHM of the peak. Figure adopted from [43]

the bending from the pressure differential during operation, the isobutane gas, and all cathode foils. A test simulation was used to test which scattering element would have the largest impact on the FWHM. In this simulation, a beam of 7-MeV α particles impinged the front face of the detector at an angle of 43.5°(9.5°). The simulation showed that when all elements were in place, a FWHM resolution of 0.48(2) mm was seen. To test the contribution of each element, each individual element was removed to see the effect on the FWHM. Removing Mylar foils and isobutane gas did not affect the FWHM within statistical fluctuations; however when the Kapton foil was removed the FWHM became 0.06(2) mm. The Kapton window is therefore responsible for limiting the detector resolution, however, there must be an interface to separate the vacuum of the spectrometer and the pressurized environment of the detector, so the Kapton window cannot be removed.

The kinematic broadening effect is introduced when there is a dependence between the focal plane image and the entrance angle. This can be solved by displacing the detector in the direction of the beam.

Chapter 3

Data analysis and Results

3.1 Data Analysis

The following section will discuss the data analysis method used in each experiment. The major sections are: particle identification, peak fitting, and the calibration process to determine the energies.

3.1.1 Particle Identification

After coming out of the spectrograph, many different light reaction products will be present. These are typically α particles, tritons, deuterons or protons. Since we only want to see the events that produce tritons, we need a way to separate them from the other light reaction products. This section will discuss the Particle Identification (PID) technique used in the experiment. PID is carried out using the energy deposited in the wire proportional counter ($\Delta E1$), multiwire proportional counter (ΔE), and the plastic scintillator (E). As a light charged particle produced from the nuclear reaction passes through the isobutane gas it interacts with the gas primarily through Coulomb forces with the electrons of the gas. When the particle passes, it will interact simultaneously with several of these electrons, imparting an impulse to each of the electrons. This can result in excitation or ionization. The latter is what allows the detection of the particle in the two wire proportional counters. When the gas is ionized in this way, it comes at the expense of energy in the charged particle. The amount of energy that is deposited into the gas (and thus the magnitude of ionization events) is then proportional to the

stopping power of the particle through the gas. The linear stopping power is given by [36]:

$$S = -\frac{dE}{dx} \tag{3.1}$$

As the speed of the charged particle decreases, the stopping power, S, increases. The formula that describes this is known as the Bethe formula[48]:

$$\frac{dE}{dx} = \frac{4\pi e^4 Z^2}{m_0 v^2} NB \tag{3.2}$$

where

$$B = z\left[ln\frac{2m_0v^2}{I} - ln\left(1 - \frac{v^2}{c^2}\right) - \frac{v^2}{c^2}\right] \tag{3.3}$$

and Ze is the charge of the particle, m_0 is the mass of the electron, v is the velocity of the charged particle, N is the number density of the absorber atoms, z is the atomic number of the absorber atoms, and c is the speed of light. In non-relativistic conditions, the variable B varies slowly with v, so dE/dx varies as $1/v^2$. This makes sense since a charged particle with lower velocity (and hence kinetic energy) has more time to impart the impulse and interact with the electric field of the electrons. Figure 3.1 shows the hyperbolic relationship between dE/dx vs E.

This relationship can be used to distinguish individual nuclides in the cocktail of light reaction products from each other. Since the properties of the absorber atoms will remain the same, we can look at the variables unique to the charged particle:

$$\frac{dE}{dx} \propto \frac{Z^2}{v^2} \tag{3.4}$$

If we substitute the kinetic energy of the moving charged particle, $E = \frac{1}{2}Mv^2$, then this proportionality becomes:

$$\frac{dE}{dx} \propto MZ^2\frac{1}{E} \tag{3.5}$$

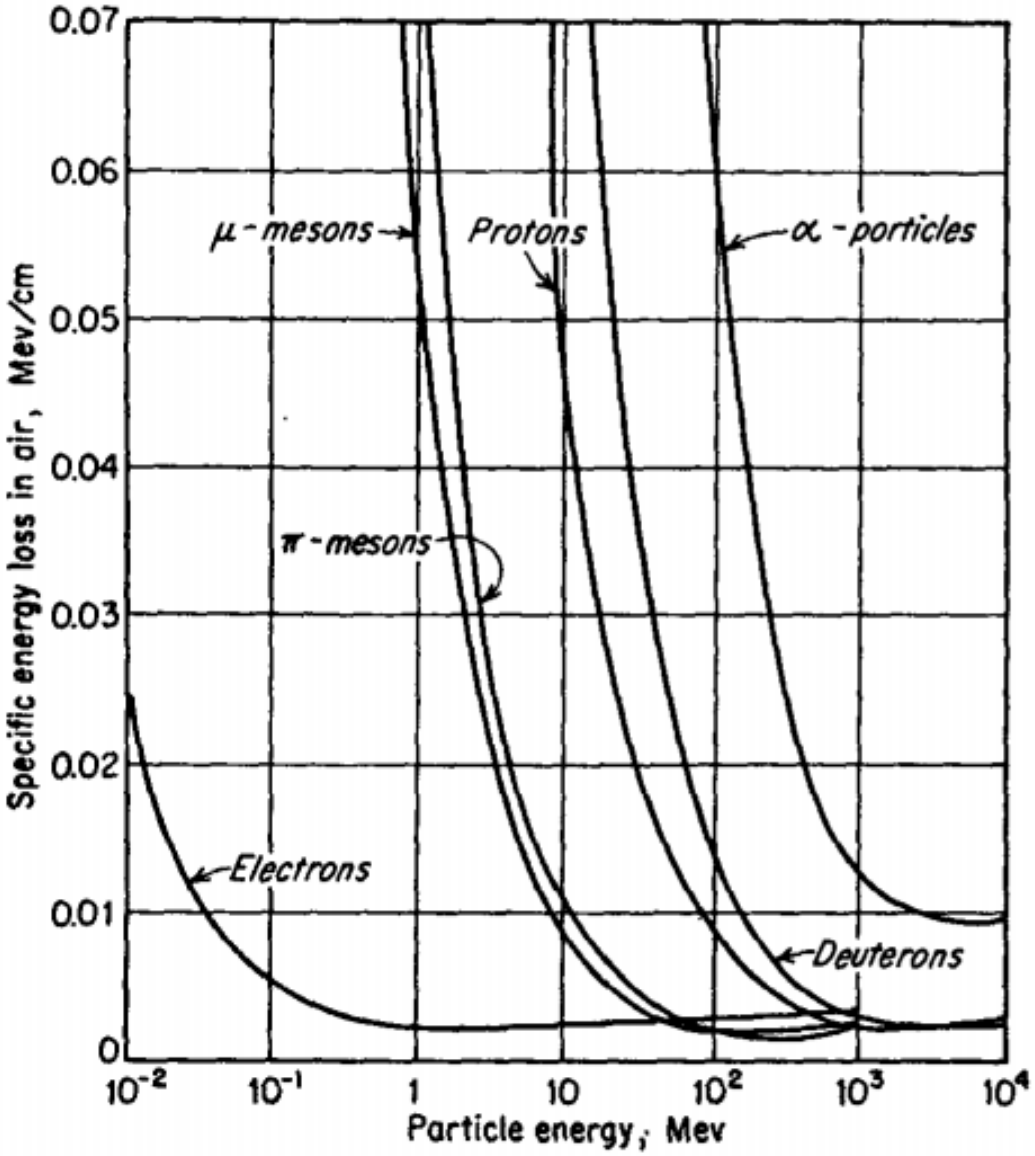

FIGURE 3.1: Energy loss curve taken from Ref. [35]. Variation of energy loss in air versus the kinetic energy of the charged particle.

Thus the energy loss from the moving charged particle into ionization of isobutane gas can be characterized by the mass times the charge squared. This is a product that is unique to each species of particle in the cocktail of light reaction products.

A particle that deposits more energy in the wire proportional counter will cause more electron ionization events, thus creating more ion pairs. This in turn will induce a larger current in the wire proportional counter, which will allow us to differentiate between each species of particle. If energy losses from the wire proportional counter and scintillator are plotted against each other (ΔE vs E), then each species of particle forms a locus of points as seen in Figure 3.2.

Tritons of interest can be selected with a "gate" in analysis software, which will allow only particles that have a unique energy profile to be analyzed. This particular gate is called the "proton" gate due to its resemblance to a canonically spherical proton. It should be noted that the shape of these loci are due to the momentum analysis of the Q3D. Since the Q3D only allows particles in a certain range of momenta to pass through, Thus, since the reaction products are not in a continuous energy range, the result is that the particle groups appear as circular blobs. An additional gate can also be drawn using the energy deposited in each of the the wire proportional counters ΔE vs. $\Delta E1$. Using the same principles as previously, we can draw a "banane" gate due to its resemblance to a (German) banana. This is seen in Figure 3.3. A plot ΔE vs E was used to select tritons from the TUNL ^{39}K(^{3}He,t) reaction. This plot is shown in Figure 3.4 with tritons highlighted in red.

It should be noted that these tritons are from all nuclear reactions in the target in addition to the calcium. This includes the isotopically pure ^{12}C backing, fluorine, and any elements that could have collected via oxidation. This will be apparent in the position spectrum that we obtain in the coming sections.

3.1.2 Peak analysis

The increased cross section resulting from forming a resonant state manifests as local peaks of increased count on specific positions in the triton position histogram. Theoretically, these peaks should take the form of the Breit-Wigner distribution, but due to contributions from random error, these distributions more closely resemble Gaussian distributions.

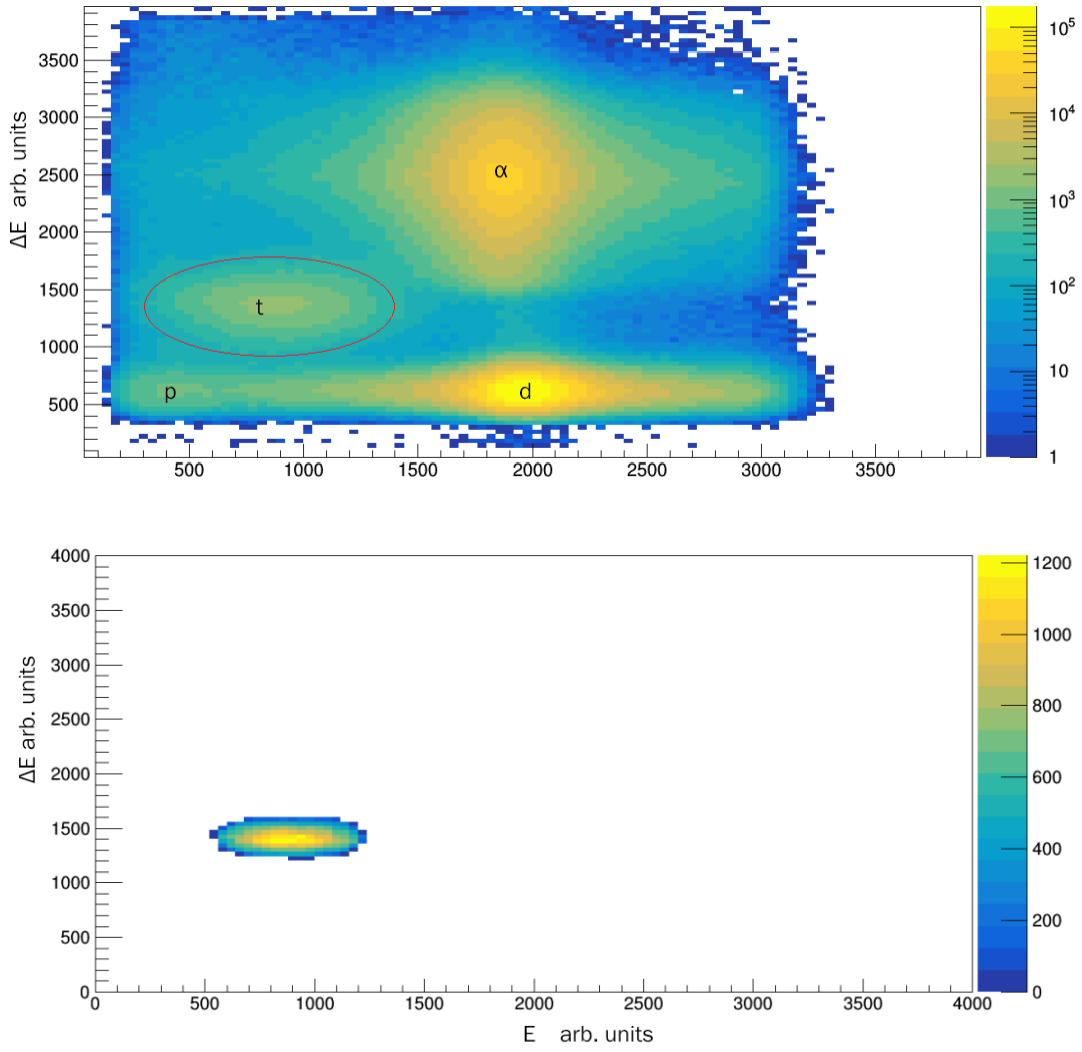

FIGURE 3.2: PID plot of MLL data at 20° spectrograph angle, units of axes arbitrary. Top: The various species of light reaction products pass through the wire proportional counter and end in the scintillator, depositing energy according to Equation 3.5. When plotting the energy loss through these detectors (ΔE and E for wire proportional and scintillator respectively) each unique particle species forms a locus of points. The particle group to the circled in red are tritons. Bottom: A gate is set on the tritons so that only events that fall within the red circle in the above figure are used in the position spectrum.

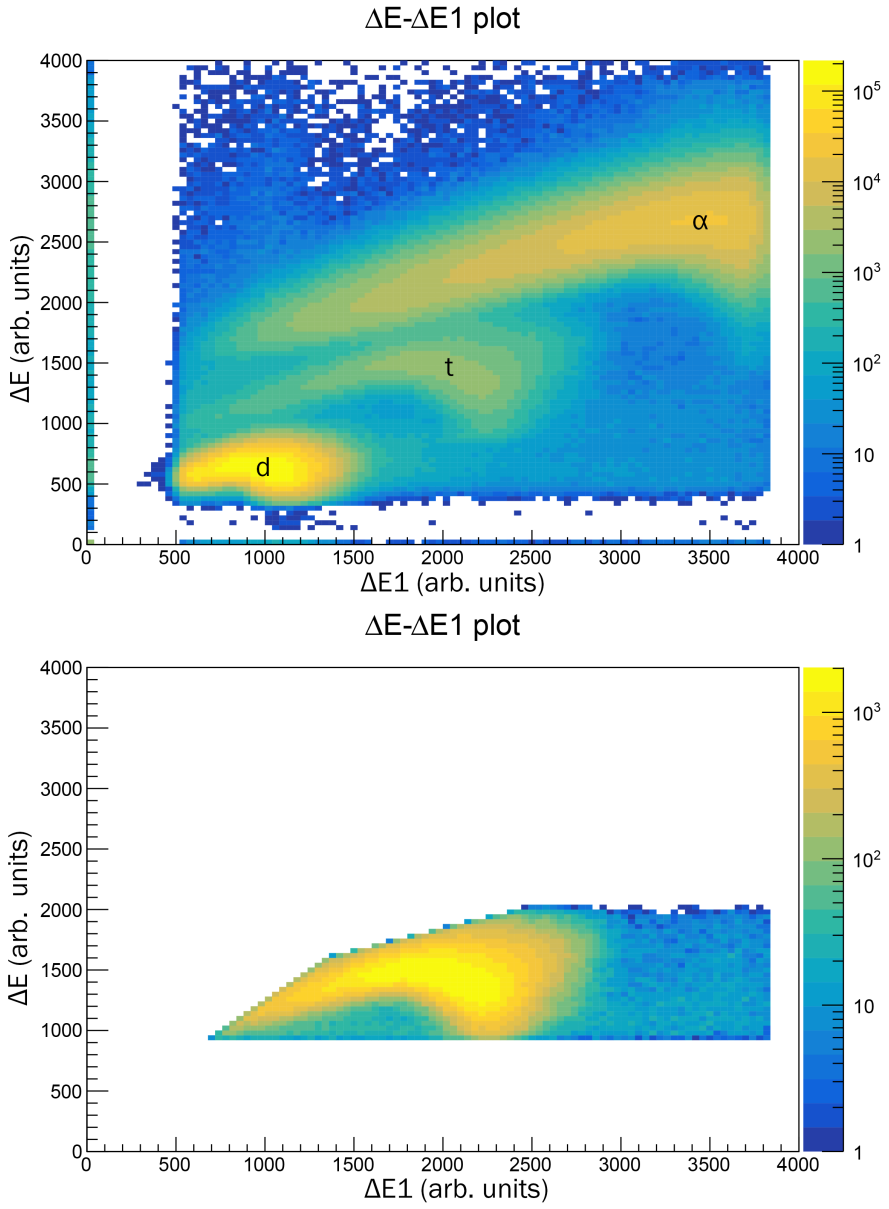

FIGURE 3.3: PID plot of MLL data at 20° spectrograph angle, units of axes are arbitrary. Top: Various species of light reaction products also pass through a multiwire proportional counter giving an signal labelled $\Delta E1$. By plotting the energy loss from the wire proportional counter (ΔE) against the the multiwire proportional counter ($\Delta E1$), each particle species forms a locus of points. Bottom: The particle group of tritons can be gated on. Only events with those energies are used in position spectrum.

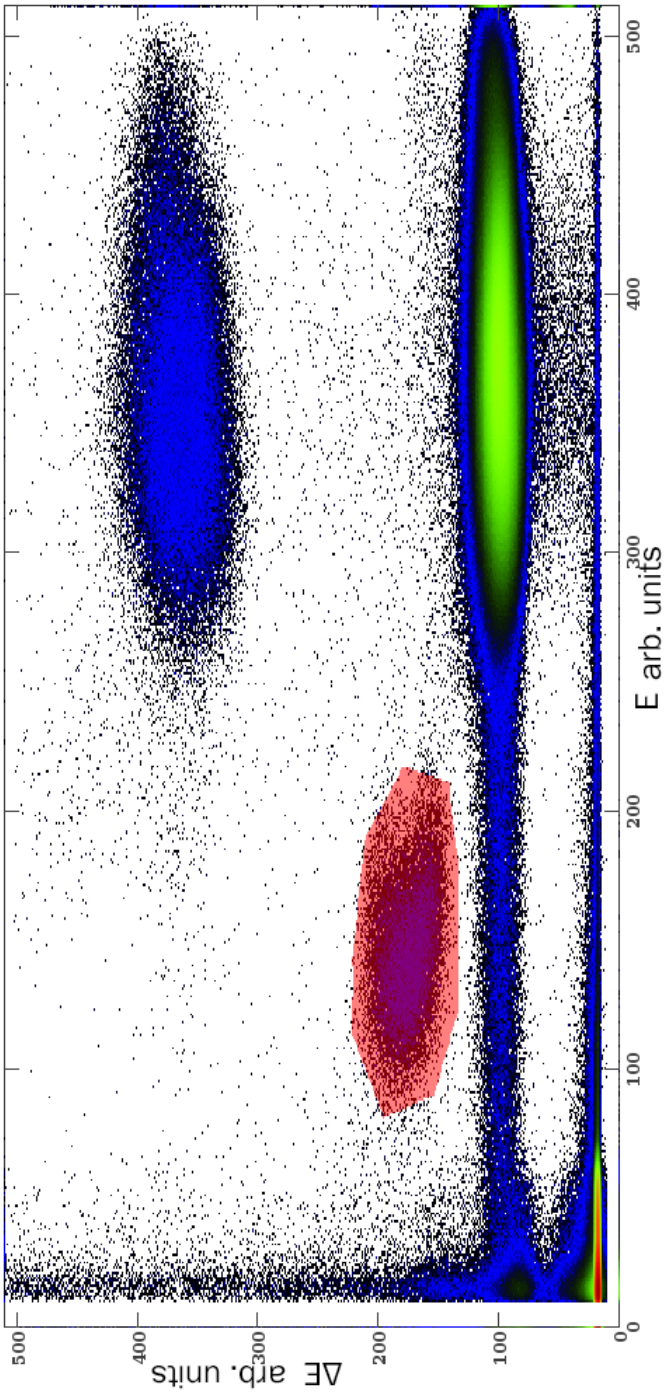

FIGURE 3.4: TUNL PID, units of axes are arbitrary: Energy loss through the wire proportional counter (ΔE) is plotted against energy loss at scintillator (E) Tritons are highlighted in red, and will be used in the position spectrum.

Further, in the peaks from the MLL data, there is an asymmetry with the Gaussian distribution, namely that there is straggling at the lower triton energies within a given peak. This asymmetry can be seen in Figure 3.5. Recalling that charged particles of higher energy will lose less energy when moving through a medium, higher energy particles that move within the CaF_2 target will be subject to less energy loss than their lower energy counterparts within a single peak. This results in a low energy tail. The function that fit the peaks well is a Gaussian function modified by an exponential. This is given by:

$$f(x) = Ce^{-\frac{1}{2}\left(\frac{x-\mu}{\sigma}\right)^2} \times \begin{cases} e^{\lambda(x-\mu)}, & \text{for } x < \mu \\ 1, & \text{for } x \geq \mu \end{cases} \tag{3.6}$$

where the expression to the left of the curly brace is the typical Gaussian distribution, with channel number x, mean μ, width σ, and intensity C. The latter three variables are fitted to the data in order to minimize χ^2. On the right of the curly braces is the exponential modification that is applied asymmetrically about the mean, with a variable λ which is fitted to the data. Figure 3.5 shows a comparison of this asymmetric Gaussian fit vs. a conventional Gaussian fit for a triton peak in the ^{32}S target. Most importantly, it shifts the centroid to a more accurate position in the peak.

Lastly, in the MLL data there was a large background that could not be satisfactorily described with a global polynomial function. Thus, a linear background was applied under the peak of interest when fitting, sampling only the region of interest near the peak.

To fit the data for the MLL experiment we used a conventional χ^2 minimization procedure. These seek to minimize the χ^2 test of goodness of fit defined by:

$$\chi^2 = \sum_{i=1}^{n_{bins}} \left(\frac{y_i - f(x; a_0 ... a_k)}{\sigma_i} \right)^2 \tag{3.7}$$

where the a_k are the adjustable parameters for the fit function $f(x; a_0, , , a_k)$, y_i is the measured value for the i^{th} bin, and σ_i is the uncertainty of the measured value for the i^{th} bin.

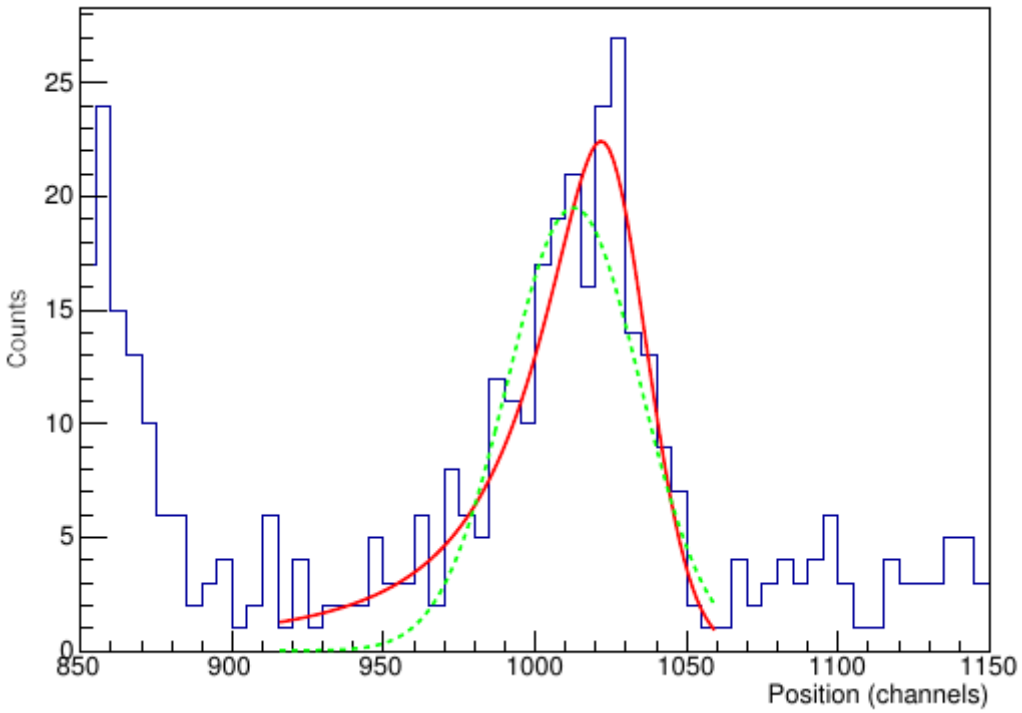

FIGURE 3.5: Triton spectrum of the ^{32}S(d,t)^{31}S reaction from MLL experiment. Fit function is an asymmetric Gaussian fit in red vs. symmetric Gaussian fit in dotted green. The former is a more accurate fit that accounts for the low energy triton tail.

A ROOT [49] macro was created in order to fit n peaks that are overlapping. The same χ^2 condition was applied for the fitting; however, a sum of n exponentially modified Gaussian functions was used as the descriptive function instead.

For the TUNL data, a different approach was taken. The peaks were fitted instead with the quadratic approximation, a Markov Chain Monte Carlo (MCMC) algorithm, using the R programming language developed by Refs. [43, 50]. Initial guesses were provided by the user on the parameters of the Gaussian function (mean, intensity, background, and area of interest), and a normal distribution is created for each variable with mean equal to the guess, and width of ten channels. The normal distributions are then sampled in order to create n Gaussians. These are then used to create a probability distribution function (PDF) of each variable, each which converges on a target distribution. These target distributions are well approximated as normal distributions, and each centroid yields the value of each respective variable. An example of the final fit is shown in Figure 3.6

3.1.3 Energy calibration

We have identified the positions of the centroids for the Gaussians in the triton position spectra produced by targets - calibration and production - in the experiments performed. Since the positions of increased cross sections represent reactions occurring at the resonance energy (via momentum sorting in the spectrograph), the energy related to that position needs to be known. The peaks of the calibration spectrum are what will be used to convert the position axis of the spectrum into a value of triton energy. Candidates for calibration targets were chosen based on whether the triton producing reaction could produce well separated and previously precisely measured states in the residual nucleus. The properties of the calibration targets used in each experiment are explained in previous sections (subsection 2.1.4 and subsection 2.2.4).

The calibration was done using a Markov Chain Monte Carlo (MCMC) algorithm [51]:

- First, we take one of the observed centroids obtained from the fitted Gaussians in a given triton spectrum and create a normal distribution $\mathcal{N}(x_{obs}, \sigma)$ where μ is the mean of the normal distribution and σ is the standard deviation. We repeat this for all data points used in the calibration.

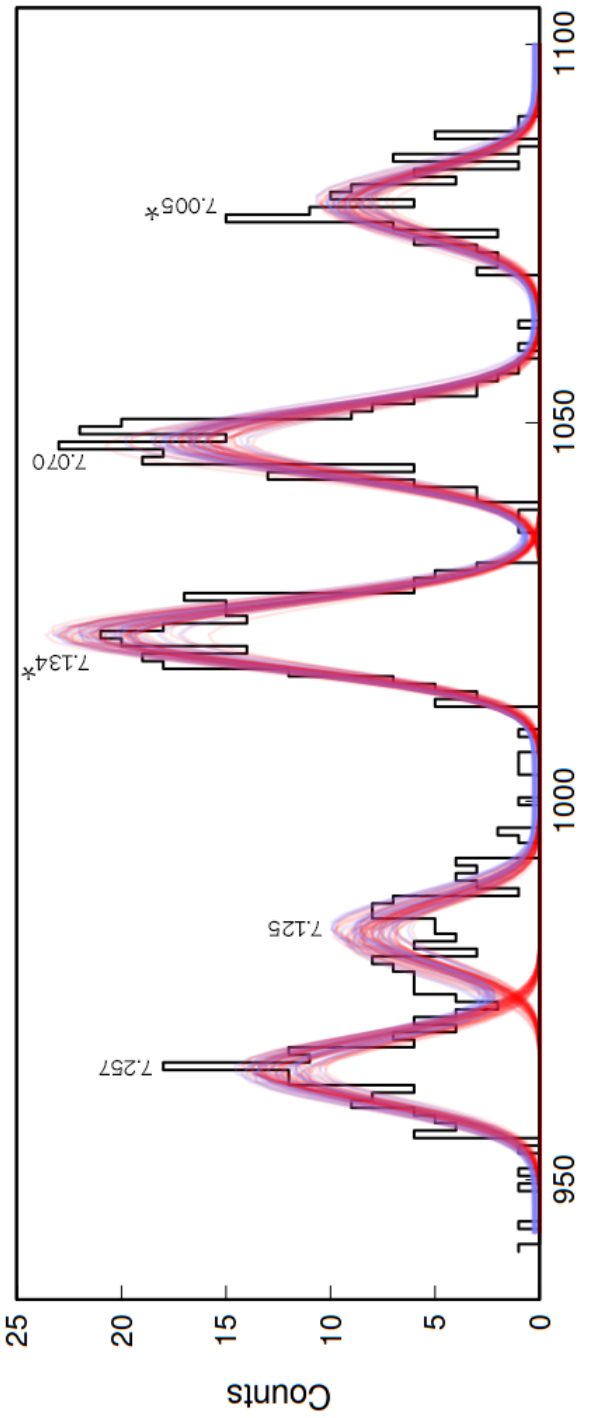

FIGURE 3.6: TUNL triton position spectrum from the ^{27}Al(^{3}He,t)^{27}Si reaction used to calibrate data at the 15 degrees spectrograph angle. Red lines are Gaussian fits, blue lines are fits using a Gaussian summed with linear background. Energies assigned to each peak are displayed in MeV above the peaks. Numbers in red are energy values that were used in the calibration.

- Next, we define a polynomial of degree N that relates magnetic rigidity to the observed centroids, $\rho = \theta_0 x_i^0 + \theta_1 x_i^1 ... \theta_N x_i^N$, where x_i is the observed centroid, and θ_N are coefficients to be fitted. This is defined as the kinematic equation; for this work, a 3rd degree polynomial was used.
- Random samples from the normal distributions produced in the first step are then used to solve the kinematic equation, This produces one set of values for the coefficients. This is repeated 50000 times and the values of the coefficients are plotted in a histogram, yielding a probability distribution function for each coefficient. The form of these PDFs are well described by normal distributions as well, and the mean values determined give the value of each respective coefficient.

From this process, the magnetic rigidity, and thus the energy of the tritons from that peak can be determined. Runs using the calibration target and background target were taken before and after a series of runs with the production target. This was done to monitor the energy drift of the beam by observing if the positions of peaks shifted before and after the run.

From the TUNL experiment, the triton position spectra from the ^{27}Al(^{3}He,t)^{27}Si calibration reaction are shown in Figure 3.7-Figure 3.12. This is followed by the triton position spectra from the ^{39}K(^{3}He,t)^{39}Ca production reaction in Figure 3.14-Figure 3.19.

From the MLL experiment, the triton position spectra from the ^{32}S(d,t)^{31}S calibration reaction are shown in Figure 3.20 - Figure 3.23. The triton position spectra of the ^{40}Ca(d,t)^{39}Ca reaction are shown in Figure 3.24-Figure 3.27.

This is followed by the compiled energies from the TUNL experiment in Table 3.1, the compiled energies from the MLL experiment in Table 3.2. Finally the results from the experiments of this work are compared against the results from Setoodehnia et al. [23], and Hall et al. [22] in Table 3.4, and their weighted averages are taken.

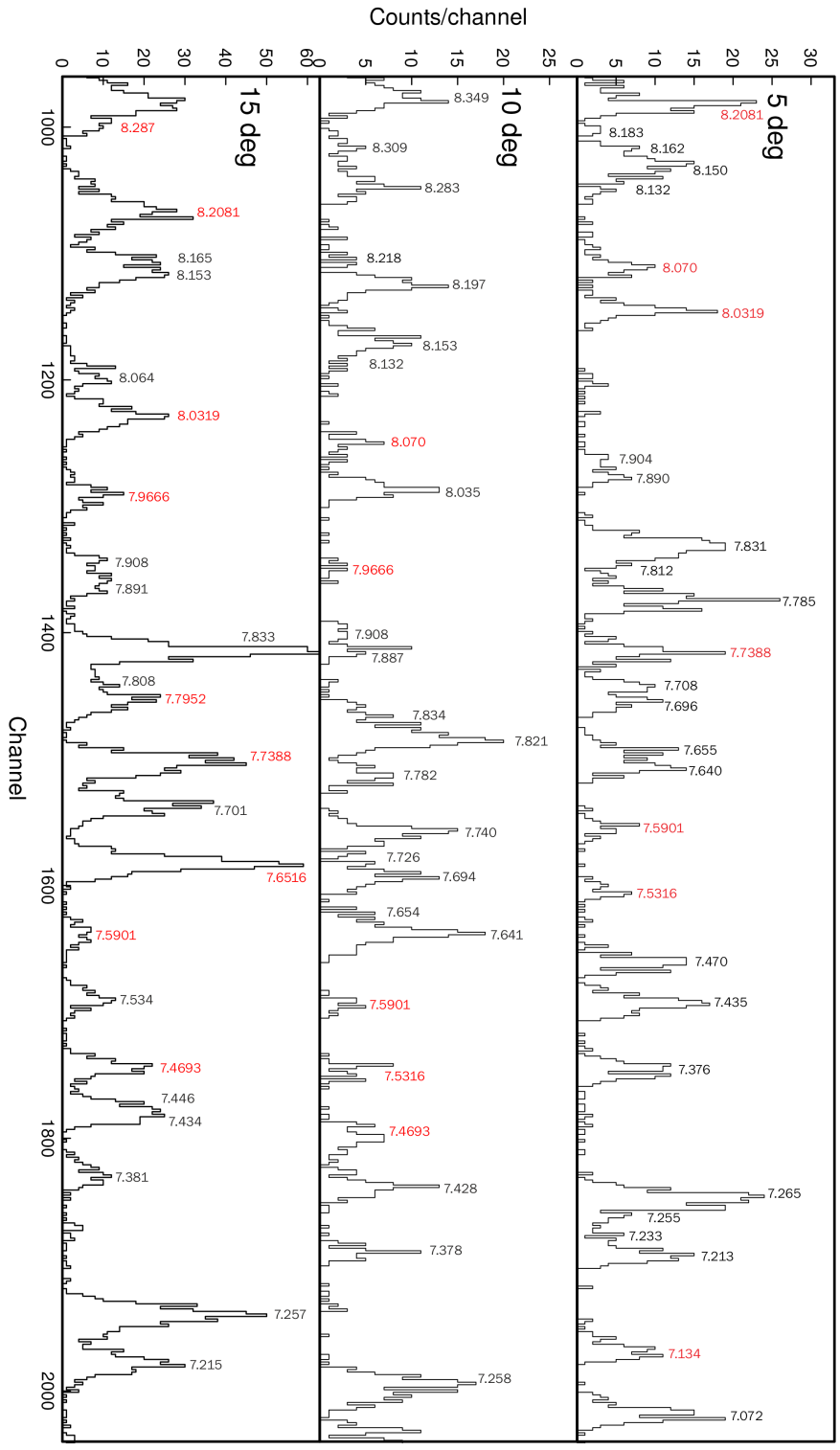

FIGURE 3.7: TUNL triton spectra for ^{27}Al(^{3}He,t)^{27}Si at spectrograph angles between 5-15 degrees. Energy listed in MeV. Red denotes a peak used in the calibration.

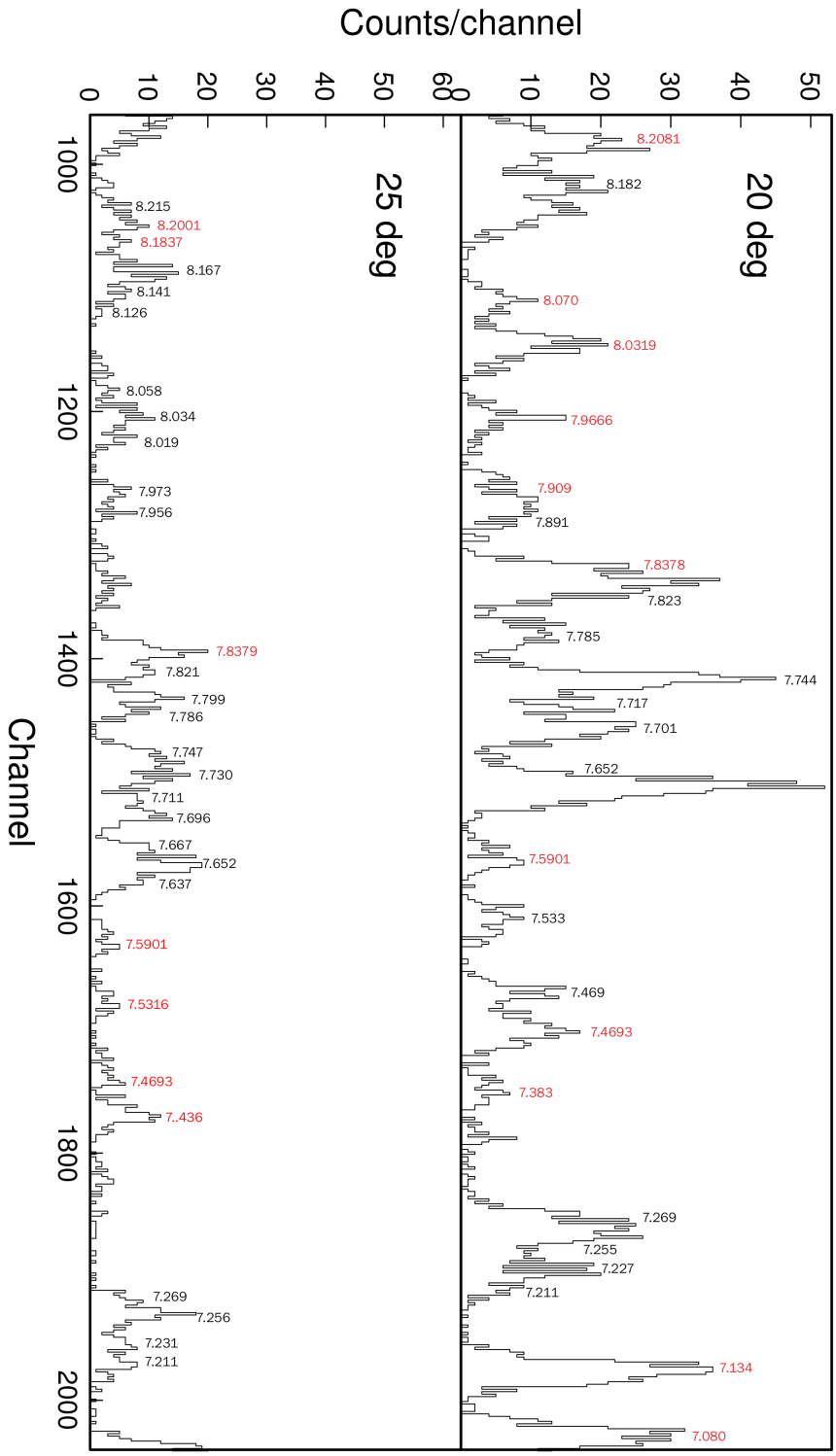

FIGURE 3.8: TUNL triton spectra for ^{27}Al(^{3}He,t)^{27}Si at spectrograph angles between 20-25 degrees. Energy listed in MeV. Red denotes a peak used in the calibration.

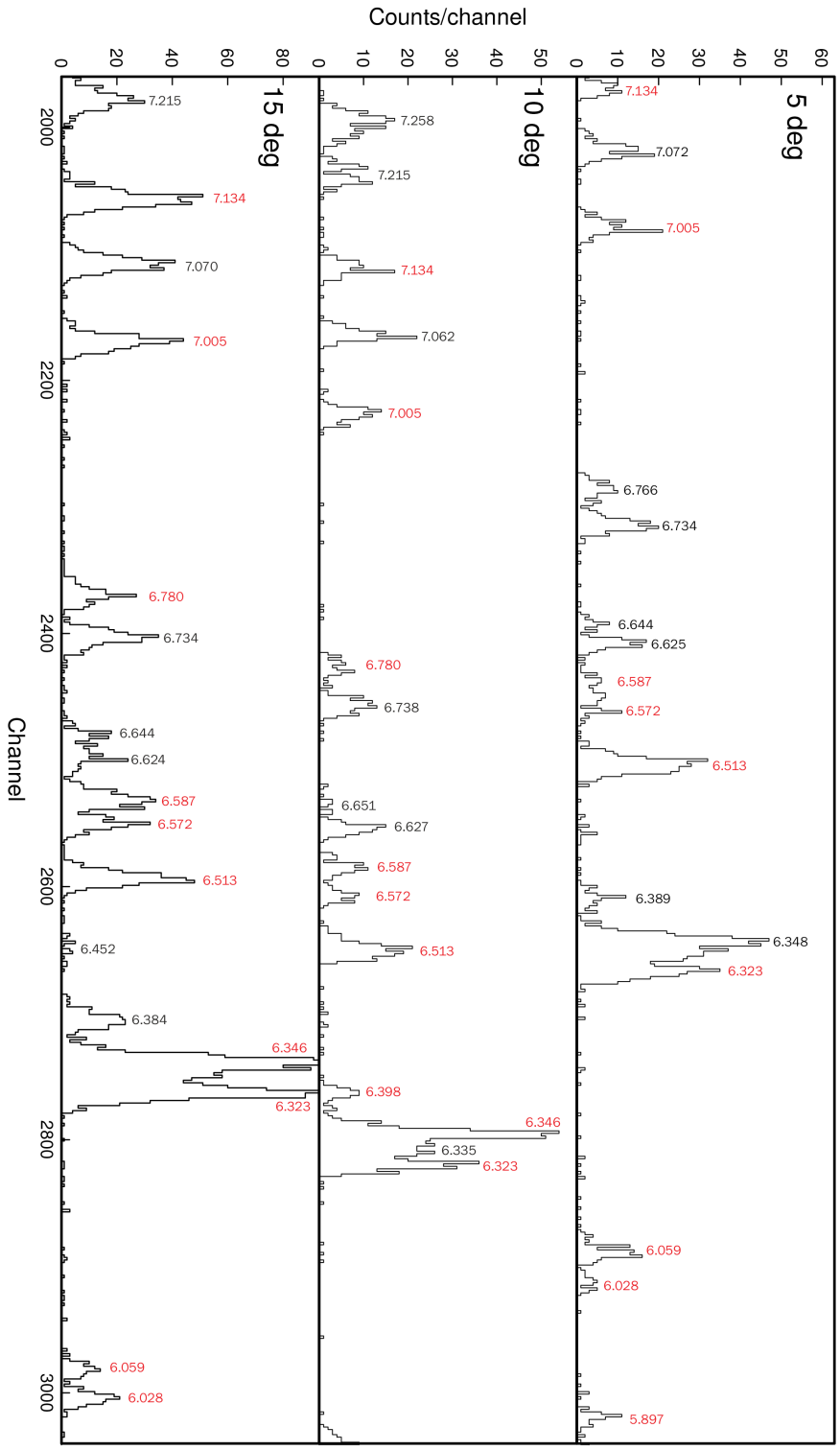

FIGURE 3.9: TUNL triton spectra for ^{27}Al(^{3}He,t)^{27}Si at spectrograph angles between 5-15 degrees. Energy listed in MeV. Red denotes a peak used in the calibration.

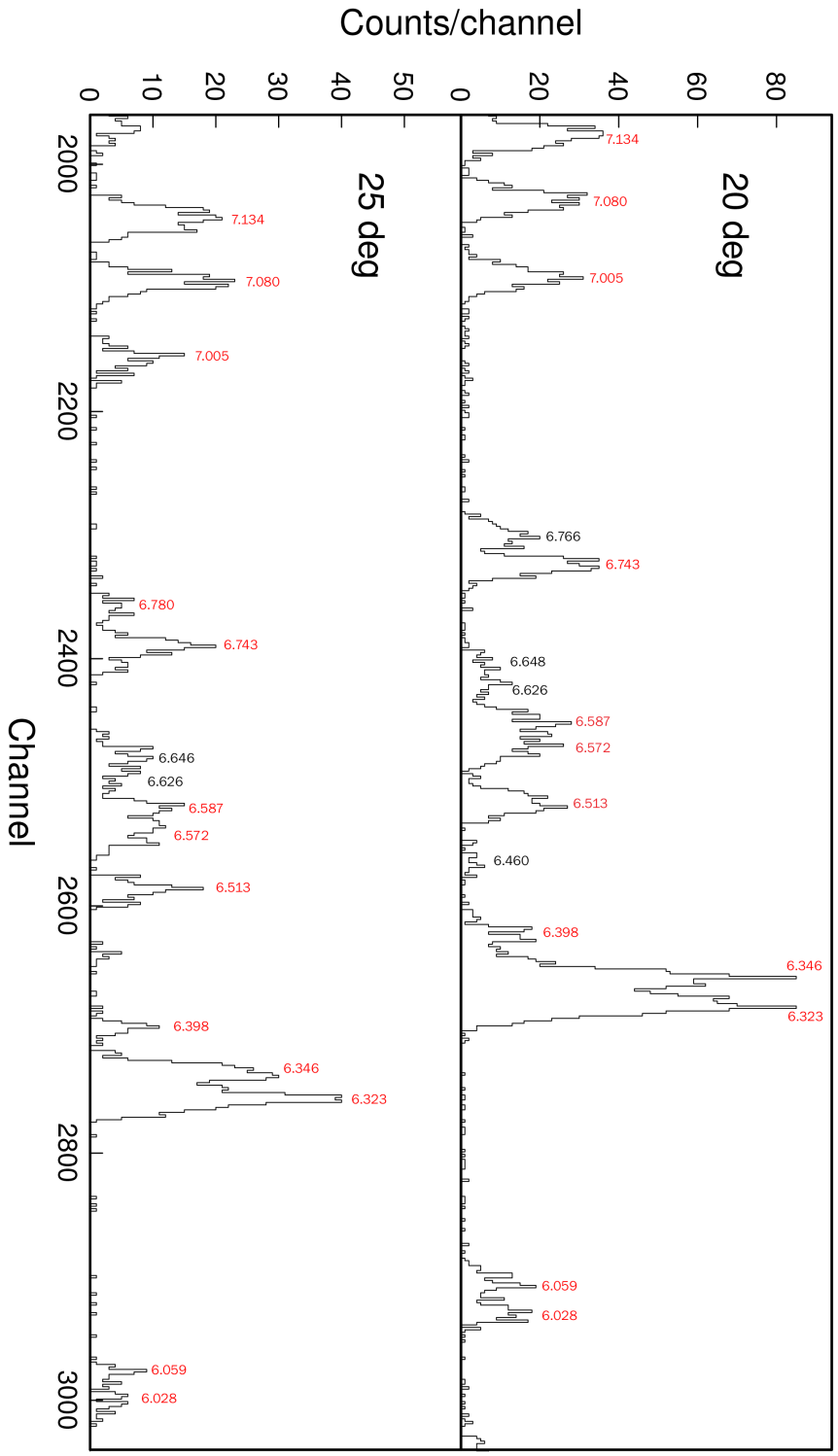

FIGURE 3.10: TUNL triton spectra for ^{27}Al(^{3}He,t)^{27}Si at spectrograph angles between 20-25 degrees. Energy listed in MeV. Red denotes a peak used in the calibration.

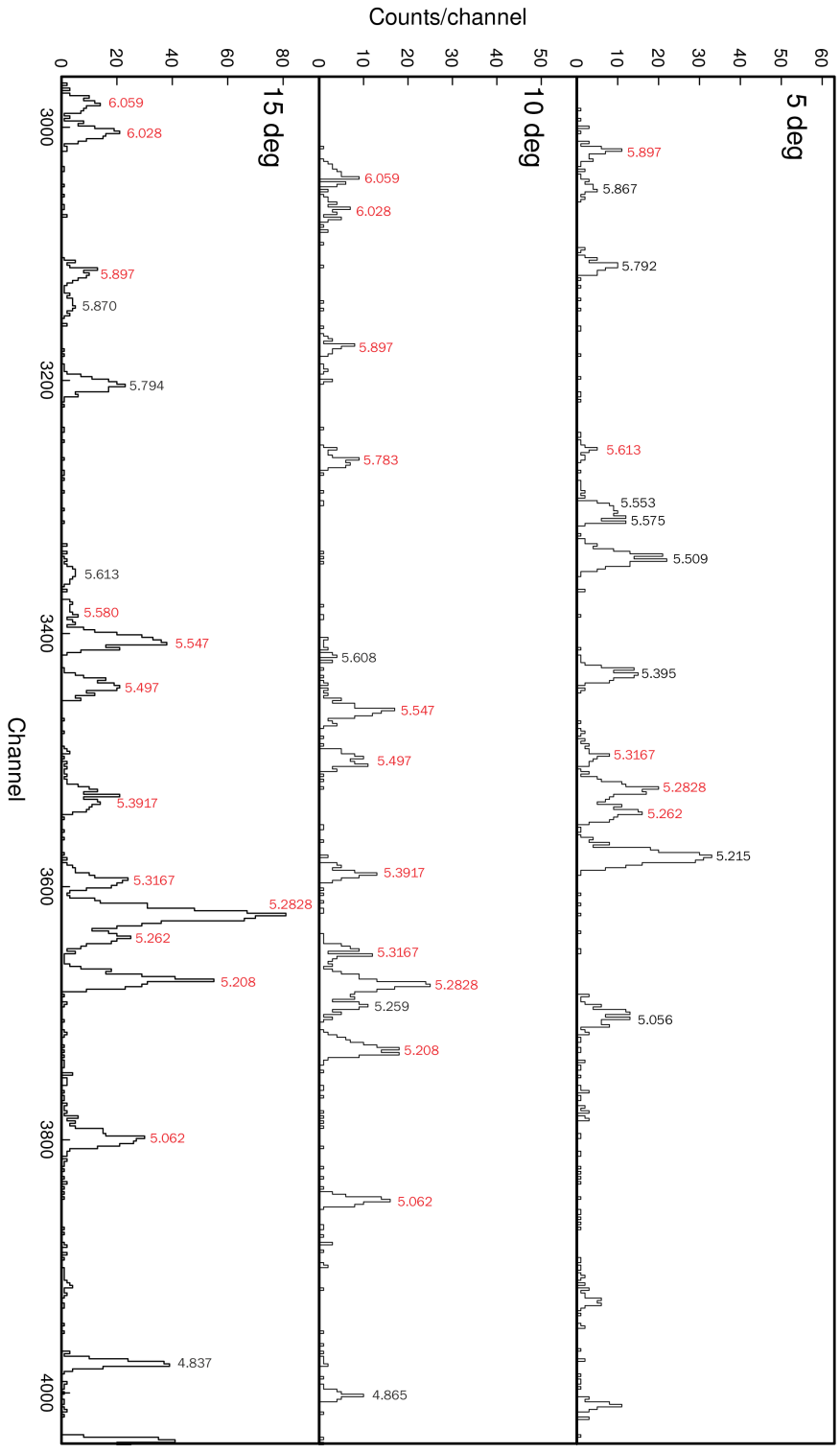

FIGURE 3.11: TUNL triton spectra for ^{27}Al(^{3}He,t)^{27}Si at spectrograph angles between 5-15 degrees. Energy listed in MeV. Red denotes a peak used in the calibration.

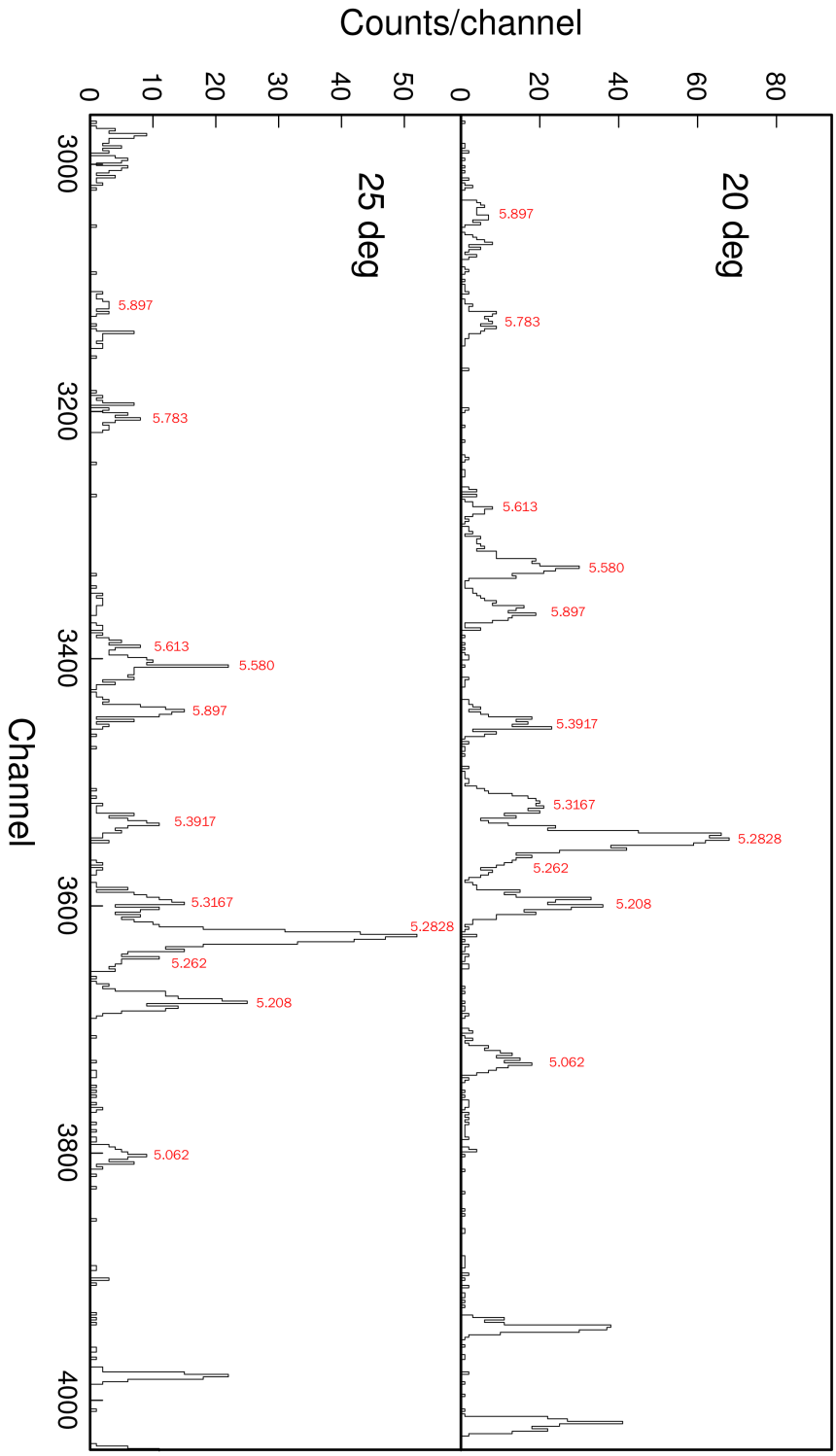

FIGURE 3.12: TUNL triton spectra for ^{27}Al(^{3}He,t)^{27}Si at spectrograph angles between 20-25 degrees. Energy listed in MeV. Red denotes a peak used in the calibration.

SpecPlot

SpecPlot is a code developed by staff at TUNL in the R language to simulate the positions of tritons on the focal plane after passing through the spectrograph. The code takes in the parameters of the experiment such as the magnetic field, beam energy, and reaction, and it is able to calculate the bending radius of a reaction product that is sorted through the spectrograph. Then, using the known excitation energies of the residual nucleus, it is able to plot where resonance peaks would occur on the focal plane. For our data, the tritons from different excited states are shown in Figure 3.13 where the SpecPlot simulation result of the ^{27}Al(^{3}He,t)^{27}Si calibration reaction at 20° is overlaid on the respective triton spectrum. Once several peaks are matched to states in ^{27}Si, a polynomial fit can be made to convert the triton position spectrum to a triton energy spectrum. This polynomial fit can then be used to deduce the energies of tritons in the production target, and thus the energies of the residual nucleus that are being populated in the resonance.

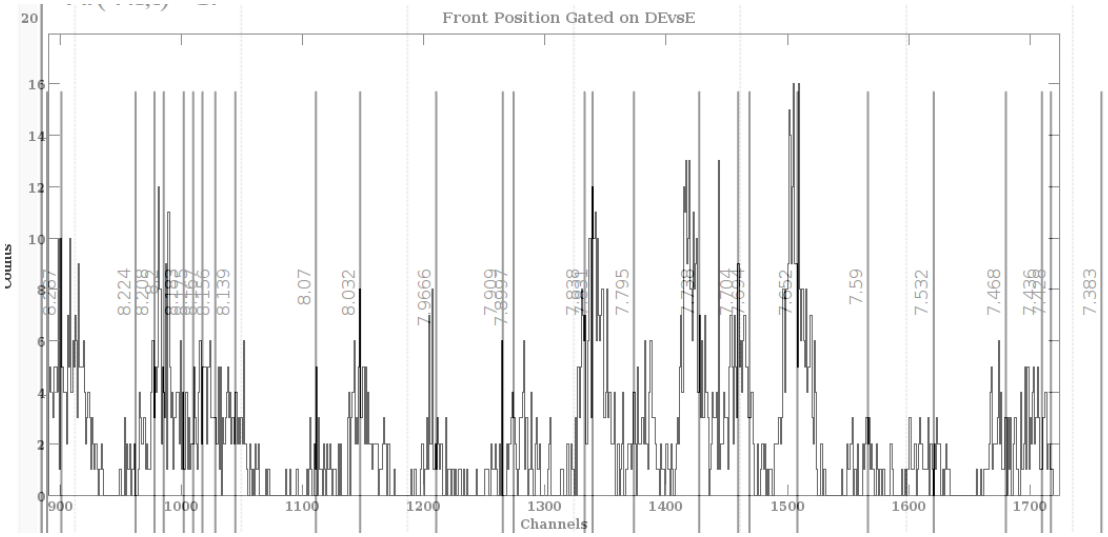

FIGURE 3.13: Overlay of SpecPlot predicted positions of triton peaks at 20° spectrograph angle for the ^{27}Al(^{3}He,t)^{27}Si reaction on the actual data from the experiment carried out at TUNL. The number displayed is the state of ^{27}Si that the triton peak corresponds to. By predicting the locations of peaks with Specplot, the position channel can be mapped to triton kinetic energy.

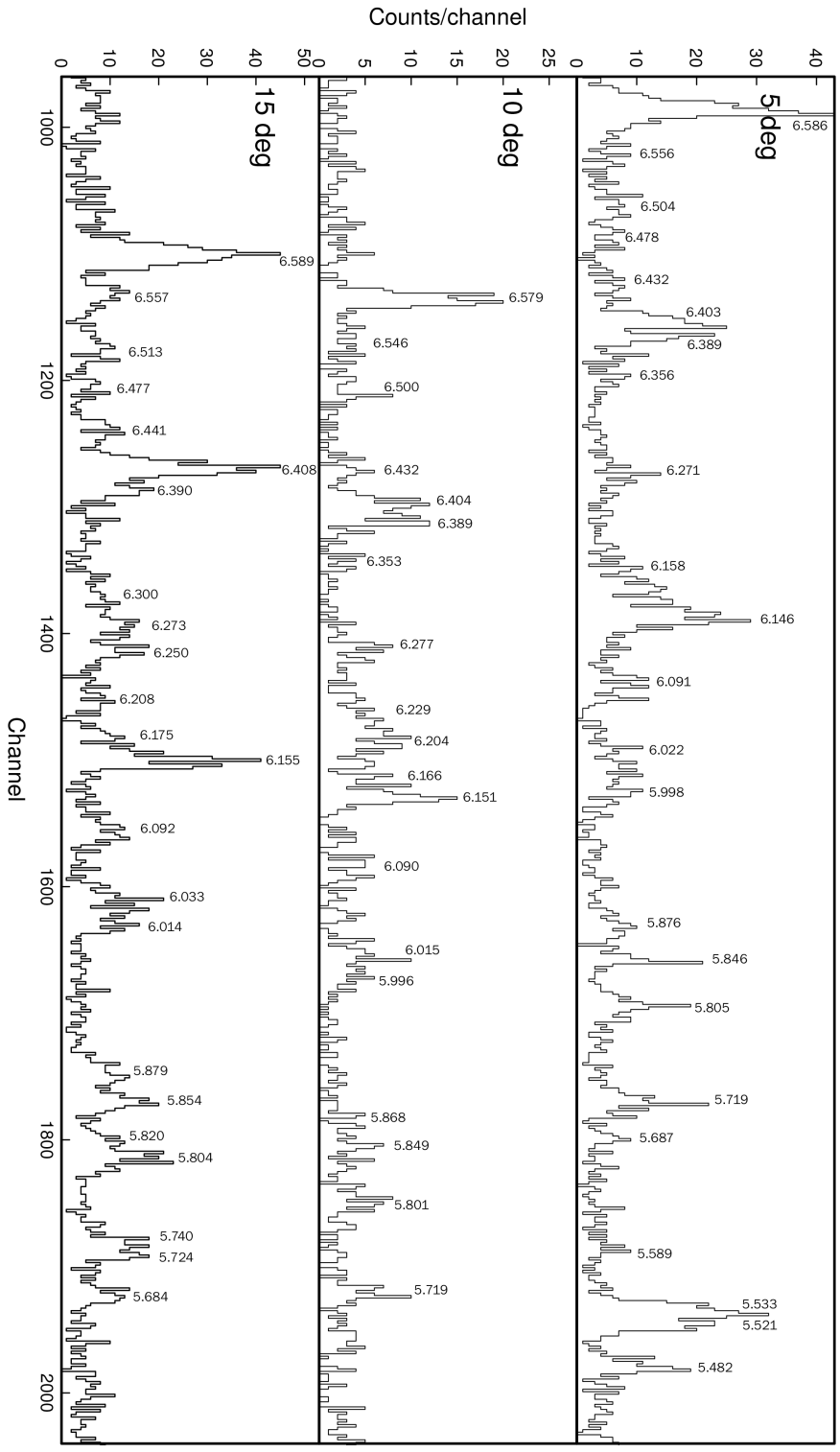

FIGURE 3.14: TUNL triton spectra for ^{39}K(^{3}He,t)^{39}Ca at spectrograph angles between 5-15 degrees. Energy listed in MeV

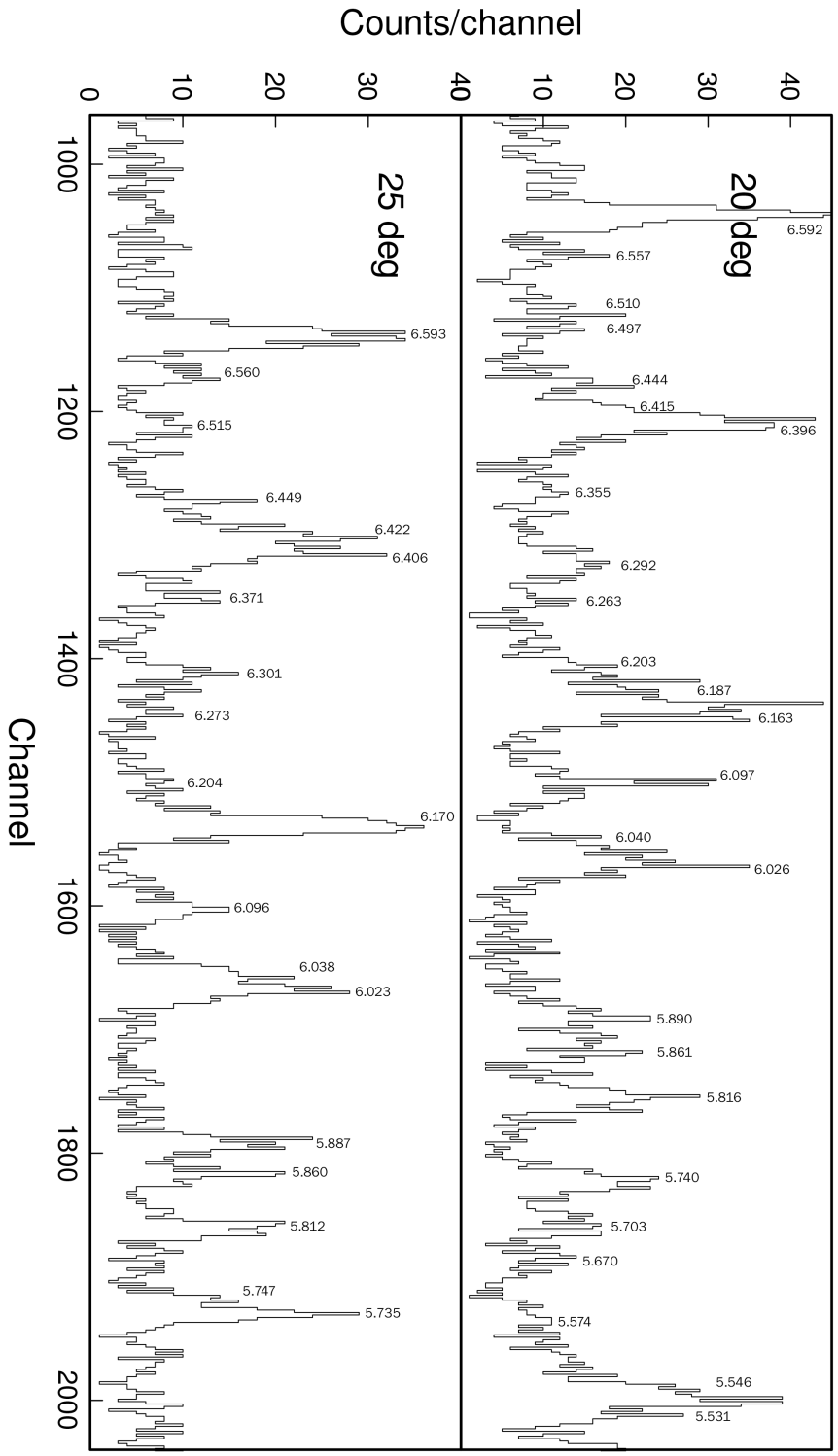

FIGURE 3.15: TUNL triton spectra for ^{39}K(^{3}He,t)^{39}Ca at spectrograph angles between 20-25 degrees. Energy listed in MeV

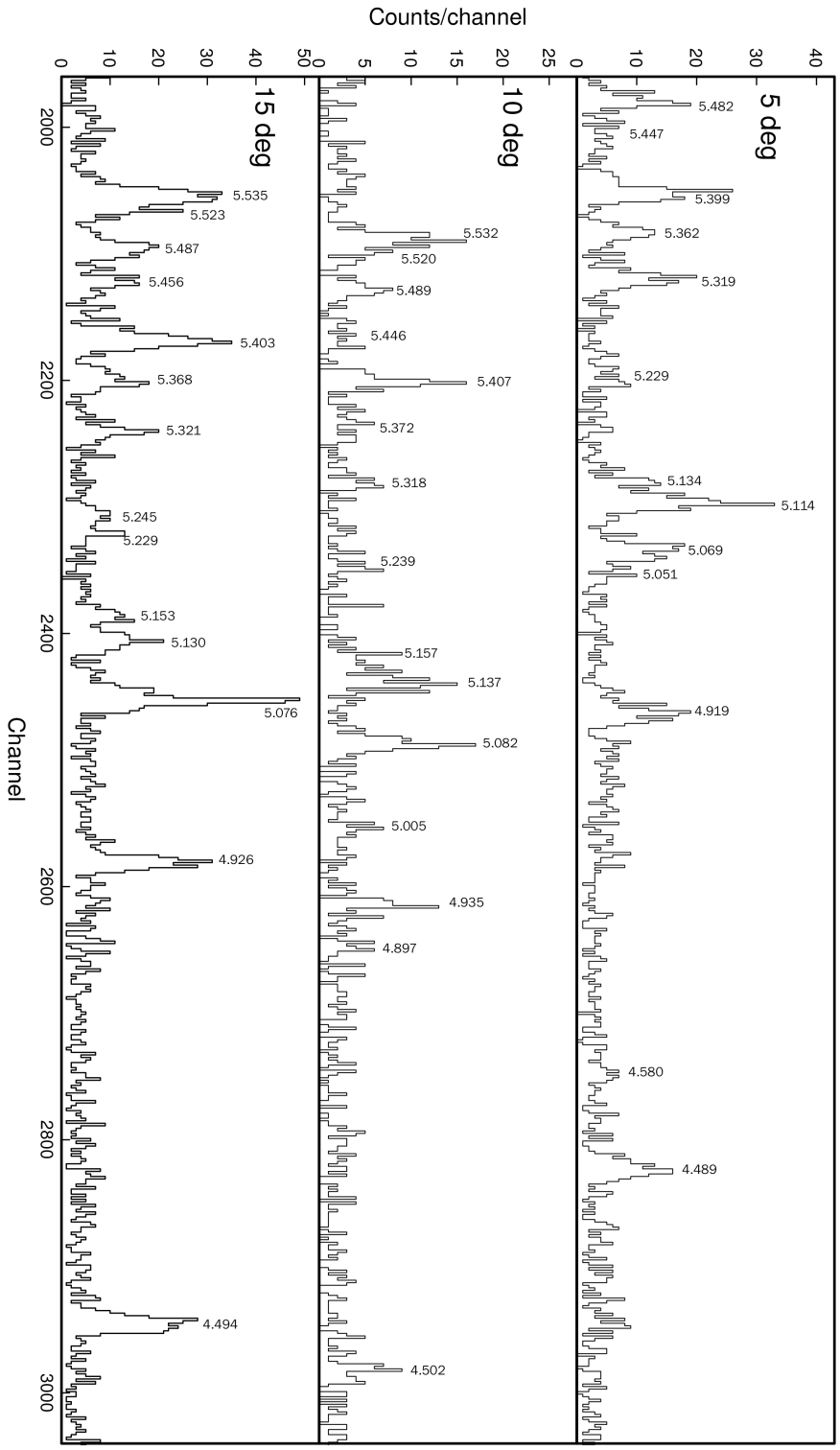

FIGURE 3.16: TUNL triton spectra for ^{39}K(^{3}He,t)^{39}Ca at spectrograph angles between 5-15 degrees. Energy listed in MeV

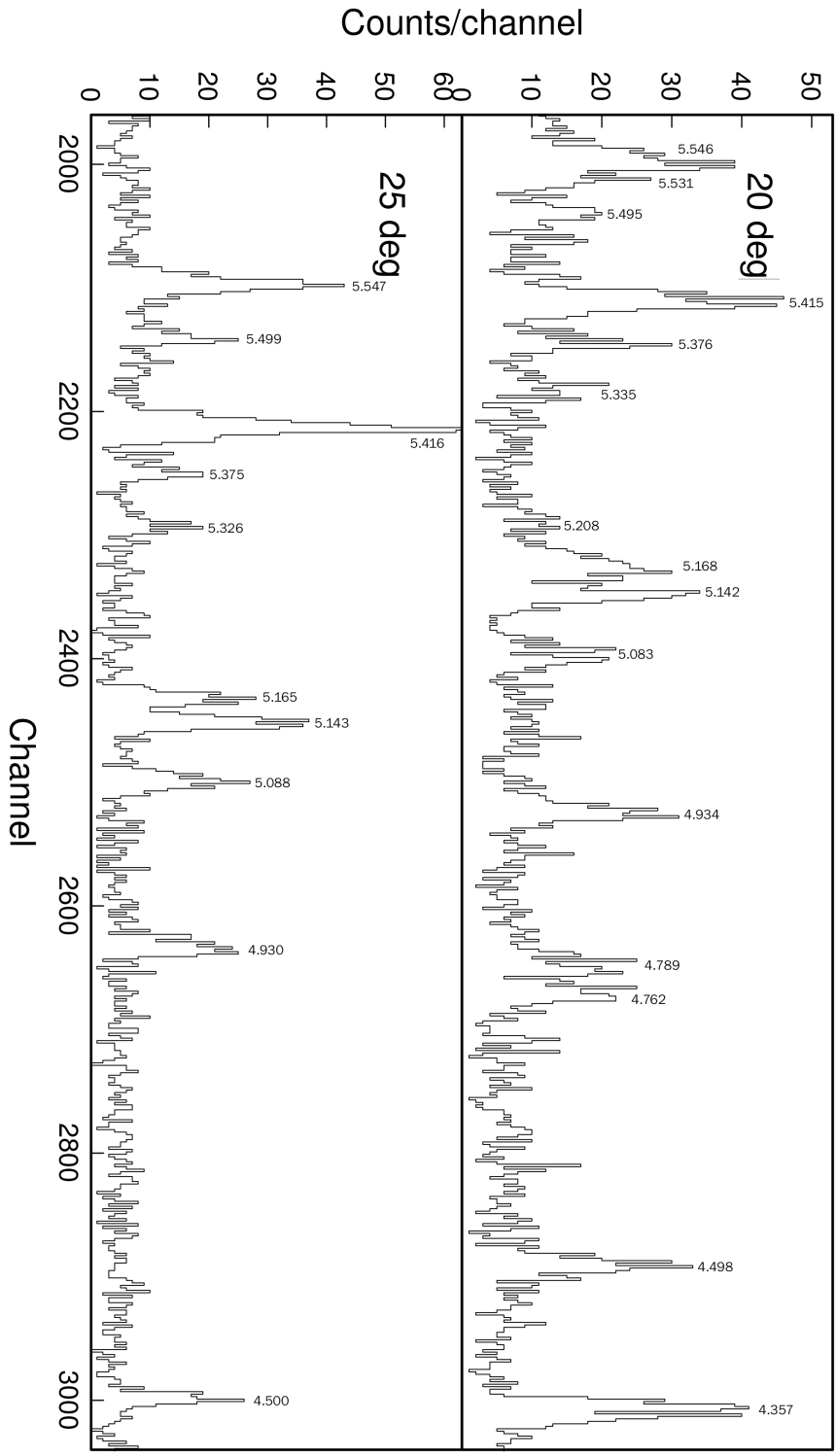

FIGURE 3.17: TUNL triton spectra for ^{39}K(^{3}He,t)^{39}Ca at spectrograph angles between 20-25 degrees. Energy listed in MeV

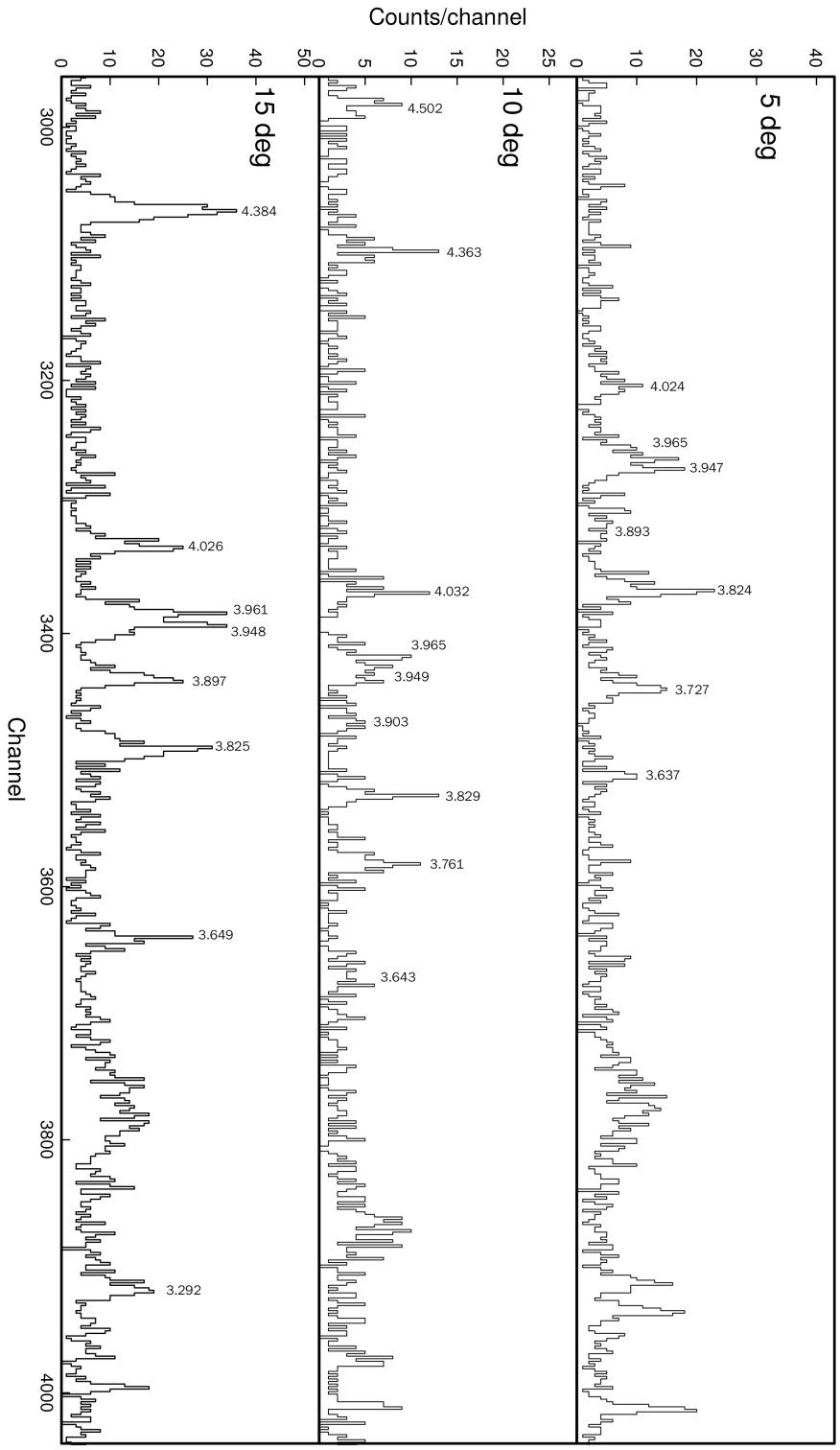

FIGURE 3.18: TUNL triton spectra for ^{39}K(^{3}He,t)^{39}Ca at spectrograph angles between 5-15 degrees. Energy listed in MeV

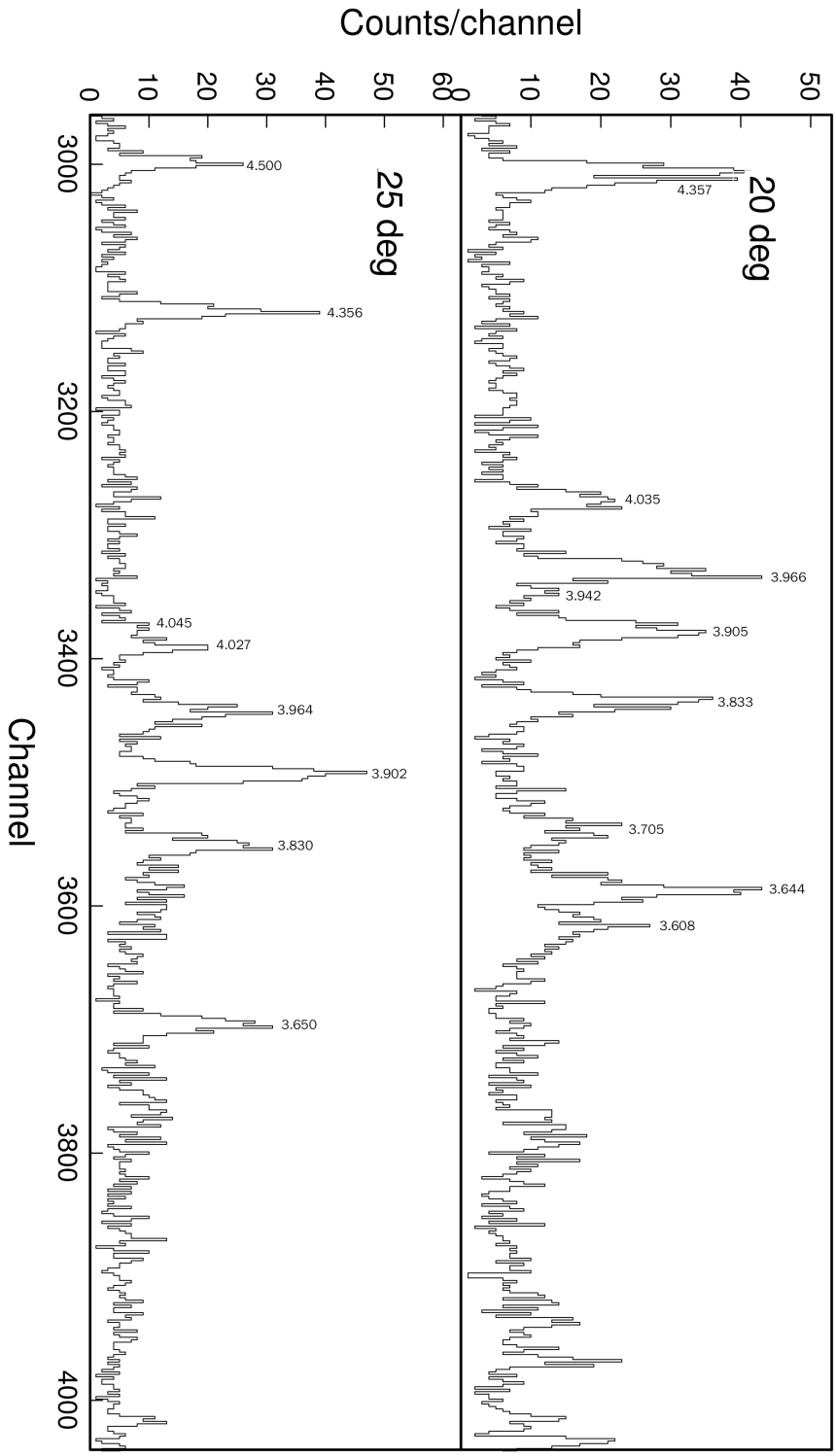

FIGURE 3.19: TUNL triton spectra for ^{39}K(^{3}He,t)^{39}Ca at spectrograph angles between 20-25 degrees. Energy listed in MeV

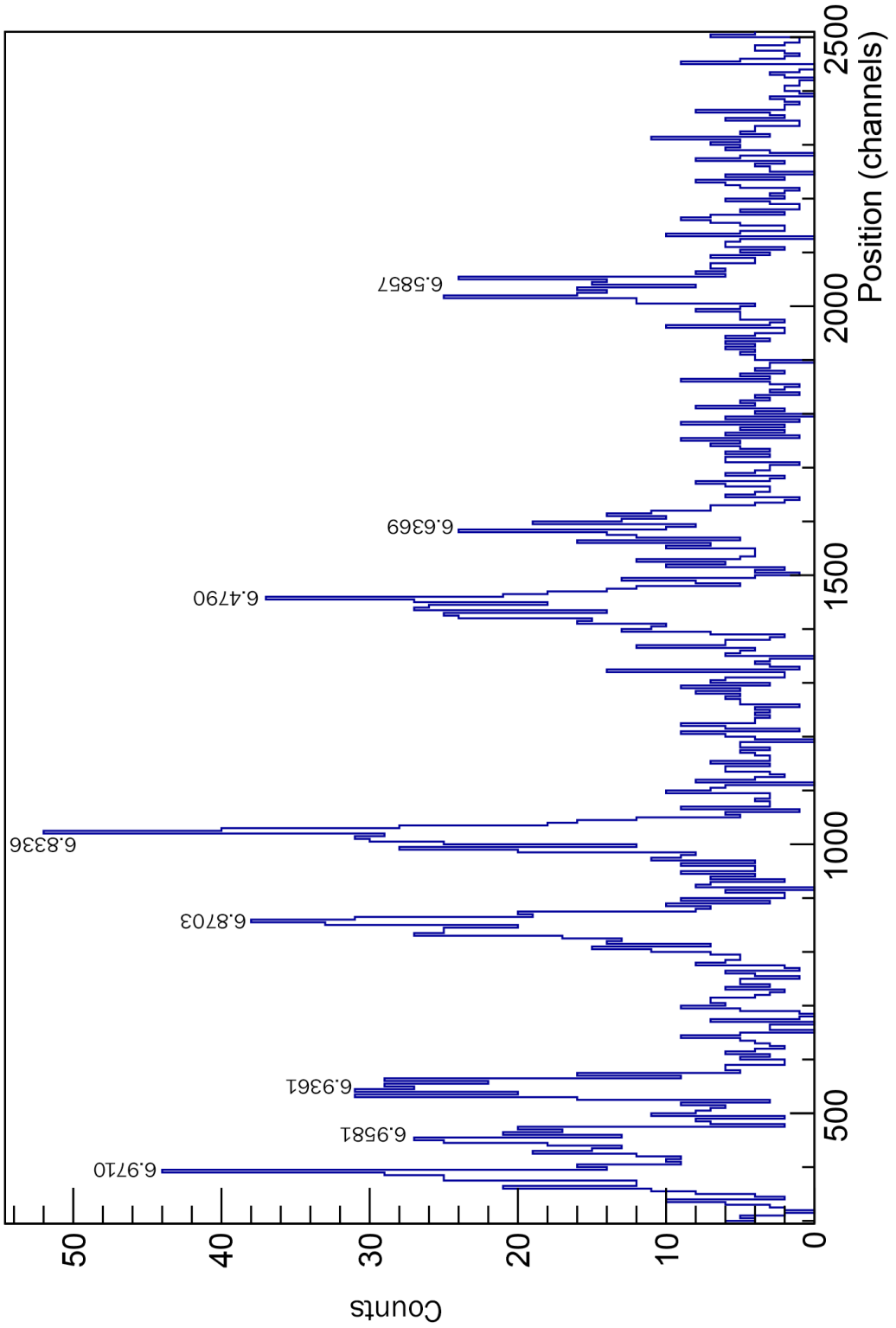

FIGURE 3.20: MLL triton spectra for ^{32}S(d,t)^{31}S at 15 degrees. Energy listed in MeV.

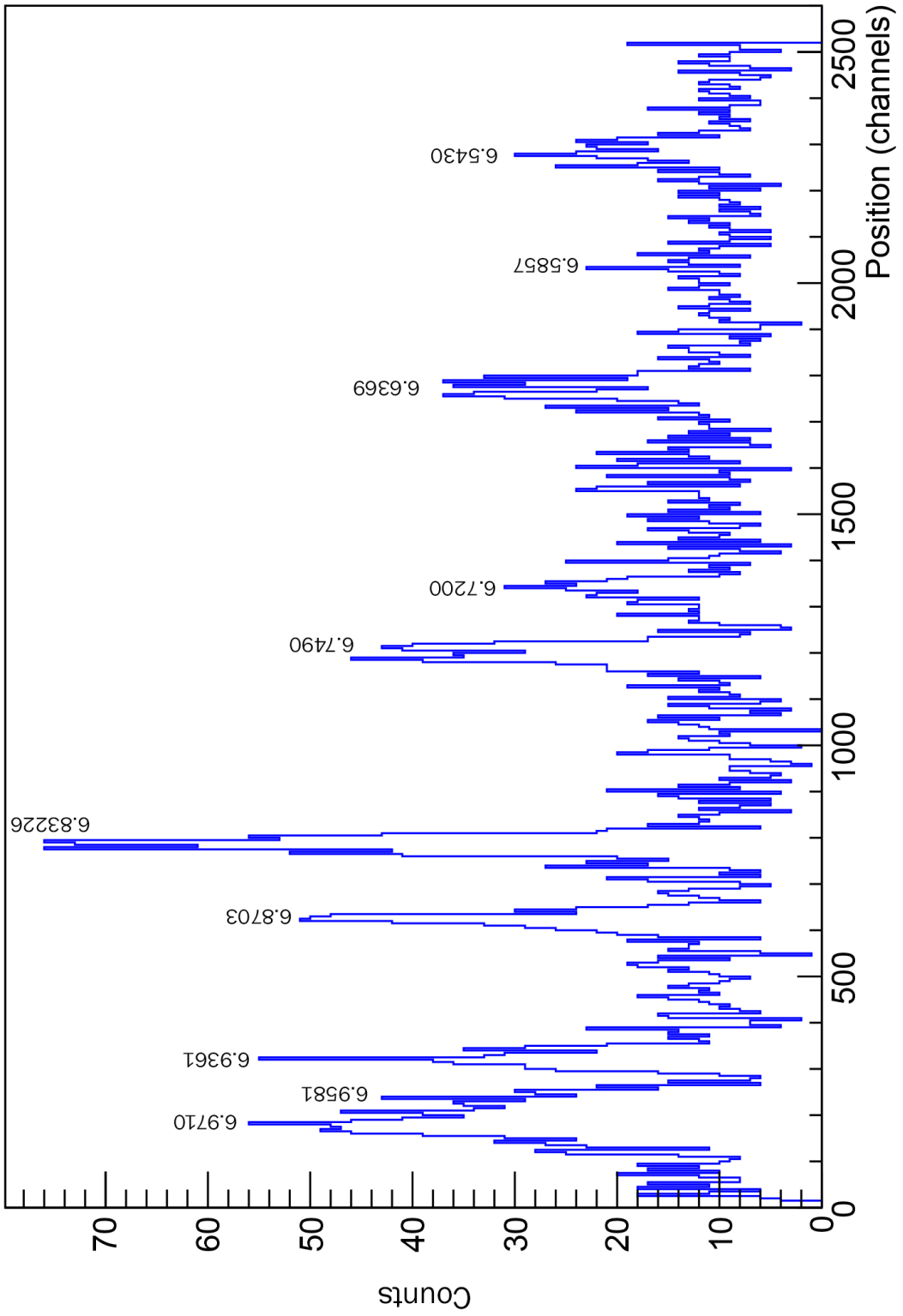

FIGURE 3.21: MLL triton spectra for ^{32}S(d,t)^{31}S at 20 degrees. Energy listed in MeV.

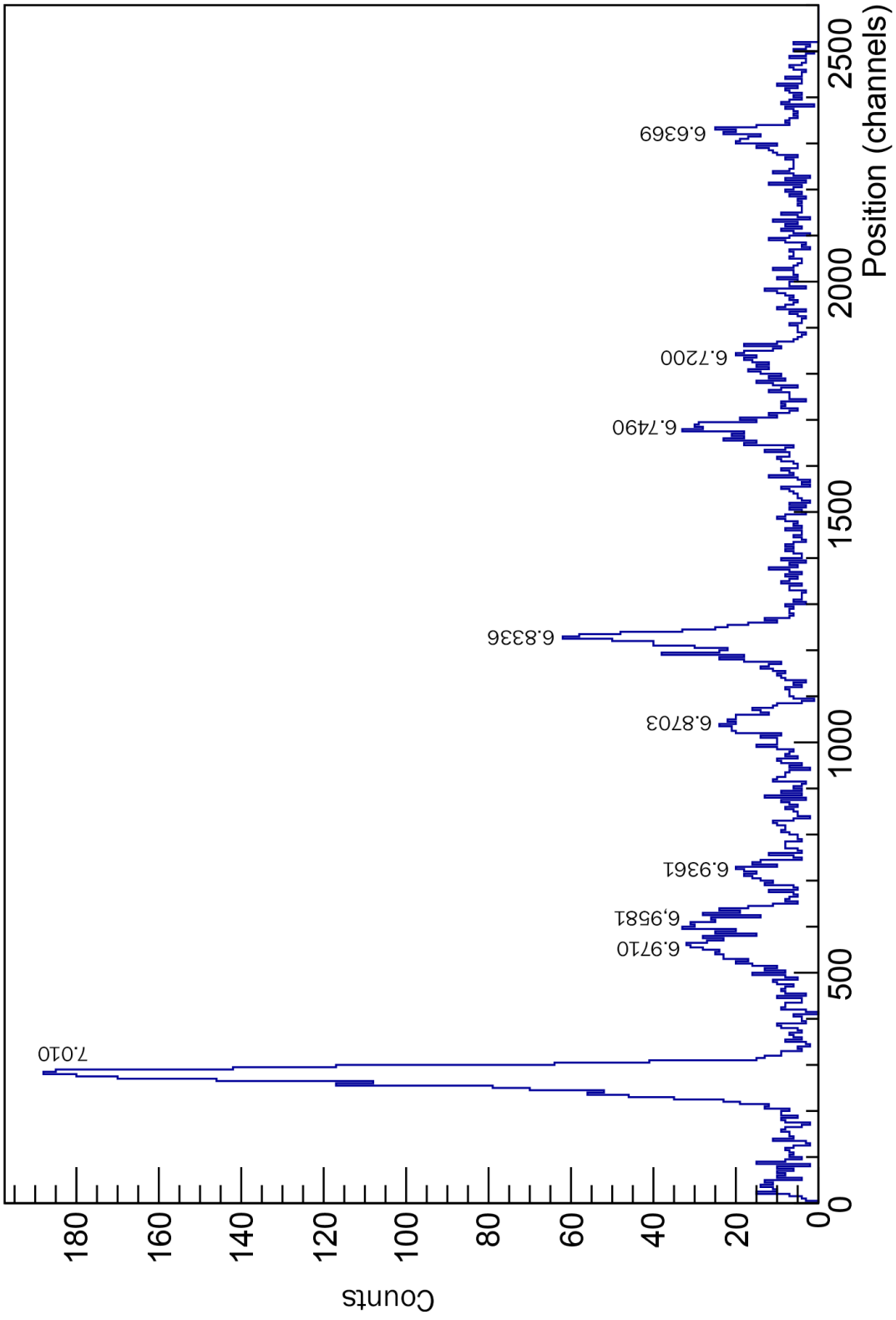

FIGURE 3.22: MLL triton spectra for ^{32}S(d,t)^{31}S at 25 degrees. Energy listed in MeV.

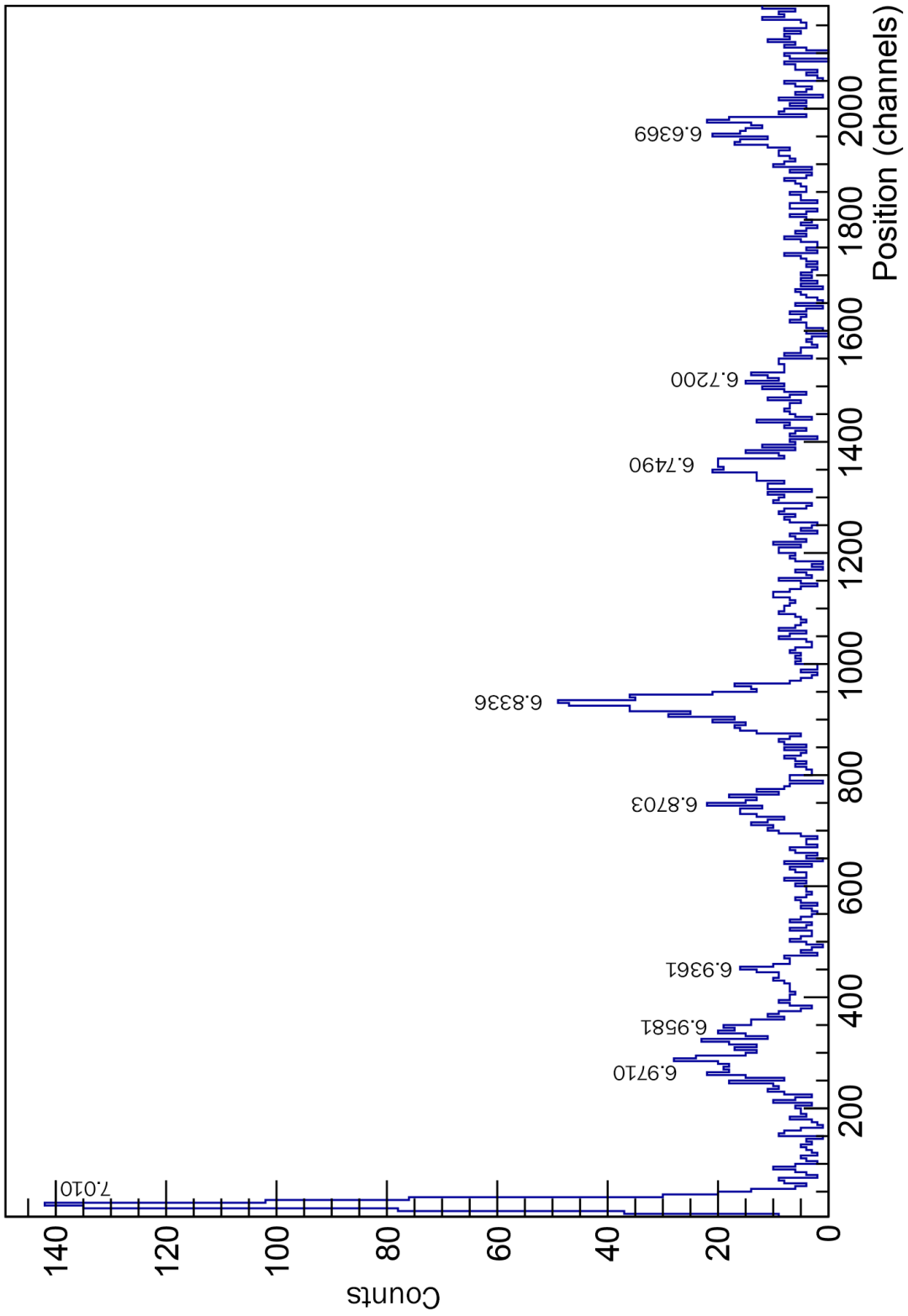

FIGURE 3.23: MLL triton spectra for ^{32}S(d,t)^{31}S at 30 degrees. Energy listed in MeV.

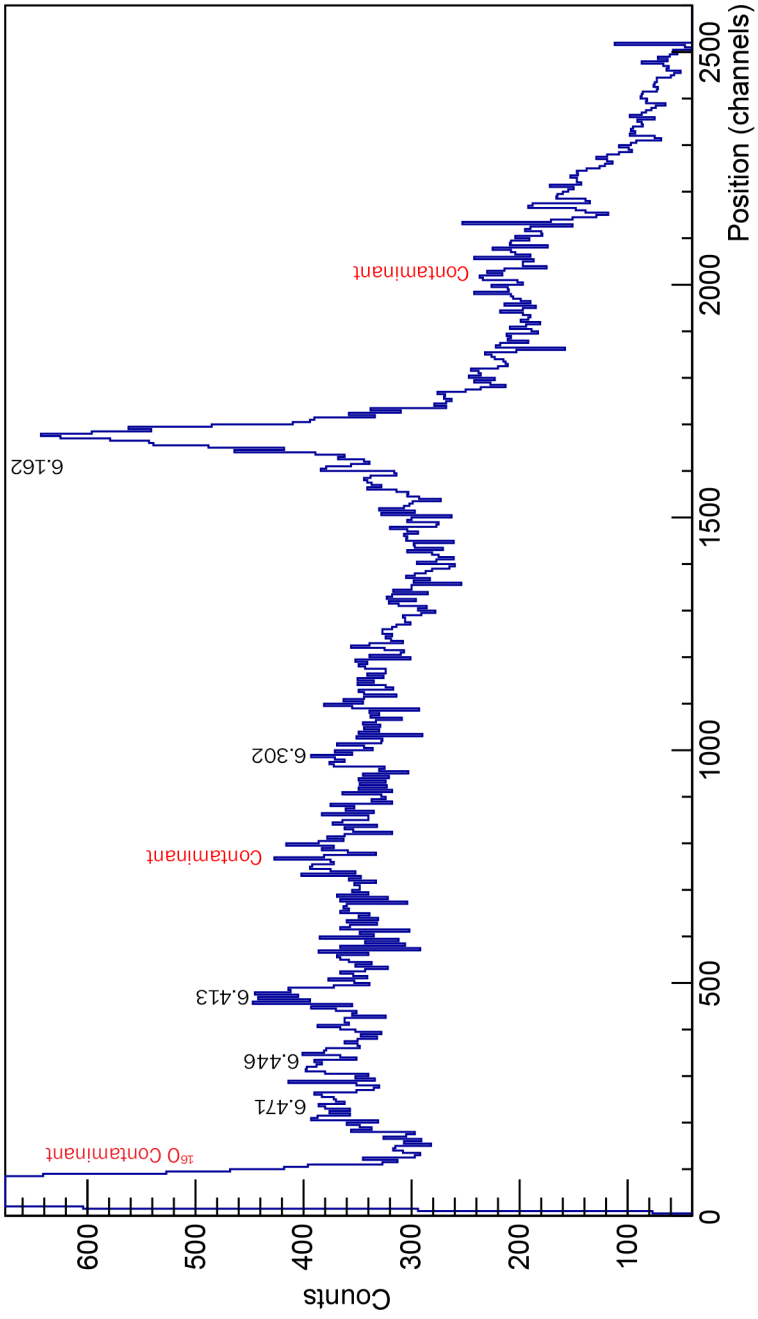

FIGURE 3.24: MLL triton spectra for ^{40}Ca(d,t)^{39}Ca at 15 degrees. Energy listed in MeV.

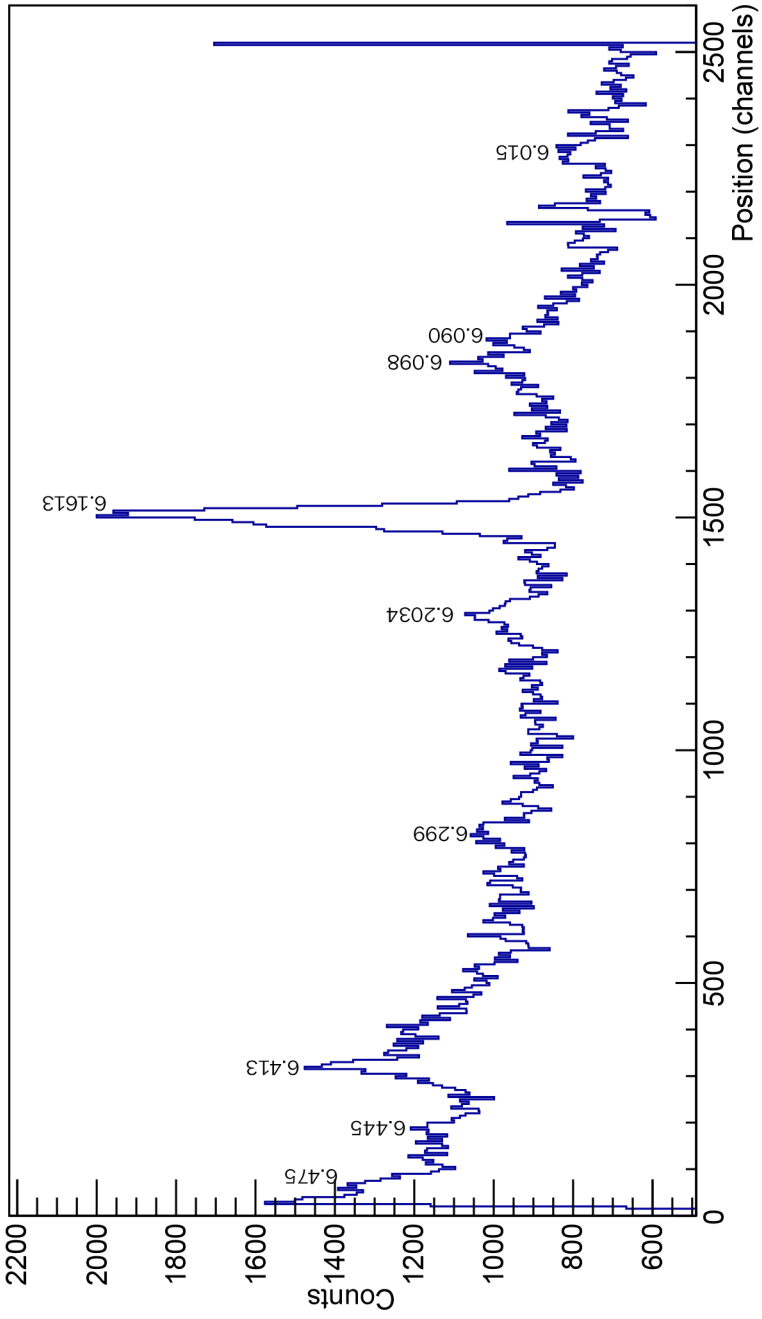

FIGURE 3.25: MLL triton spectra for ^{40}Ca(d,t)^{39}Ca at 20 degrees. Energy listed in MeV.

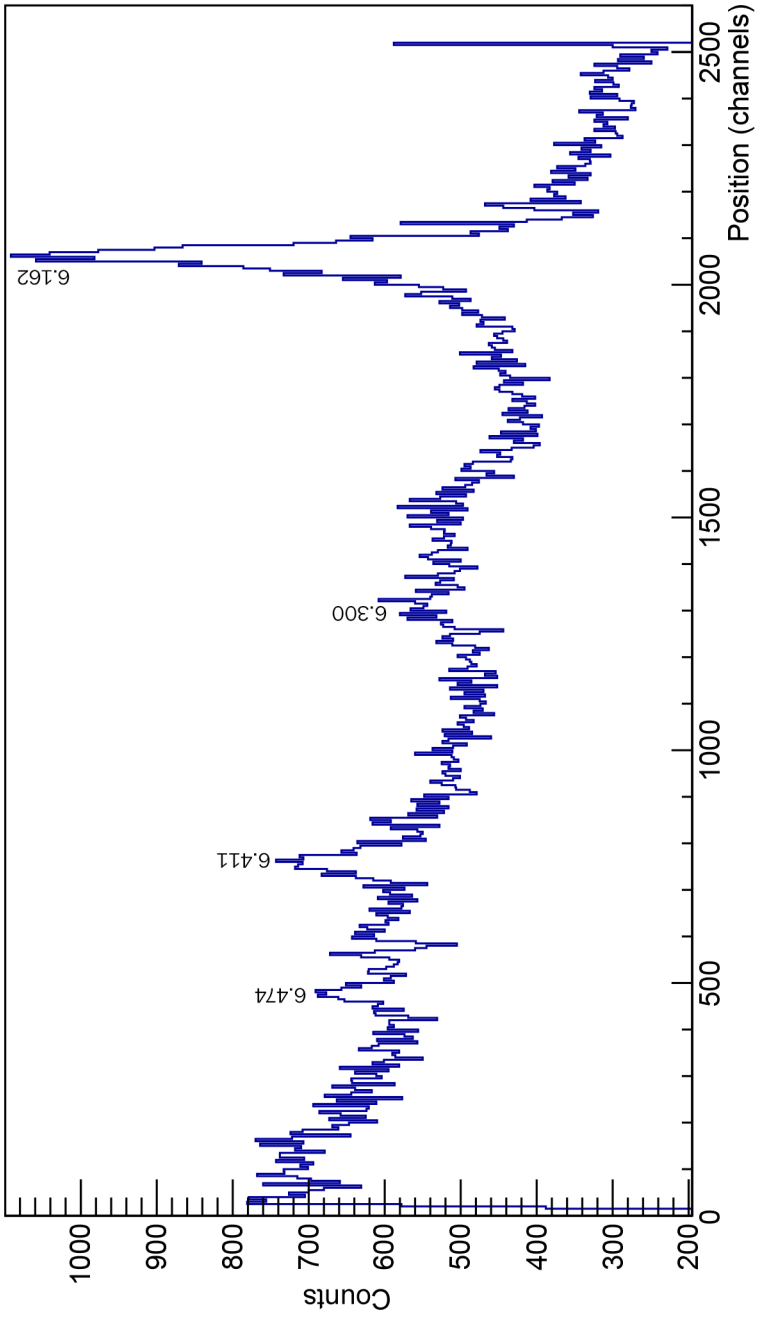

FIGURE 3.26: MLL triton spectra for ^{40}Ca(d,t)^{39}Ca at 25 degrees. Energy listed in MeV.

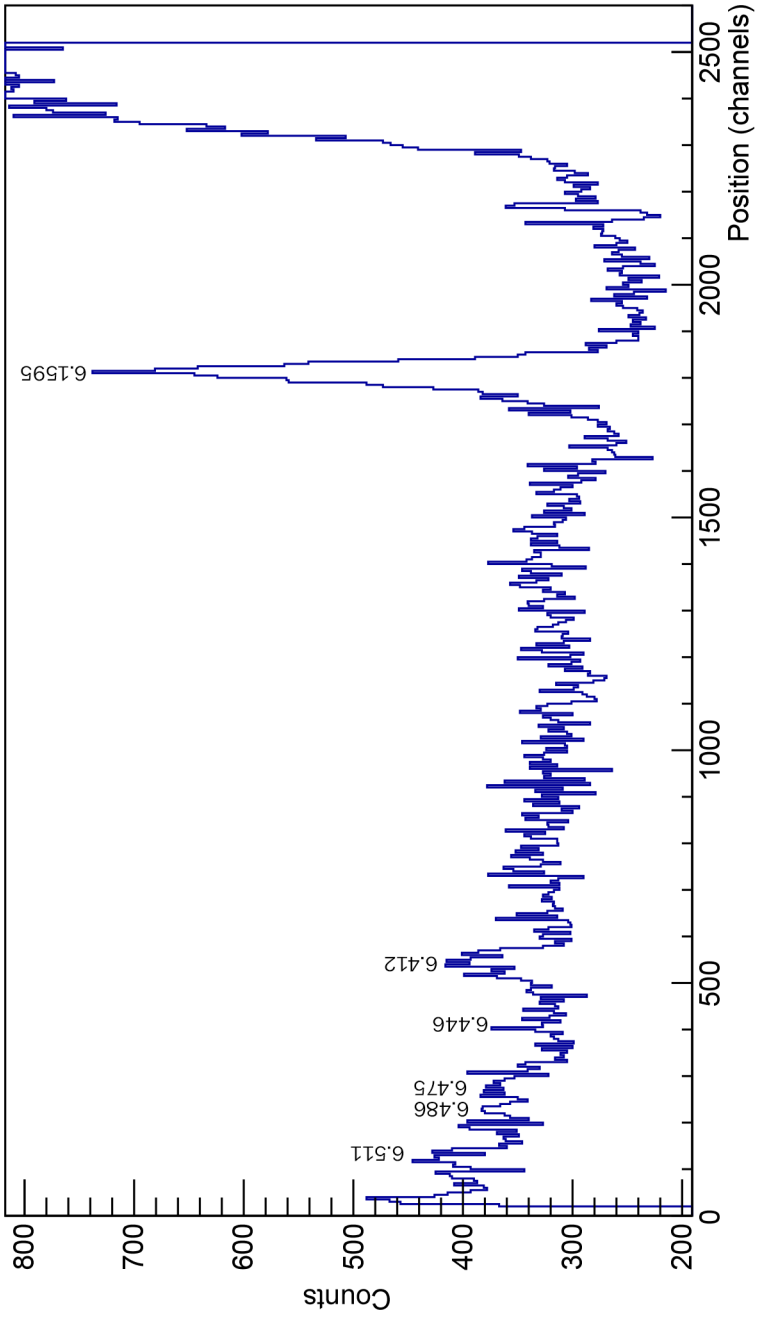

FIGURE 3.27: MLL triton spectra for ^{40}Ca(d,t)^{39}Ca at 30 degrees. Energy listed in MeV.

TABLE 3.1: Compilation of experimental data for ^{39}Ca energies (in MeV) in the ^{39}K(^{3}He,t)^{39}Ca reaction (Figure 3.14-Figure 3.19). Statistical uncertainties are shown, systematic uncertainty added in quadrature when determining the weighted average (WA) in final column.

5° E_x (keV)	10° E_x (keV)	15° E_x (keV)	20° E_x (keV)	25° E_x (keV)	WA E_x (keV)
6.586(5)	6.579(2)	6.589(4)	6.592(4)	6.593(3)	6.587(3)
6.556(8)	6.546(5)	6.557(4)	6.557(4)	6.560(3)	6.556(3)
6.504(3)	6.500 (3)	6.513(5)	6.510(7)	6.515(3)	6.507(3)
6.478(5)		6.477(7)	6.497(7)		6.483(6)
6.433(4)	6.432(3)				
		6.441(4)	6.444(3)	6.449(3)	6.445(3)
				6.422(3)	
6.403(3)	6.404(2)	6.409(3)	6.415(3)	6.406(2)	6.407(3)
6.390(5)	6.389(2)	6.390(3)	6.396(4)		
				6.371(3)	
6.356(5)	6.353(3)		6.355(4)		6.354(2)
		6.300(5)	6.292(3)	6.301(2)	6.298(4)
6.271(2)	6.277(2)	6.273(3)	6.263(5)	6.273(5)	6.273(3)
		6.250(3)			
	6.204(4)	6.208(4)	6.203(13)	6.204(3)	6.204(3)
	6.166(3)	6.175(3)	6.187(8)		
6.158(3)	6.151(2)	6.155(2)	6.163(2)	6.170(2)	6.160(3)
6.146(2)					
6.091(2)	6.090(3)	6.093(2)	6.097(2)	6.096(2)	6.094(2)
		6.033(2)	6.040(5)	6.038(2)	6.036(2)
6.022(4)	6.015(3)	6.014(3)	6.026(3)	6.023(2)	6.020(3)
5.998(3)	5.996(5)				
5.876(2)	5.869(7)	5.879(2)	5.890(2)	5.887(1)	5.883(3)
5.847(2)	5.849(4)	5.855(2)	5.861(2)	5.860(2)	5.844(3)
		5.820(3)	5.817(2)	5.812(1)	5.815(3)
5.805(1)	5.801(2)	5.804(2)			5.804(3)
		5.740(7)	5.740(2)	5.747(3)	5.743(4)
5.720(1)	5.720(2)	5.724(2)	5.703(2)	5.735(2)	5.720(5)

TABLE 3.1: Compilation of experimental data for ^{39}Ca energies (in MeV) in the ^{39}K(^{3}He,t)^{39}Ca reaction (Figure 3.14-Figure 3.19). Statistical uncertainties are shown, systematic uncertainty added in quadrature when determining the weighted average (WA) in final column.

5° E_x (keV)	10° E_x (keV)	15° E_x (keV)	20° E_x (keV)	25° E_x (keV)	WA E_x (keV)
5.687(2)		5.684(2)	5.670(3)		5.682(5)
5.589(3)			5.574(3)		
			5.546(2)	5.547(1)	
5.533(1)	5.532(1)	5.535(2)	5.531(3)		5.533(2)
5.521(1)	5.520(4)	5.523(2)			5.521(3)
5.482(1)	5.489(2)	5.487(1)	5.495(2)	5.499(1)	5.490(3)
5.447(6)	5.446(6)	5.456(2)			5.452(3)
5.399(1)	5.407(1)	5.404(1)	5.415(1)	5.416(1)	5.408(3)
5.362(1)	5.373(5)	5.368(2)	5.376(2)	5.375(2)	5.370(3)
5.320(1)	5.318(2)	5.321(2)	5.335(3)	5.326(2)	5.323(3)
		5.245(3)			
5.229(3)	5.239(2)	5.229(3)			5.233(4)
			5.208(4)		
	5.157(3)	5.153(2)	5.168(2)	5.165(1)	5.161(3)
5.133(2)	5.137(1)	5.130(1)	5.142(1)	5.143(1)	5.137(3)
5.114(1)					
5.069(1)	5.082(1)	5.076(1)	5.083(2)	5.088(1)	5.079(3)
5.051(4)					
	5.005(3)				
4.919(1)	4.935(2)	4.926(1)	4.934(1)	4.930(1)	4.928(3)
	4.898(3)		4.789(2)		
			4.762(2)		
4.580(3)					
4.489(1)	4.502(2)	4.494(1)	4.498(2)	4.500(1)	4.496(2)
	4.363(2)	4.348(1)	4.357(1)	4.356(1)	4.355(3)
4.025(2)	4.032(2)	4.026(2)	4.035(2)	4.027(2)	4.029(2)
				4.045(4)	
3.965(8)	3.965(2)	3.961(2)	3.966(2)	3.965(2)	3.964(2)

TABLE 3.1: Compilation of experimental data for ^{39}Ca energies (in MeV) in the ^{39}K(^{3}He,t)^{39}Ca reaction (Figure 3.14-Figure 3.19). Statistical uncertainties are shown, systematic uncertainty added in quadrature when determining the weighted average (WA) in final column.

5° E_x (keV)	10° E_x (keV)	15° E_x (keV)	20° E_x (keV)	25° E_x (keV)	WA E_x (keV)
3.947(3)	3.949(3)	3.948(2)	3.942(4)	3.948(4)	3.947(3)
3.893(4)	3.903(3)	3.897(2)	3.905(2)	3.902(2)	3.901(2)
3.824(2)	3.829(2)	3.825(2)	3.833(2)	3.830(2)	3.828(2)
3.727(2)	3.761(2)				
			3.705(4)		
3.637(3)	3.643(4)	3.641(3)	3.644(3)	3.649(2)	3.643(3)

TABLE 3.2: Excitation energies of ^{39}Ca (in MeV) determined from triton spectra from the ^{40}Ca(d,t)^{39}Ca reaction, statistical uncertainties shown. Weighted average (WA) shown in final column with systematic uncertainties added in quadrature to statistical uncertainties of each peak.

15° E_x (keV)	20° E_x (keV)	25° E_x (keV)	30° E_x (keV)	WA E_x (keV)
			6.511(4)	
6.471 (5)	6.475(2)	6.474(2)	6.475(3)	6.474(1)
6.446(5)	6.445(2)		6.446(2)	6.446(1)
6.413(2)	6.413(1)	6.411(1)	6.412(1)	6.4120(6)
6.302(1)	6.299(1)	6.302(2)		6.301(1)
6.162(2)	6.1613(7)	6.162(3)	6.1595(6)	6.1604(6)
	6.098(1)			
	6.090(1)			
	6.015(3)			

3.2 Results and Discussion

The uncertainty in the energy for the MLL data is determined through the following process: The statistical uncertainty comes from the error associated with the χ^2 minimization fit. The systematic uncertainty results from a discrepancy in the evaluated energies in ^{31}S produced by the ^{32}S target. These discrepancies emerge from conflicting evaluated data sets that were averaged in ENSDF [21][17] and span $\approx$ 4 keV. A previous treatment by Fry et. al.[52] shifted the energy down 2 keV (the value that would be between the discrepant measurements) and attached a 2 keV uncertainty when calibrating with ^{31}S states.

The uncertainty in the TUNL data is determined through the following process: The uncertainty of the MCMC sampling is combined in quadrature with the experimental error when determining the channel number in the triton peak centroid. This error is propagated through Monte Carlo sampling through the reaction kinematic equations [43]. The energy values from this sampling is well approximated with a normal distribution, and the standard deviation is the uncertainty.

The sources of systematic uncertainties in the TUNL data are: 1) $\pm$10% thickness on the evaporated KI and Al targets [23], which affects the energy of the outgoing triton by up to 1.2 keV, 2) uncertainties in the Q value of the reactions taking place with the ^{39}K and ^{27}Al nuclei, which are 0.1 and 0.6 keV respectively, and 3) uncertainty in the beam energy, as the terminal voltage varied up to 0.002 MV during the runs at a given angle.

For a ^{3}He beam, this amounts to an error of ±6 keV. Adding these uncertainties in quadrature yields a total systematic uncertainty of 6.2 keV for each individual peak, the dominant uncertainty being from the drifting terminal voltage. Statistical uncertainties for each peak were on the order of 2-4 keV, yielding a total uncertainty of 6-7 keV when added in quadrature.

In the calibration process for each experiment, attention was paid to ensure there were no outliers affecting the polynomial fit. Figure 3.28 shows the experimentally measured points with blue points, and the calculated fit in the solid black line. The reduced χ^2 of these fits are typically between 2-3. Measured calibration points that were outliers were excluded from the fit as they may have been contaminants or mislabeled peaks.

The weighted average of peak measurements at each angle was taken to obtain a final value. These final values typically had uncertainty of approximately 2-5 keV. During the weighted average, the reduced χ^2 of the energy values were observed to be below the critical χ^2 needed for a 95% confidence level. A weighted average was only taken when three or more consistent measurements were found at various angles.

When comparing the resonance levels obtained in these works to ENSDF compiled data for ^{39}Ca [17], we notice that our work is systematically higher than the ENSDF averages. This can be attributed to more precise recent measurements of the masses of ^{39}Ca which ultimately affects the Q-value used during the deduction of each energy level measured. In the most recent Atomic Mass Evaluation conducted in 2016 (AME2016) [53], the mass excess of ^{39}Ca was reported as -27282.702 (596) keV. The mass excess found in the AME2003 [54] was -27274.4(1.9) keV showing that there is an approximately 8.3 keV difference in these masses. The effect of using the newer, "lighter" mass is that the Q-values of reactions producing ^{39}Ca are larger, and the deduced energies are systematically higher than the older compiled values from the previous measurements of ^{39}Ca resonances. Additionally, when the older AME2003 is used in the analysis we find that the deduced energies fall within 1 σ of the previous literature values, which is tabulated in Table 3.3.

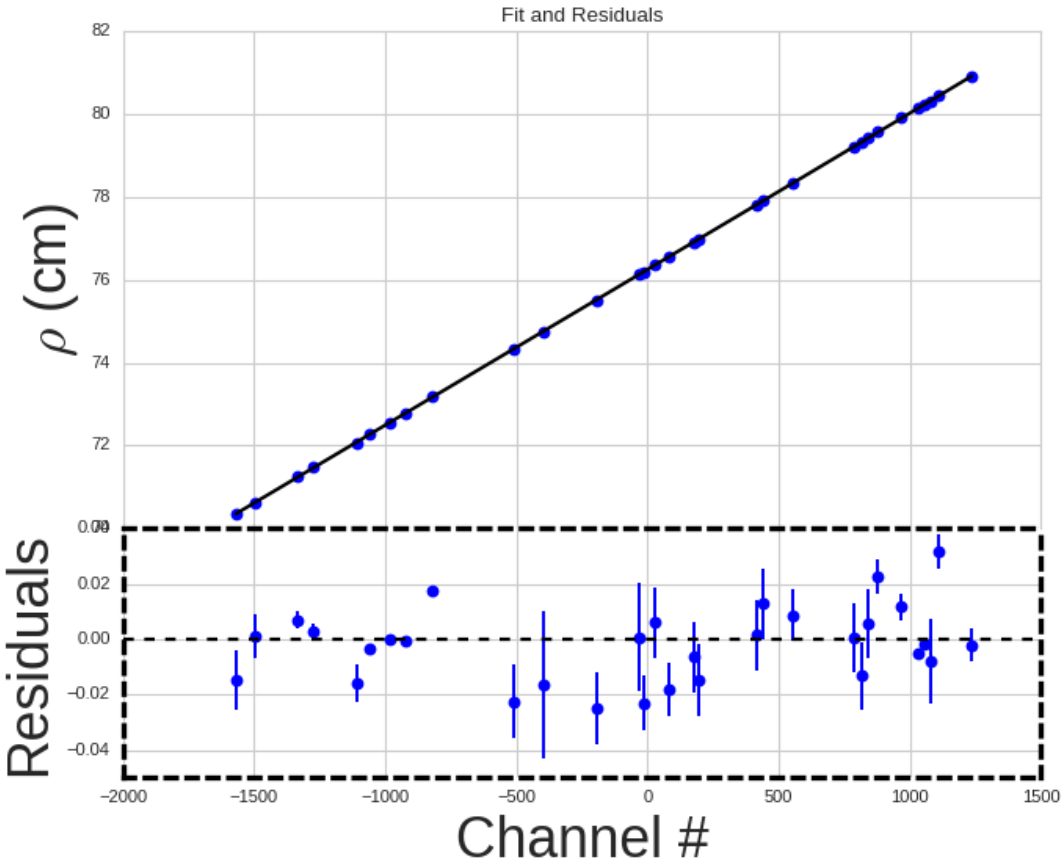

FIGURE 3.28: TUNL calibration data obtained from the ^{27}Al(^{3}He,t)^{27}Si reaction. The above plot compares the polynomial calibration fit in solid black line to the measured points in blue dots, with channel number on the x-axis and the radius of curvature, ρ, on the y-axis. Through the residual plot on the bottom panel, we can see that no outlier would strongly shift the polynomial fit and that there is no significant systematic error at work.

TABLE 3.3: Energy values from MLL experiment analyzed with AME2003 data compared to current ENSDF values for energy levels in ^{39}Ca. Weighted average of MLL data shown.

E_x MeV (MLL + AME2003)	E_x MeV (ENSDF) [17]
6.4592(6)	6.451(2)
6.431(2)	6.432(2)
6.4003(4)	6.405(10)
6.289(1)	6.286(10)
6.1507(1)	6.157(10)
6.0869(5)	6.094(10)

TABLE 3.4: Comparison of experimental data for ^{39}Ca energies (in MeV) to other literature values. Values listed are weighted averages of different angles. Values with asterisk are new states discovered in this work. Values in red are new states discovered in the Gamow window, $E_x \approx 6.0 - 6.5$ MeV

This work MLL data	This work TUNL data	ENSDF (2018)	Setoodehnia et al. [23] (2019)	Hall et al. [22] (2020)	Weighted average
	6.587(3)	6.580(10)	6.579(7)	6.5911(66)	6.586(3)
	6.556(3)*				6.556(3)
	6.507(3)	6.514(10)		6.5092(27)	6.508(2)
6.474(1)	6.483(6)	6.460(10)	6.4722(20)	6.4714(19)	6.4733(10)
6.446(1)*	6.445(3)*	6.451(2)			6.447(1)
				6.4243(18)	6.4243(18)
6.412(6)	6.407(3)	6.405(10)		6.4075(14)	6.408(1)
	6.354(2)*				6.345(2)
6.301(1)	6.298(4)	6.286(10)			6.301(1)
	6.273(3)*			6.2693(22)	6.271(2)
	6.204(3)*				6.204(3)
				6.1741(12)	6.1741(12)
6.1604(6)	6.160(3)	6.157(10)	6.154(5)	6.1567(16)	6.1599(7)
	6.094(2)	6.094(10)	6.083(7)	6.0937(19)	6.093(1)
	6.036(2)*				6.036(2)
	6.020(3)	6.008(10)	6.001(4)		6.013(6)
	5.883(3)*				5.883(3)
	5.844(3)	5.851(10)	5.849(3)	5.8499(19)	5.848(1)
	5.815(3)*				5.815(3)
	5.804(3)	5.786(10)		5.7861(24)	5.793(6)
	5.743(4)		5.738(3)	5.7358(36)	5.739(2)
	5.720(5)	5.720(10)			5.720(5)
	5.682(5)	5.673(10)	5.668(3)	5.6829(18)	5.679(4)
	5.533(2)*				5.533(2)
	5.521(3)*				5.521(3)
	5.490(3)	5.486(10)		5.4834(14)	5.485(2)

TABLE 3.4: Comparison of experimental data for ^{39}Ca energies (in MeV) to other literature values. Values listed are weighted averages of different angles. Values with asterisk are new states discovered in this work. Values in red are new states discovered in the Gamow window, $E_x \approx 6.0 - 6.5$ MeV

This work MLL data	This work TUNL data	ENSDF (2018)	Setoodehnia et al. [23] (2019)	Hall et al. [22] (2020)	Weighted average
	5.452(3)*				5.452(3)
	5.408(3)	5.400(10)	5.405(3)	5.3960(14)	5.399(3)
	5.370(3)	5.364(10)	5.3632(16)		5.365(2)
	5.323(3)*				5.323(3)
	5.233(4)		5.223(4)	5.2260(22)	5.227(2)
	5.161(3)	5.151(2)	5.151(2)	5.1539(24)	5.153(2)
	5.137(3)	5.129(10)		5.1253(24)	5.130(4)
	5.079(3)	5.070(10)	5.076(4)	5.0705(15)	5.073(2)
	4.928(3)	4.929(10)	4.9244(24)		4.926(2)
	4.496(2)	4.488(10)	4.493(2)		4.494(1)
	4.355(3)	4.332(10)	4.339(3)	4.3403(7)	4.341(2)
	4.029(2)	4.0207(17)	4.0207(17)	4.0170(7)	4.019(2)
	3.964(2)	3.9518(8)			
	3.947(3)			3.9499(7)	3.9498(7)
		3.9357(7)	3.9362(22)	3.9375(8)	3.9365(6)
	3.901(2)	3.8911(9)		3.8901(5)	
	3.828(2)	3.8236(15)	3.8217(17)	3.8203(10)	3.822(2)
	3.643(3)	3.6396(8)	3.6396(8)	3.6386(6)	3.6392(4)

The values found in both works in this thesis fall within 2-3 σ of contemporary measurements by Setoodenhia et al. [23] and Hall et al. [22].

Of note is the existence of the 6.446(1) MeV state in the MLL data, corresponding to the 6.445(3) MeV state observed in the TUNL data. This corresponds within 2 σ to the state observed in the DRAGON measurement of $6.450^{+0.002}_{-0.001}$(stat.) $\pm$ 0.001(sys.) MeV, as opposed to the 6.474(1)/6.483(6) MeV state observed in the MLL and TUNL data

respectively. This is further supported by the following observation in the DRAGON experiment: Given a ^{38}K beam energy meant to populate the 6.460(10) MeV state, the reactions had occurred downstream of the center of the gas target, denoting that the resonance strength found must be of a lower energy state than 6.460 MeV. In the analysis of this state, a maximum likelihood method was used to ascertain the energy and resonance strength of $6.450^{+0.002}_{-0.001}$(stat.) $\pm$ 0.001(sys.) MeV. A simulated bismuth germanate detector (BGO) hit pattern using these values is shown in Figure 1.9 as a black solid line. This resonance strength was obtained independently of the the spin and parity.

In the data obtained in Setoodehnia et al. [23], a potentially astrophysically important state with spin parity $5/2^-$ was found at an energy of $E_x = 6.4722(20)$ MeV using the Distorted Wave Born Approximation (DWBA) code FRESCO [55] to determine the spin and parity through the angular distribution of this state. In addition to this, a γ-ray measurement performed by Hall et al. [22] had also found a state of similar energy at $E_x = 6.4714(19)$ MeV. In our work, we have found an excited state that agrees with these contemporary measurements in the MLL data with $E_x = 6.474(1)$ MeV, and in the TUNL data with $E_x = 6.483(6)$ MeV, In the case that the DRAGON measurement did not measure this astrophysically important $5/2^+$ state at approximately 6.4734(20) MeV (weighted average of the measurements by [23], [22], and this work), then there could be a significantly higher proton capture rate than what was concluded in the DRAGON direct measurement. Further, the new states found in Table 3.4 will contribute to the overall proton capture rate, but the extent of this contribution is not known until angular distribution work is done.

Several new states were also found and were observed in multiple angles, many of which fall within the Gamow window. Future work will include determining the spin/parity of the found states, using the code FRESCO. At this time, shell model calculations can be done for low lying states or the ground state, but do not reach the excitation energies of proton unbound states (A. Brown, Priv. Communication). There could be future work in this regard.

Chapter 4

Summary and Conclusions

The properties of ^{39}Ca plays a large role in the ^{38}K(p,γ)^{39}Ca reaction rate; a key reaction that affects the final abundances of endpoint nuclides synthesized during classical novae as identified by the sensitivity study of Ref. [1]. The uncertainty in this reaction rate can alter the final abundances of endpoint nuclides: Ar, Ca, and K by up to two orders of magnitude. In temperature ranges specific to classical novae, the ^{38}K(p,γ)^{39}Ca reaction rate is dominated by $\ell = 0$ transfer reactions within the Gamow window.

Prior to the direct measurement performed with DRAGON, there were three resonances that fit this criteria according to an older ENSDF evaluated dataset of ^{39}Ca excited states at $E_x = 6.160(10), 6.286(10)$, and 6.460(10) MeV, with a spin parity of $J^\pi = 5/2^+$. The direct measurement attempted by the DRAGON collaboration then found the level that was assumed to be $E_x = 6.460(10)$ MeV at $6.450^{+0.002}_{-0.001}$(stat.)0.001(sys.) MeV instead. Meanwhile the states at $E_x = 6.160(10)$ and 6.286(10) remained unobserved in the direct measurement. One possible reason is the large uncertainty associated with each state. Since the hydrogen gas target can only span an energy window of approximately 30 keV, the resonance could be missed if the actual energy of the resonance is much higher or lower than the assumed value. To add to this issue, there is a systematic shift in the energy levels of ^{39}Ca due to newer mass measurements in ^{39}Ca[53] [54]. This further contributes to the possibility that the state was unobserved due to an inaccurate beam energy.

In this work, we performed two transfer reactions to study the states in ^{39}Ca using the ^{40}Ca(d,t)^{39}Ca reaction at the MLL in Garching, Germany and the ^{39}K(^{3}He,t)^{40}Ca reaction at TUNL in North Carolina, USA. The results of these experiments revealed new states in ^{39}Ca as well as reduced the uncertainties of known values by a factor of 3

in most states. These values are corroborated with measurements from Refs. [23] and [22], and agree within 2 σ.

A significant outcome from this work was the discovery of a new state at 6.446(1) MeV and 6.445(3) MeV from the MLL and TUNL experiments respectively. The energy of this new state falls within 2σ of the energy of the state wherein a resonance strength measurement was done by DRAGON. Separate energy levels were found at 6.474(1) MeV and 6.483(6) MeV in the MLL and TUNL experiment which agree within 2 σ of the values observed by Refs. [23] and [22].

Further analysis of the present data set includes angular distribution calculations using the DWBA code FRESCO [55] to find the spins and parities of the new states discovered. This information can be used to calculate theoretical reaction rates in order to estimate the impact of this reaction rate on the overall abundance of endpoint nuclides. Depending on this future work, a remeasurement of the ^{38}K(p,γ)^{39}Ca direct reaction in the Gamow window energy range may be required.

Bibliography

[1] C. Iliadis. *Nuclear Physics of Stars*. Wiley, 2008. ISBN: 978-3-527-61876-7.

[2] C. Iliadis, A. Champagne, J. Jose, S. Starrfield, and P. Tupper. The Effects of Thermonuclear Reaction-Rate Variations on Nova Nucleosynthesis: A Sensitivity Study. *The Astrophysical Journal Supplement Series* 142(1) (Sept. 2002), 105–137. ISSN: 1538-4365.

[3] G. R. Satchler. *Introduction to nuclear reactions*. xii, 316 p. New York: Wiley, 1980. xii, 316 p.

[4] L. Trache. Indirect Methods For Nuclear Astrophysics With Radioactive Nuclear Beams. *AIP Conference Proceedings* 1213 (Mar. 2010).

[5] H. Ritter. Formation and Evolution of Cataclysmic Variables. *arXiv:0809.1800 [astro-ph]* (Sept. 10, 2008).

[6] B. W. Carroll and D. A. Ostlie. *An introduction to modern astrophysics*. 2. ed., Pearson new internat. ed. OCLC: 868368508. Harlow: Pearson, 2014. 1470 pp. ISBN: 978-1-292-02293-2.

[7] S. Chandrasekhar. The Maximum Mass of Ideal White Dwarfs. 74 (July 1931), 81.

[8] J. José and M. Hernanz. Beacons in the sky: Classical novae vs. X-ray bursts. *Eur. Phys. J. A* 27 (S1 Mar. 2006), 107–115. ISSN: 1434-6001, 1434-601X.

[9] I. Iben and M. Y. Fujimoto. The evolution of nova-producing binary stars. In: *Classical Novae*. Ed. by M. F. Bode and A. Evans. 2nd ed. Cambridge Astrophysics. Cambridge University Press, 2008, 34–76.

[10] N. A. Bahcall. Hubble's Law and the expanding universe. *Proceedings of the National Academy of Sciences* 112(11) (2015), 3173–3175. ISSN: 0027-8424.

[11] S. Starrfield, C. Iliadis, and W. R. Hix. Thermonuclear processes. In: *Classical Novae*. Ed. by M. F. Bode and A. Evans. 2nd ed. Cambridge Astrophysics. Cambridge University Press, 2008, 77–101.

[12] J. Casanova, J. José, E. García-Berro, A. Calder, and S.N. Shore. Mixing in classical novae: a 2-D sensitivity study. *A&A* 527 (2011), A5.

[13] P. A. Denissenkov, J. W. Truran, M. Pignatari, R. Trappitsch, C. Ritter, F. Herwig, U. Battino, K. Setoodehnia, and B. Paxton. MESA and NuGrid simulations of classical novae: CO and ONe nova nucleosynthesis. *Monthly Notices of the Royal Astronomical Society* 442(3) (June 2014), 2058–2074. ISSN: 0035-8711.

[14] J. Andrea, H. Drechsel, and S. Starrfield. Element abundances of classical novae. 291 (Nov. 1994), 869–889.

[15] S. Starrfield, C. Iliadis, W. R. Hix, F. X. Timmes, and W. M. Sparks. The effects of the pep nuclear reaction and other improvements in the nuclear reaction rate library on simulations of the classical nova outburst. *ApJ* 692(2) (Feb. 20, 2009), 1532–1542. ISSN: 0004-637X, 1538-4357.

[16] G. Christian et al. Direct measurement of astrophysically important resonances in $^{38}K(p,\gamma\ )\ ^{39}$Ca. *Phys. Rev. C* 97(2) (Feb. 21, 2018), 025802. ISSN: 2469-9985, 2469-9993.

[17] J. Chen. Nuclear Data Sheets for A=39. *Nuclear Data Sheets* 149 (2018), 1–251. ISSN: 0090-3752.

[18] G. Lotay et al. Direct Measurement of the Astrophysical $^{38}\mathrm{K}(p,\gamma)^{39}\mathrm{Ca}$ Reaction and Its Influence on the Production of Nuclides toward the End Point of Nova Nucleosynthesis. *Phys. Rev. Lett.* 116 (13 Apr. 2016), 132701.

[19] R. Laxdal. Acceleration of radioactive ions. *Nuclear Instruments and Methods in Physics Research Section B: Beam Interactions with Materials and Atoms* 204 (2003). 14th International Conference on Electromagnetic Isotope Separators and Techniques Related to their Applications, 400–409. ISSN: 0168-583X.

[20] D. Hutcheon et al. The DRAGON facility for nuclear astrophysics at TRIUMF-ISAC: design, construction and operation. *Nuclear Instruments and Methods in Physics Research Section A: Accelerators, Spectrometers, Detectors and Associated Equipment* 498(1) (2003), 190–210. ISSN: 0168-9002.

[21] J. Tuli. Evaluated nuclear structure data file. *Nuclear Instruments and Methods in Physics Research Section A: Accelerators, Spectrometers, Detectors and Associated Equipment* 369(2) (1996), 506–510. ISSN: 0168-9002.

[22] M. R. Hall et al. γ -ray spectroscopy of astrophysically important states in Ca 39. *Phys. Rev. C* 101(1) (Jan. 29, 2020), 015804. ISSN: 2469-9985, 2469-9993.

[23] K. Setoodehnia, C. Marshall, R. Longland, J. H. Kelley, J. Liang, and F. P. Chaves. Excited states of ^{39}Ca and their significance in nova nucleosynthesis. *Phys. Rev. C* 98(5) (Nov. 26, 2018), 055804. ISSN: 2469-9985, 2469-9993.

[24] P. Doll, G. J. Wagner, K. T. Knöpfle, and G. Mairle. The quasihole aspect of hole strength distributions in odd potassium and calcium isotopes. 263(2) (June 1976), 210–236.

[25] J. Schwartz and B. Watson. Cross-shell transitions in the (3He, t) reaction. *Physics Letters B* 31(4) (1970), 198–200. ISSN: 0370-2693.

[26] R. Hertenberger, K. E. Abiary, P. Schiemenz, and G. Graw. A Stern–Gerlach polarized ion source for the Munich tandem accelerator. *Review of Scientific Instruments* 67(3) (Mar. 1996), 1354–1355. ISSN: 0034-6748, 1089-7623.

[27] R. Hertenberger, A. Metz, Y. Eisermann, K. El Abiary, A. Ludewig, C. Pertl, S. Trieb, H.-F. Wirth, P. Schiemenz, and G. Graw. The Stern–Gerlach polarized ion source for the Munich MP-tandem laboratory, a bright source for unpolarized hydrogen and helium ion beams as well. *Nuclear Instruments and Methods in Physics Research Section A: Accelerators, Spectrometers, Detectors and Associated Equipment* 536(3) (Jan. 2005), 266–272. ISSN: 01689002.

[28] R. Middleton. A survey of negative ion sources for tandem accelerators. *Nuclear Instruments and Methods* 122 (Nov. 1974), 35–43. ISSN: 0029554X.

[29] W. Assmann et al. The Munich MP tandem. *Nuclear Instruments and Methods* 122 (Nov. 1974), 191–203. ISSN: 0029554X.

[30] D. T. Irvine. A Study of the Astrophysically Important States of 31S via the 32S(d,t)31S Reaction (Feb. 2012), 105.

[31] J. F. Ziegler, M. D. Ziegler, and J. P. Biersack. SRIM - The stopping and range of ions in matter (2010). *Nuclear Instruments and Methods in Physics Research B* 268(11-12) (June 2010), 1818–1823.

[32] C. Wiedner, M. Goldschmidt, D. Rieck, H. Enge, and S. Kowalski. Performance of a QDDD spectrograph. *Nuclear Instruments and Methods* 105(2) (Dec. 1972), 205–210. ISSN: 0029554X.

[33] H. A. Enge. Magnetic spectrographs for nuclear reaction studies. *Nuclear Instruments and Methods* 162(1) (June 1979), 161–180. ISSN: 0029554X.

[34] H.-F. Wirth, J. Ott, H. Angerer, T. von Egidy, Y.Eisermann, G.Graw, and R.Hertenberger. New Q3D Focal Plane Detector with Cathode-strip Readout Became Operational. *Maier-Leibnitz-Laboratorium Annual Report* (2000), 71.

[35] G. Knoll. *Radiation Detection and Measurement*. Wiley, 2010. ISBN: 978-0-470-13148-0.

[36] W. R. Leo. *Techniques for Nuclear and Particle Physics Experiments*. Berlin, Heidelberg: Springer Berlin Heidelberg, 1994. ISBN: 978-3-540-57280-0 978-3-642-57920-2.

[37] J. Ott, H. Angerer, T. von Egidy, R. Georgii, and W. Schauer. A position sensitive cathode strip detector with single strip readout. *Nuclear Instruments and Methods in Physics Research Section A: Accelerators, Spectrometers, Detectors and Associated Equipment* 367(1) (1995). Proceedings of the 7th International Wire Chamber Conference, 280–284. ISSN: 0168-9002.

[38] R. Lutter, O. Schaile, K. Schoffel, K. Steinberger, P. Thirolf, and C. Broude. MARaBOU - A MBS and ROOT Based Online/Offline Utility (), 4.

[39] B. Wolf. *Handbook of Ion Sources*. Taylor & Francis, 1995. ISBN: 978-0-8493-2502-1.

[40] D. Combs. *Beta Decay as a Test of the StandardModel*. North Carolina State University, 2018.

[41] H. R. Hiddleston, R. E. Chrien, J. A. Fasolo, J. A. Frederick, and D. C. Minette. Sodium Vapor Charge Exchange Cell (1976), 6.

[42] J. Spencer and H. Enge. Split-pole magnetic spectrograph for precision nuclear spectroscopy. 49(2) (1967), 181–193.

[43] C. Marshall, K. Setoodehnia, K. Kowal, F. Portillo, A. E. Champagne, S. Hale, A. Dummer, and R. Longland. The Focal plane Detector Package on the TUNL Split-pole Spectrograph. *arXiv:1806.02401 [nucl-ex, physics:physics]* (June 6, 2018).

[44] M. Ohring. Chapter 3 - Thin-Film Evaporation Processes. In: *Materials Science of Thin Films (Second Edition)*. Ed. by M. Ohring. Second Edition. San Diego: Academic Press, 2002, 95–144. ISBN: 978-0-12-524975-1.

[45] C. Morris, L. Atencio, W. Sondheim, S. Seestrom, M. Rawool-Sullivan, P. McGaughey, D. Lee, W. Kinnison, M. Brooks, and V. Armijo. Electric discharge etching of thin metalized plastic films. *Nuclear Instruments and Methods in Physics Research Section A: Accelerators, Spectrometers, Detectors and Associated Equipment* 379(2) (Sept. 1996), 243–246. ISSN: 01689002.

[46] G. Smith, J. Fischer, and V. Radeka. Capacitive charge division in centroid finding cathode readouts in MWPCs. *IEEE Trans. Nucl. Sci.* 35(1) (Feb. 1988), 409–413. ISSN: 0018-9499, 1558-1578.

[47] S. Agostinelli et al. Geant4—a simulation toolkit. *Nuclear Instruments and Methods in Physics Research Section A: Accelerators, Spectrometers, Detectors and Associated Equipment* 506(3) (2003), 250–303. ISSN: 0168-9002.

[48] E.Segre, H. Staube, H.A.Bethe, and J.Ashkin. *Experimental nuclear physics*. Vol. 1. 1. New York, Wiley and sons, 1953, 253.

[49] R. Brun and F. Rademakers. ROOT An object oriented data analysis framework. *Nuclear Instruments and Methods in Physics Research Section A: Accelerators, Spectrometers, Detectors and Associated Equipment* 389(1) (1997). New Computing Techniques in Physics Research V, 81–86. ISSN: 0168-9002.

[50] C. Marshall, P. Morfouace, N. De Séréville, and R. Longland. Bayesian Analysis of the ^{70}Zn(d,^{3}He)^{69}Cu Transfer Reaction (June 2020).

[51] *Front Matter*. Elsevier, 2015, i–ii. ISBN: 978-0-12-405888-0.

[52] C. Fry et al. Discovery of ^{34g,m}Cl$(p,\gamma)^{35}$Ar resonances activated at classical nova temperatures. *Phys. Rev. C* 91 (1 Jan. 2015), 015803.

[53] W. Huang, G. Audi, M. Wang, F. Kondev, S. Naimi, and X. Xu. The AME2016 atomic mass evaluation (I). Evaluation of input data; And adjustment procedures. *Chinese Physics C* 41 (Mar. 2017), 030002.

[54] A. Wapstra, G. Audi, and C. Thibault. The Ame2003 atomic mass evaluation: (I). Evaluation of input data, adjustment procedures. *Nuclear Physics A* 729(1) (2003). The 2003 NUBASE and Atomic Mass Evaluations, 129–336. ISSN: 0375-9474.

[55] I. J. Thompson and F. M. Nunes. *Nuclear Reactions for Astrophysics: Principles, Calculation and Applications of Low-Energy Reactions*. Cambridge University Press, 2009.